A Thin-Film Model to Characterize a Luminescent Solar Concentrator for Higher Efficiency Electricity Generation

by

Don Jehan Savio Reshon Jayamaha

A thesis submitted in partial fulfillment of the requirements for the degree of

Master of Science

Department of Mechanical Engineering
University of Alberta

Abstract

A Luminescent Solar Concentrator (LSC) is a device that consists of a transparent plate with photovoltaic (PV) cells connected to one or more sides. The transparent plate functions as a waveguide and contains luminescent particles, such as organic dyes or quantum dots. The luminescent particles absorb sunlight and part of the re-emitted rays is guided towards the edges of the LSC by total internal reflection, where light is converted to electrical energy from the PV cells. The efficiency of the received sunlight directed to the edges of the LSC is determined by the size of the waveguide and the luminescent particles. This thesis outlined the important characteristics of the LSC, such that we can optimize its optical efficiency for best performance. Here, red-dye (Lumogen F 305) and silicon quantum dots (Si-QDs) were studied, and their application to the LSC was simulated by modifying the physics of the photon interaction.

Initially, a red-dye-based LSC model was simulated in ray-tracing software. The LSC simulation results are compared to existing experimental measurements. After the validation of results, the ray-tracing method was extended to the silicon quantum dot-based thin-film LSC model. Quantum dots were found to be a good luminescent particles for LSCs since they have a large Stokes shift, which reduces the re-absorption loss. Later, a silicon quantum dot thin-film LSC model was simulated, in which, a ray-tracing simulation model is developed to study the optical efficiency of a given LSC structure. The model consists of a low-iron glass with a copolymer film known as Poly (butyl methacrylate-co-methyl methacrylate) and silicon quantum dots embedded in it. The quantum dot characteristics were changed in this model, and the optical efficiencies were recorded. The models were used to present different parameter studies of the LSC to optimize performance.

Acknowledgement

This thesis work has been challenging, but having academic supervisors and family support makes everything easier. I would like to thank a few unique people while completing my graduate studies.

Firstly, I would like to offer special thanks to Dr. Walid Moussa, who, although no longer with us, accepted me to be one of his students, which inspired me by his example and his dedicated support to his students he served throughout his career. He is an excellent supervisor, and I express my utmost gratitude for all the support he provided me.

I am also grateful to my current supervisors, Dr. Tim Weis and Dr. Arman Hemmati, for their invaluable patience and feedback on completing my master's program. They have given various inputs and guided me in improving my technical writing to complete this thesis.

I would also like to thank Dr. David Antoniuk and his team in Applied Quantum Materials for providing data on quantum dots for my thesis project to use in the simulation software.

I would like to thank my parents for their support in the difficult times they faced during the time I was completing my program. I am sincerely grateful for the love and care they provided me to the best of their ability.

Finally, I would also like to thank the University of Alberta for being a supportive multicultural university for graduate students.

I would like to apologize if I have left anyone out of this list and I would like to express my sincere thanks for your help.

Don Jehan Jayamaha

November 2022

Table of Contents

List of Tables

List of Figures

List of Abbreviations

AM 1.5	Air mass coefficient of 1.5 atmosphere thickness, corresponding to a solar zenith angle of z = 48.2°
AQM	Applied Quantum Material Inc.
BAPV	Building applied photovoltaics devices
BiPV	Building integrated photovoltaic devices
LSC	Luminescent solar concentrator
MFP	Mean free path [mm]
PLQY	Photoluminescent quantum yield
PMMA	Poly-methyl methacrylate. Used as waveguide for luminescent solar concentrators
PV	Photovoltaic device
QD	Quantum dots
Si	Silicon
TIR	Total internal reflection

List of Symbols

A	Surface area [cm^2] or [m^2]
d	Waveguide glass thickness [mm]
G	Geometric gain, the incident light area (A_{top}) to the total area of the edges (A_{edge})
H	Waveguide height [mm]
L	Waveguide length [mm]
N	Density of luminescent particles in the waveguide [mm^3]
R	Reflection (%)
T	Transmission (%)
W	Waveguide thickness [mm] where luminescent materials are doped in it
$\boldsymbol{\alpha}$	Absorption coefficient [mm^{-1}]
$\boldsymbol{\lambda}$	Light wavelength [nm]
$\boldsymbol{\sigma}$	Optical cross-section of the particle [mm^2]
$\boldsymbol{\kappa}$	Extinction coefficient
$\boldsymbol{\eta_{opt}}$	Optical efficiency, defined as the ratio between output (P_{out}) and the input power (P_{in})
$\boldsymbol{\eta_{QY}}$	Quantum yield
$\boldsymbol{\theta_c}$	Critical angle
$\boldsymbol{\mathcal{R}}$	MFP ratio, ratio between MFP length before and after emission by a luminescent particle

Chapter 1

Introduction

In environmentally sustainable and renewable energy sources, use of solar power presents a solution to the increasing energy demand and reducing the environmental impacts from fossil-fuels [1]. Electricity generated from solar energy offers significant advantages compared with conventional resources, including its nonpolluting, renewable, and widely distributed characteristics. For a long time, development of photovoltaic (PV) systems have been lowering their costs while improving their efficiency. However, the silicon solar cell itself still remains a key cost to electricity generation from solar energy. Luminescent Solar Concentrators (LSCs) were developed to lower the cost of PV solar cells and to introduce new applications, such as transparent windows. Light concentration, light trapping, and luminescence are three principal process, which are combined in an LSC. Historically, the solar cells themselves were the most expensive component of the system, and it was advantageous to concentrate the light prior to illuminating it on a reduced cell area. As the cost of solar PV cells have declined, today the biggest opportunity for LSC is to take advantage of buildings with large areas covered with windows. This includes power generation for

skyscrapers, apartments, and single-family houses. LSC technology offers advantages in architectural integration, i.e., light weight, tunability of color, ability to work under diffuse light. These advantages allow LSC to overcome some of the intrinsic limitation of conventional PV systems [2], [3]. Compared to bulk-plate LSC configuration, where a polymer slab acts as a waveguide that is lightly doped with luminescent particles, the thin-film LSC configuration presents advantages of depositing heavily doped thin luminescent film on any transparent material. These broaden the applicability of this technology [4], [5].

This thesis discusses how quantum dots can be modelled in new LSC windows. This study first provides a foundation for the theory, while establishing the background knowledge on the subject matter. In this work a thin-film quantum dot LSC system is investigated based on different parameters, such as luminescent concentration, LSC film and glass thickness, and LSC size. This chapter describes the background knowledge of the LSC.

1.1. Motivation

The dependence of our society on energy resources dominates our economy and industries, such that energy is the lifeblood of technological and economic development [6]. Even with more efficient new technologies, energy demand is expected to increase due to population and economic growth. To this end, primary energy including coal, oil, natural gas, solar, and wind, increased by 28% from 2005 to 2019. During the same period, Canada produced 33% more primary energy [7].

The Energy Information Administration (EIA) predicts that the world primary energy consumption will increase by around 50% between 2018 and 2050 [8]. Currently, global energy consumption increases by 2% per year, which indicates that demand for energy will continue to grow. On average around 80% of the primary energy comes from fossil fuels, which have major environmental impacts including air pollution and increasing greenhouse gas (GHG) emissions [9].

As shown in Figure 1.1, EIA's International Energy Outlook 2019 identifies that the global energy related GHG emissions will continue to grow in the near future. GHG emissions have started to plateau and even decline in some countries (Organization for Economic Cooperation and

Development, OECD), although the growth of GHG emissions will be dominated by non-OECD countries, i.e., China and India, in the coming years. The EIA business as usual forecast suggests member countries' GHG emissions collectively will decline at a rate of 0.2% per year from 2018 to 2050. Since non-OECD countries have growing populations and economies, in the absence of major changes related to GHG emissions in energy production, emissions are expected to increase at a rate of 1% per year from 2018 to 2050 [10]. Increase use of renewable energy, such as solar, will be important in curbing this growth.

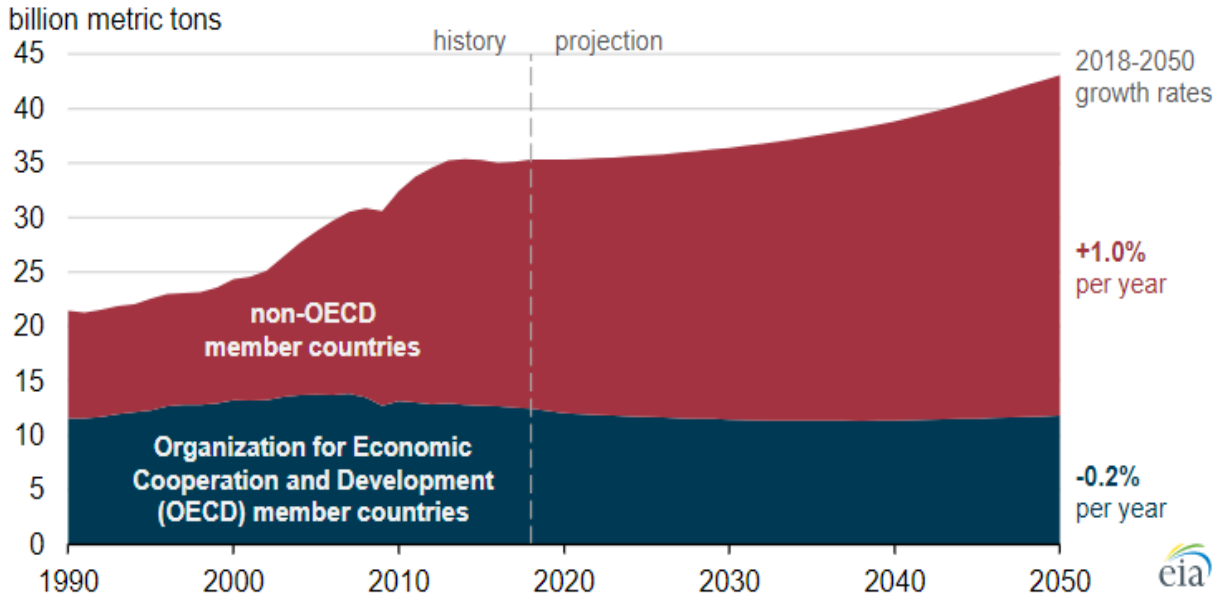

Figure 1.1: Global energy-related carbon dioxide emission from 1990 to 2018 and projected to 2050. (Reprinted with permission from U.S. EIA [10].)

Solar power is a clean energy source with near-zero GHG emissions for producing electricity. Material systems, such as copper indium gallium selenide (CIGS) and cadmium telluride (CdTe), have been used to reduce the production cost of PV cells for the solar energy industry [11]. Photovoltaic technologies recently have shown remarkable progress, such that now PV accounts for one of the lowest cost electricity generations globally [12]. Solar cells have a wide range of applications, from calculators to rooftop solar panels and even utility-scale power plants. Improving the design and using advanced materials to build solar cells, have led to a higher efficiency for

these systems. Research and development will continue to reduce the cost of solar cells and increase their efficiency [13].

PV systems have been growing rapidly in recent years. Figure 1.2 shows the evolution of the annual PV installation from 2000 to 2021. At the end of 2021, a cumulative capacity of ~175 GW is installed in the world. China has led PV annual installation in recent years compared to other countries [14]. Today, most PV is built in large utility-scale configurations. However, solar as part of buildings offer the benefit of local energy supply and reduced distribution losses. Houses and office buildings account for 40% of overall energy use in the United States [15]. There are two different concepts in distributed PV systems: Building applied photovoltaics (BAPV) and building integrated photovoltaics (BIPV). PV systems installed on existing buildings are called BAPV, while BIPV refers to PV systems that replace conventional building materials such as PV tiles, PV shingles, and PV glass [14].

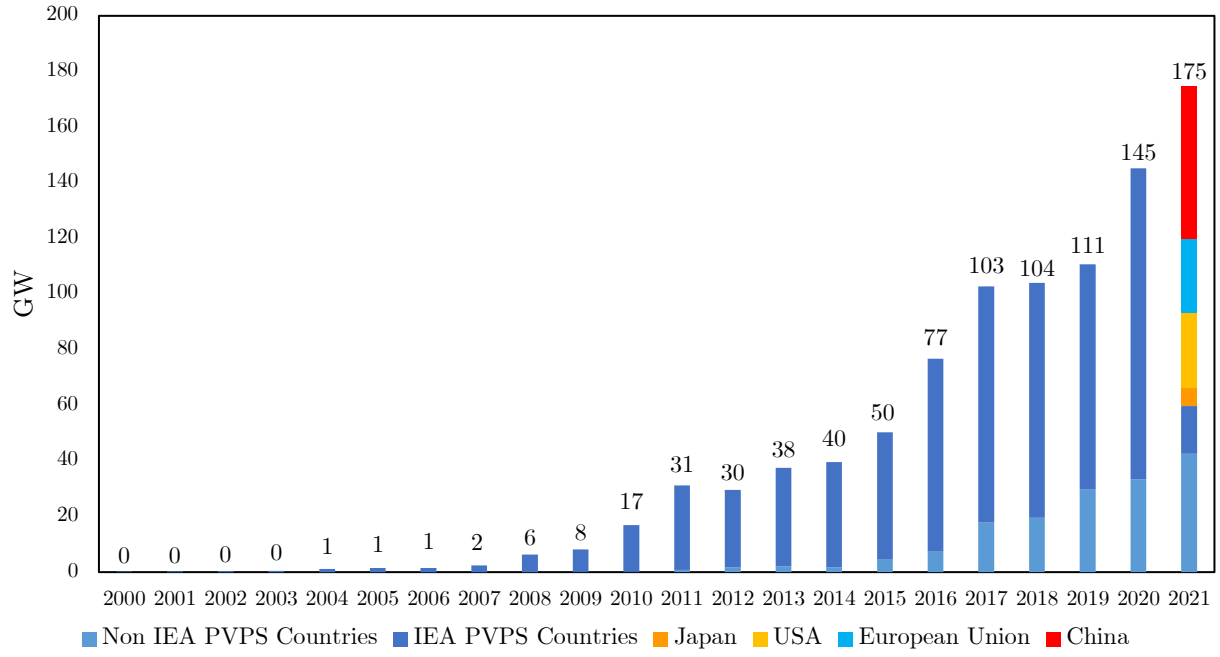

Figure 1.2: Annual PV installations. (Reprinted with permission from IEA PVPS Task 1 [14].)

A photovoltaic cell requires a large surface area to collect sunlight and convert solar energy into electrical energy. Unfortunately, tall buildings have small rooftop spaces relative to their overall

size, which are not sufficient for rooftop PV to supply their electrical requirements. As a result, new innovative technologies are needed for solar energy-harvesting devices in the form of PV windows [16]. Material scientists in the past have tried to embed light-absorbing films into glass windows, where the architects find it unappealing due to their reddish or brown tint. The latest solar power window technologies absorb ultraviolet (UV) or infrared light. This blocks the UV and infrared radiations, which normally pass through the glass, and sometimes delivers unwanted heat. By generating power from the solar window and reducing the heat gain, windows have an immense potential for energy harvesting with sufficient capacity to power up a large office building in the future [15].

1.2. Background

Solar energy was first discovered in 1839 when Edmond Becquerel discovered the photovoltaic effect. They explained how electric current can be generated from sunlight. Even after extensive research and development on the introduced theory, the efficiency of photovoltaic power was low, but their work set the stage for solar cells [17]. American inventor Charles Fritts created the first solar cell in 1883 using selenium. The efficiency obtained was less than one percent at converting sunlight to electricity. This motivated many researchers to continue researching photovoltaics in the following decades. The first silicon solar cell, which was created in Bell Labs, was about 6% efficient at converting solar energy into electricity [13]. In 1956, the first commercialized solar panel cost was around $300 per watt [18]. As the price per watt was expensive to mass produce, the efforts to commercialize did not succeed in the United States. During the energy crisis in the 1970s, the federal government focused more on making solar energy viable for the market. The Solar Energy Research, Development and Demonstration Act of 1974 was passed to utilize solar energy as a major source for energy needs [19].

The demand for electricity will be increasing in the future and many efforts have been placed on BIPV technologies, where the PV element becomes part of the building. Various techniques have been proposed for concentrating solar light into a smaller area, where energy can be collected efficiently. There are two types of solar concentration: Solar thermal power concentrators and

concentrators that use PV cells. Solar thermal concentrators use mirrors to concentrate sunlight into a smaller area to generate heat, where the heat is delivered to a steam engine to produce electricity [20]. PV concentrators focus solar light into smaller PV cells for electricity generation. Thus, solar energy efficiency can increase by concentrating solar radiation, cost effectively [21]. This concept of concentrating solar energy has been extensively researched, which has led to the idea of Luminescent Solar Concentrators (LSCs) [22]. LSCs were initially proposed in 1976 to reduce the cost of silicon solar cells, and as an alternative for traditional solar panels [16].

As solar cells were costly, the luminescent solar concentrator concept was developed to reduce the number of solar cells required per unit area. The most common configuration of LSC is attaching PV cells to the edge of the luminescent waveguide that is coated or doped with highly fluorescent materials. This concept was to focus the light from a large area into a smaller area of solar cells to generate electricity. The Luminescent particle is one of the key components that directly determines the LSC performance. Different types of luminescent materials, such as dyes or quantum dots, can be used in LSCs. By design, direct or diffuse sunlight can penetrate the waveguide and be absorbed by the luminescent materials and re-emitted to the edges of the LSC. Thus, sunlight tracking option is not necessary and can be integrated into the built environment (Figure 1.3) [16] [23].

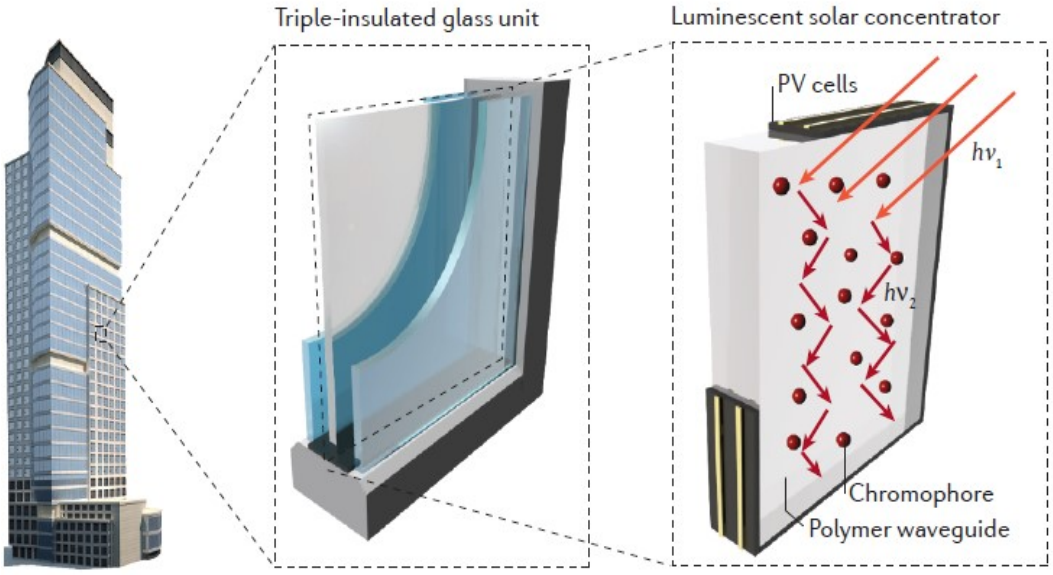

Figure 1.3: Schematic representation of a PV window. (Reprinted with permission from Nature Review Materials [16].)

The major advantage over silicon-based PV panels is that LSC can adapt in the built-in environment. As the weight in plastic or glass waveguide is less compared to the silicon PV panels, the LSC are viable for mounting on sides of the building [24]. To increase optical efficiency in LSCs, different luminescent particles (dyes, quantum dots) and waveguide materials are used in configuring the LSC. Quantum dots (QDs) have shown a number of promising properties in LSCs [25]. QD particles present no self-absorption as their absorption and emission spectrum is substantially shifted. Among various types of QDs, silicon quantum dots (Si-QD) are one of the highly efficient luminescent solar concentrators, while Si-QD is one of the most abundant elements on the Earth's crust [26]. This abundance of silicon is beneficial, since it is a non-toxic material that is readily available. Furthermore, due to the non-toxic behavior of Si-QD, studies have been conducted to use silicon nanomaterials for biological applications [27].

The non-toxic nature of Si and its availability can be important for the future of LSC industry in BIPV applications. Furthermore, these silicon semiconductor nanoparticles hold great potential in the fast-growing world of nanotechnology. Only silicon QD doped bulk LSCs configuration have been studies and other configurations are not documented. This thesis has worked on a thin-film based LSC configuration setup where silicon QDs are used as luminescent materials.

1.3. Novelty and Objectives

This thesis is motivated by solar energy harvesting technology and it focuses on the luminescent solar concentrator concept. Particularly, it assists in developing a product using a small area of PV cells and high-efficiency concentrators for electricity generation. This thesis utilizes several design parameters to study the optical performance of LSC. Understanding the interaction between light and quantum dots is crucial in optimizing the performance of LSC. The main question is proposed in this thesis: which explore the main parameters affecting the performance of LSC and how they can be optimized.

To answer the proposed question, the ray-tracing simulation software will be used to achieve the following objectives:

1. Develop an accurate LSC ray-tracing model for interactions between light and luminescent particles.
2. Validate an existing LSC model and create a Si-QD LSC prototype in a ray tracing software.
3. Quantify power losses in the LSC and the amount of light reaching the PV edge.
4. Optimize power output using different parameters of the LSC.

1.4. Thesis Outline

This thesis focuses on understanding luminescent dyes and quantum dots in LSC. To achieve the proposed objectives, first an understanding of the operating principles of an LSC is needed. The theoretical background related to an LSC are discussed in Chapter 2, which explains the information necessary to understand the concepts and theories for constructing a ray-tracing simulation of an LSC model. This chapter discusses the main physical phenomena by first explaining the main optic concepts that relate to the operating principle inside an LSC. Luminescent process is discussed to understand the properties of luminescent particles, such as organic dyes and quantum dots. Finally, the equations necessary to obtain the overall optical efficiency of an LSC is shown.

Chapter 3 describes the methodology. This chapter is broken down to two models. The first LSC model has red-dye luminescent particles, which are embedded in a waveguide. The second LSC model consists of two layers. The first layer is a glass component, and the second layer is a thin copolymer film coating on top of the glass, which has QD luminescent particles embedded in it. The simulation of red-dye based LSC model in Chapter 4 discusses whether ANSYS can be used as a tool to simulate a LSC device, and how accurate are the simulation results. A red-dye based LSC is modeled in a ray-tracing software, and the estimated optical efficiency and losses obtained by the simulation is compared to the experimental data from the thesis of Lisset Manzano Chávez [28].

The simulation of quantum-dot-based LSC model in Chapter 5 characterizes the Si-QD based LSC model with the data provided by Applied Quantum Materials (AQM). In this chapter, the Si-QD

LSC model is simulated using ray-tracing software to find the optimum parameters of the LSC model with different photoluminescence, quantum yield, polymer thickness, and LSC lengths.

Finally, conclusions on the LSC model are discussed in Chapter 6 along with recommendations to improve the LSC model.

Chapter 2

Theoretical Background

This chapter focuses on explaining the main theories associated with a Luminescent Solar Concentrator. The aim is to establish a background knowledge to analyze and compare different models in simulating ray-tracing. In section 2.1, the concepts on optics are described. Then the luminescent particles are described in section 2.2. Finally in section 2.3, the operating principle of an LSC is described.

2.1. Concepts of optics

Light has dual behavior, such that it acts as a wave and as a particle (photon). Considering this behavior, properties of light can be further explained. When light interacts with a matter, it ejects electrons, which produces electricity. This is called the photoelectric effect. Albert Einstein explained that light particle energies are related to their frequencies according to Planck's formula [29]. The energy of a photon can be given as,

$$E_{ph} = hv \tag{2.1}$$

Here, h is Planck's constant and v is the frequency of light. This equation can be further derived as [29]:

$$E_{ph} = \frac{hc}{\lambda}, \tag{2.2}$$

where c is the speed of light, and λ is the wavelength of light [nm]. This equation demonstrates the photon energy at different wavelengths. Different frequencies of light can carry photons with different energies.

2.1.1. Reflection and Refraction

The refractive index is closely related to the velocity of light. The velocity of light in vacuum is the largest when compared to other mediums, i.e., Water or glass. Refractive index (n) of a matter is defined by the ratio between the two velocities of light, the velocity of light in vacuum (c) [m/s] to that in the given medium (v) [m/s] [29]:

$$n = \frac{c}{v} \tag{2.3}$$

When light passes through a material, the propagation of light will decrease. This is described in the form of a complex refractive index, defined as: $\tilde{n} = n + ik$. Here, the real part (n) is called the usual refractive index, and the extinction coefficient (k) is the imaginary part of the refractive index that represents the absorption of light in the material.

The extinction coefficient (k) is related to the absorption coefficient (α), and by using equation (2.4), it can convert the extinction coefficient to the absorption coefficient [1/mm] [30], such that,

$$\alpha = \frac{4\pi k}{\lambda}. \tag{2.4}$$

Here, λ is the wavelength of light [nm].

As shown in Figure 2.1, light hitting the surface between two mediums with different refractive indices of n_1 and n_2 at an angle of θ_1 breaks to two parts. Part of the light will be reflected with an angle of θ_1', and another part will refract with an angle of θ_2. This characteristic defines a Fresnel loss, where part of the light will reflect, and another part is refracted from the surface. The angles are measured relatively perpendicular to the surface from where the light interacts with the surface.

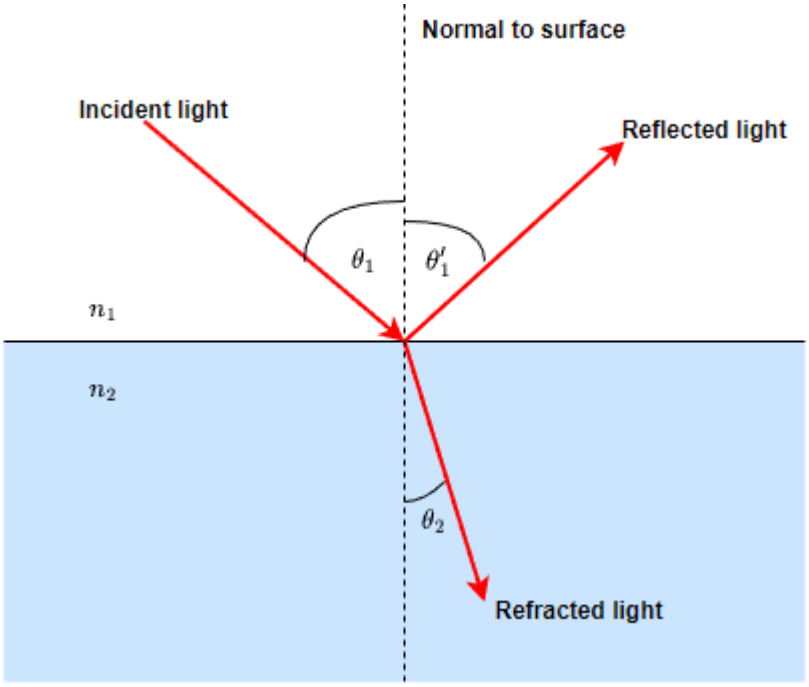

Figure 2.1: Reflection and refraction of light between two medias.

For unpolarized light with normal incidence angles ($\theta_1 = \theta_2 = 0^o$), the reflectance (R) is calculated according to:

$$R = \left|\frac{n_1 - n_2}{n_1 + n_2}\right|^2 \tag{2.5}$$

If the media is non-absorbing, the transmittance (T) and reflectance (R) add up as T + R = 1. Figure 2.1 shows how light changes its direction when traveling through a change in refractive index. Direction of the light changes depending on the incident angle and the refractive index of

both mediums. The law of refraction, or Snell's Law, represents the mathematical relationship that relates the refractive index of both materials, angle of incident (θ_1), and angle of refraction (θ_2) [29]:

$$n_1 \sin(\theta_1) = n_2 \sin(\theta_2) \tag{2.6}$$

When light travels from a low refractive index to a higher refractive index ($n_1 < n_2$), it can be trapped in a waveguide if the incident angle is above a critical angle. Equation (2.7) presents the critical angle, at which the total internal reflection occurs.

$$\theta_c = \sin^{-1}\left(\frac{n_2}{n_1}\right) \tag{2.7}$$

Total internal reflection (TIR) will occur when the incidence angle is higher than the critical angle, where the light will reflect multiple times inside the waveguide.

2.1.2. Absorption

When light passes through a material, part of its energy will transfer to the medium in the absorption process. Transmittance (T) is the ratio of the amount of light transmitted (ϕ') to the amount of incident light (ϕ_0) through a material measured at the same wavelength. This relation shows the exponential law of absorption or Lambert-Beer Law [29].

$$\mathrm{T} = \frac{\phi'}{\phi_0} = e^{-\alpha d} \tag{2.8}$$

Here, α is the absorption coefficient [1/mm] and d [mm] is the thickness of the material.

2.2. Luminescence

Luminescence is the emission of light from an excited state of a molecule (luminophore) that does not arise from heating. Various types of luminescence exists based on the energy source that

initiates the luminescent process, such as thermoluminescence, radioluminescence, mechanoluminescence, chemiluminescence, electroluminescence, cathodoluminescence, and photoluminescence [31]. In LSC principle photoluminescence process is the emision of light, where absorption of photons takes placed.

In Figure 2.2, the luminophore excitation process is shown. When an luminophore absorbs light, it excites from the ground state (S_0) to a maximum energy level (singlet state S_2), identified as state 1 in Figure 2.2. The ground state describes all electrons in the lowest possible energy level. The excited state depends on the luminophore and typically lasts 1-10 nanoseconds. Excited electrons fall to the lowest energy excited state, which is semi-stable (singlet state S_1) by releasing some of the absorbed energy as heat, (phase 2 in Figure 2.2). The electron will then fall back to its ground state (S_0) by releasing the remaining energy as fluorescence (state 3 in Figure 2.2). This released energy has a longer wavelength (low energy). In molecular systems, fluorescence is commonly referred to as photoluminescence [32].

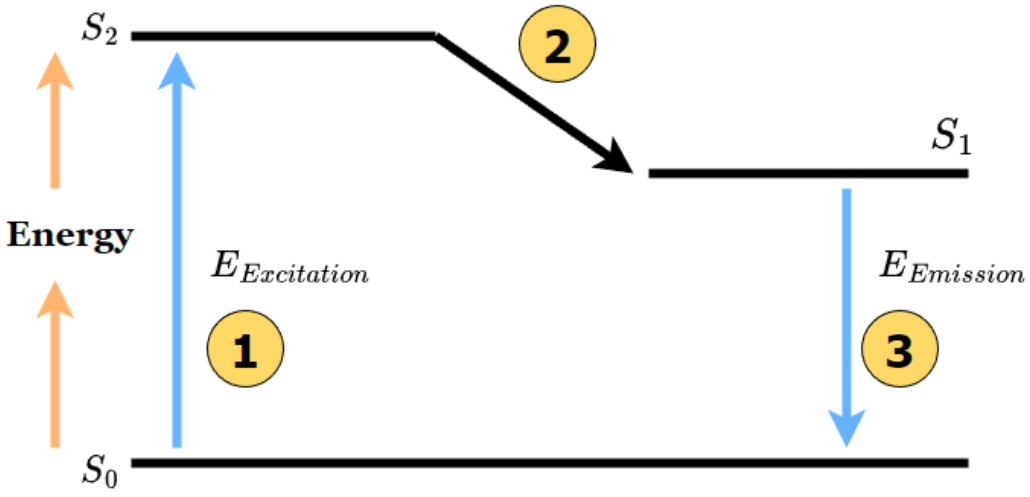

Figure 2.2: Excited electron movement of a luminescent particle. (Figure adapted from bio-rad [32].)

Absorption and emission spectra shown in Figure 2.3 are the characteristic property of luminophores in the luminescent particle. The Strokes' shift is the difference between the wavelengths of maximum absorption (A in Figure 2.3) and maximum emission (C in Figure 2.3)

in a luminophore [32] [33]. Suppose a large Stoke shift (B in Figure 2.3) is present in a luminophore. In that case, this shows that there will be less overlap between the absorption and emission spectra, resulting in a low probability of re-absorption by other luminophores. So, small Stoke shift luminophores have re-absorption losses [32] [33].

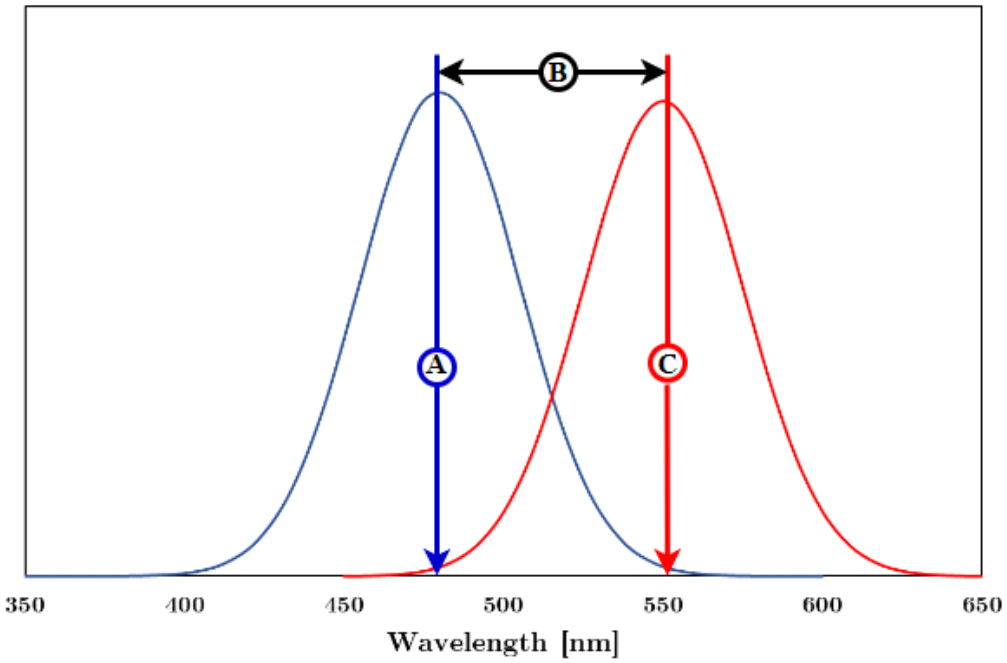

Figure 2.3: Schematic drawing of an absorption and emission spectrum. (Figure adapted from bio-rad [32].)

Another parameter to evaluate the photoluminescence efficiency is the photoluminescent quantum yield (PLQY), also known as quantum yield (η_{QY}). The light emitted within the waveguide is determined by η_{QY} of the luminescent particle. Quantum yield is the ratio between the number of photons emitted to the number of photons absorbed [34].

$$\eta_{QY} = \frac{Number\ of\ photons\ emitted}{Number\ of\ photons\ absorbed} \tag{2.9}$$

2.2.1. Luminescent Material

Luminescent materials are one of the important components of the LSC design. Luminescent material properties must be considered to minimize losses for LSC development. A list of these properties for an ideal luminescent material are [35]:

- Wide spectral absorption: A broader absorption spectrum is ideal for absorbing a wider range of incident solar energy.
- A higher Stokes' shift: The overlap of absorption and emission spectra of a luminescent material needs to be minimized to obtain higher optical efficiency.
- A higher photoluminescent quantum yield: The efficiency of a luminescent material should be higher to ensure a high emission probability.
- The lifetime of the luminescent material: For commercial use, the luminescent material needs to perform at a certain level over many years.
- Solubility in a waveguide: The luminescent material needs to be soluble in the waveguide material with the required optical properties.

The property of luminescent particles doped in the polymer or glass waveguide is an essential factor in defining the efficiency of an LSC. Therefore, identifying the optimal luminescent particle for the LSC system is essential for improving LSC performance. To date, various types of luminescent particles, such as organic dyes and quantum dots, have been utilized as light converters for LSC purposes. These are summarized in Table 2.1, in which it is shown that organic dyes with a smaller absorption range have a higher PLQY. Also, organic dye-based LSCs have higher re-absorption losses due to the Stokes' shifts for Lumogen Red 305 and Rhodamine (Rh B), which are ~140 and ~65 meV, respectively [36].

Table 2.1: Optical properties of luminescent particles.

Luminescent particles		**Absorption range (nm)**	**Emission range (nm)**	**Stokes shift (meV)**	η_{QY} (%)	**Ref**
Organic dyes	Perylene dye 4	400-580	500-650	-	96	[37]
	Coumarin-540	420-555	450-620	~264	78	[38]
	Lumogen Red 305	400-620	580-740	~140	~100	[39]
	Rh B	450-620	520-650	~65	~70-97	[40]
Quantum dots	CdSe/ CdS	400-650	590-700	~400	45	[41]
	PbS/CdS	300-800	800-1100	~250	~40-50	[42]
	Si	300-660	640-1000	~400	50	[26]

2.2.1.1. Organic Dyes

Organic dyes were mainly investigated as luminescent particles for the LSC application in the early stages of LSC research. Most organic dyes are categorized as perylene, coumarin, and rhodamine. As seen in Table 2.1, most dyes overlap between absorption and emission spectra, where photons will be self-absorbed, resulting in self-absorption losses. Even though organic dyes are cheap to produce, having a self-absorption loss, leads to a non-efficient dye-based LSCs. Among all dyes, Lumogen Red 305 organic dye is often used for comparison in LSCs, and it is used for the dye-based simulation. The small Stokes' shift of organic dyes causes self-absorption losses, which limits their performance in large-area LSCs. Moreover, the narrow absorption band limits the solar energy harvested in LSCs.

One of the main disadvantages of organic dyes is their limited lifetime compared to the lifetime of solar PV cells (≈ 20 years) under illumination [35]. Stark *et al.* [43] have shown that absorption intensity has decreased in Red305 organic dyes when exposed to light for a significant amount of time (see Figure 2.4). The authors have conducted an experiment where an LSC doped with Lumogen Red 305 was attached to a solar cell and the short circuit current was measured at various intervals during illuminations. The LSC is illuminated under a sulfur lamp and outdoors. As shown in Figure 2.4, the sample was illuminated using a sulfur lamp, and the sample kept

outdoors showed a 20% decrease in the short circuit current. The reference sample, which is stored in a dark environment, shows a minor difference.

Organic dyes are advantageous compared to QDs due to their high PLQY, low cost, and availability. However, they are disadvantageous due to their photo-stability, narrow absorption spectrum, broad emission spectrum, and overlap between absorption and emission spectra. This drawback has prevented commercialization of dye-based LSCs. Compared to traditional organic dyes, quantum dots are excellent emitters for LSCs. They can be engineered to suppress re-absorption energy losses by providing a large Stokes' shift in the absorption and emission spectra, which increases the efficiency of LSC devices [36].

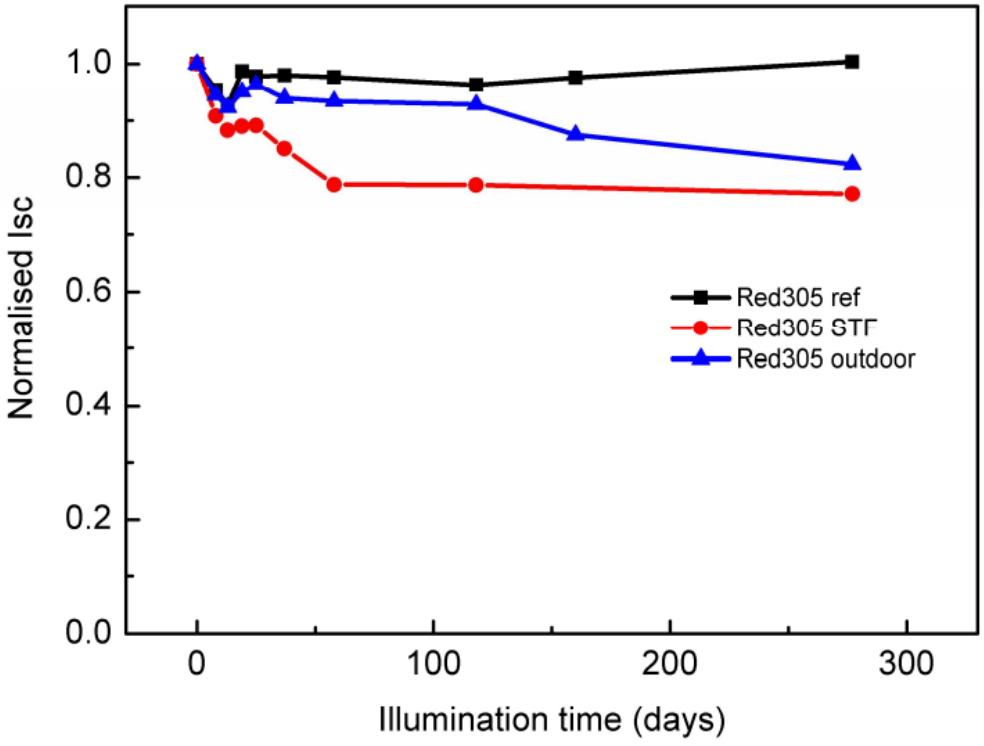

Figure 2.4: LSC degradation under illumination in a duration of 300 days. (Reprinted with permission from The Optical Society [43].)

2.2.1.2. Quantum Dots

Quantum dots are inorganic semiconductor nanocrystals (spherical materials) with a diameter of 2-8 nm [44]. When the size of a bulk semiconducting crystal is reduced to the nanoscale, it gains different properties that differ from its bulk property. Quantum dots have unique properties depending on their size and also high photostability under illumination [45]. An excited electron in a quantum dot can release higher energy than a bulk crystal when moving to a lower energy level. This released energy might be able to excite another electron in the valence band. The band gap of a QD can be engineered by altering its size, which changes the absorption emission peak. Combining different band gap materials, the core-shell structure shown in Figure 2.5 can obtain a larger stokes shift than organic dyes [46]. In addition, the low quantum yield in QD-based LSC results in the possibility that no photons will re-emit from the QD when a QD absorbs an emitted photon. There also has been concern regarding the toxicity of some QDs.

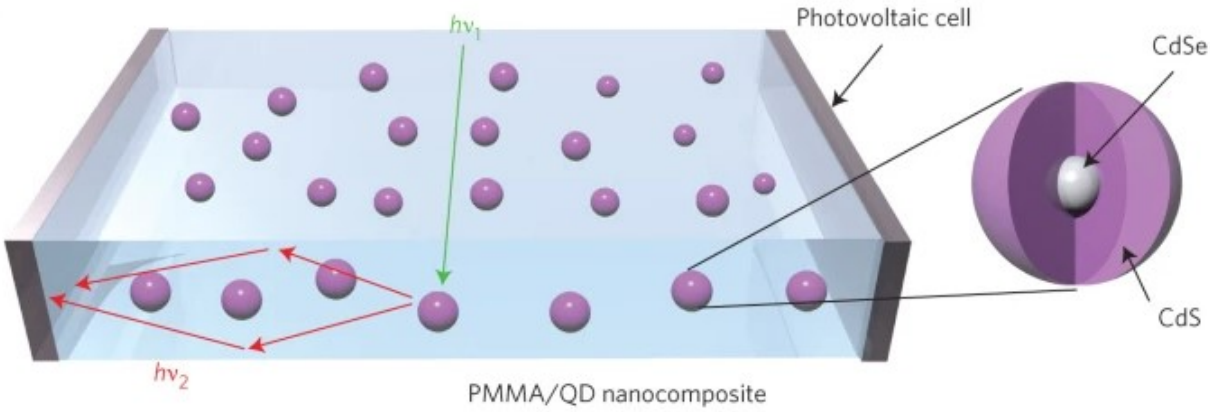

Figure 2.5: Schematic representation of LSC with QDs. (Reprinted with permission from Nature Photonics [41].)

Silicon nanocrystals are classified as QDs when the crystallite size is reduced below Si's Bohr exciton diameter of ~10 nm [47]. Si is an indirect band gap semiconductor, where the maximum energy of the valence band occurs in a different value of momentum in the minimum energy of the conduction band. Figure 2.6 (b) shows that an electron in an indirect bandgap semiconductor requires additional energy for the momentum change that is included in the energy gap (E_g) to

transition electrons from the maximum point in the valence band to the minimum point in the conduction band. Compared to direct bandgap semiconductors, indirect bandgap semiconductors are inefficient emitters where the optical transitions are allowed only if phonons are absorbed or emitted to conserve the momentum of the bulk Si. However, when quantum confinement occurs, the uncertainty of the crystal momentum increases allowing optical transitions without involving phonons [48] [49]. The quantum confinement effect has shown the importance of Si QDs which results in the photoluminescence improvement of the Si QDs compared to bulk Si, where photoluminescence is the important property in the LSC application [48].

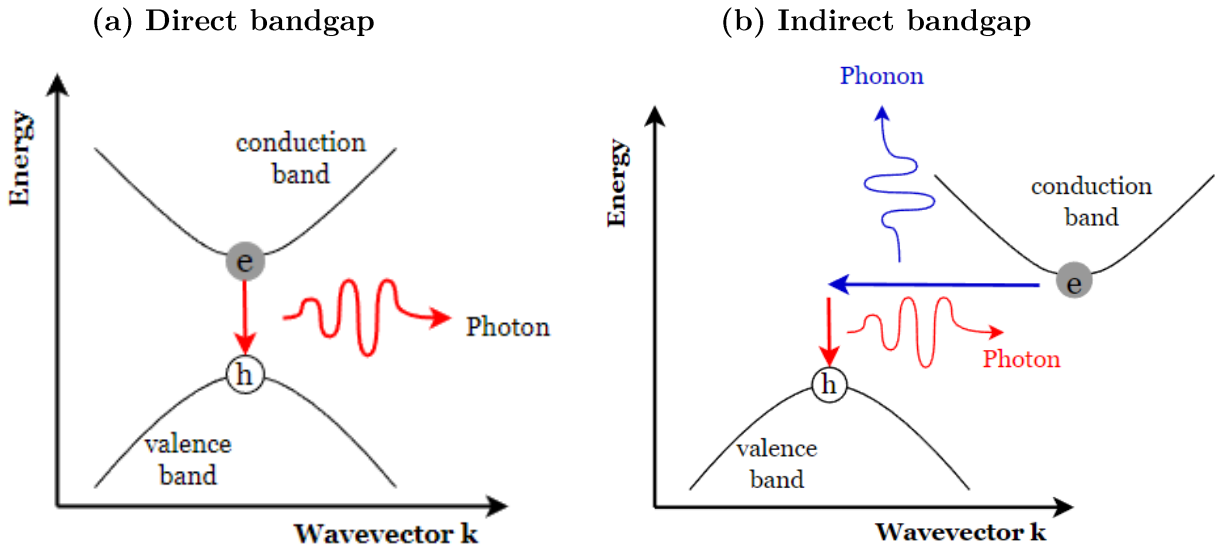

Figure 2.6: Schematic representation in (a) direct bandgap semiconductor and (b) indirect bandgap semiconductor. (Figure adapted from Samantha [48].)

2.3. Literature review of bulk and thin-film LSCs

Coropceanu & Bawendi [50] have used CdSe/CdS QDs embedded in LSC (2 cm x 2 cm x 0.2 cm) with 0.5% w/w concentration. The QD PLQY is 86%. All four surface areas of the edges are used in the LSC for optical efficiency measurements. The optical efficiency of 48% was obtained at a fixed wavelength of 400 nm. Meinardi *et al.* [41] have considered a PMMA slab (21.5 cm x 1.3 cm x 0.5 cm) embedding CdSe/CdS QDs of a concentration of 0.05% w/w with a PLQY of 45%. One of the smaller edges was used to collect the light of the LSC. Reflectors are placed in the long surfaces to reflect the escaped light into the waveguide (no reflectors are at the base of the PMMA slab and opposite face of the detector). From this LSC setup, the optical efficiency of 10.2% is measured. Meinardi *et al.* [51] have used CISe coated with ZnS with a concentration of 0.5% w/w doped in an LSC (12 cm x 12 cm x 0.3 cm) with a PLQY of 40%. No reflectors are placed on the bottom of the slab, and all four edges are used to measure the optical efficiency of 3.27%. Zhou *et al.* [52] have fabricated a QD-based LSC (5 cm x 1.5 cm x 0.3 cm) by embedding PbS/CdS QDs of a concentration of 0.5% w/w. The geometric factor (G) is the ratio of the area of the top surface and the edge surface (other three edges are being covered by the mirrors to limit photon losses) is 16. The PLQY is 40-50%, and the QD-based LSC reaches an optical efficiency of up to 6.1%. Meinardi *et al.* [26] have shown indirect bandgap silicon quantum dots as promising materials for LSCs. Silicon is a promising material for commercialized use for LSC applications due to its non-toxicity, low cost, and ultra-earth abundance. A Si QD size of 4.6 nm is embedded in an LSC waveguide (12 cm x 12 cm x 0.26 cm) with a PLQY of 46%. All four side of the LSC is used to measure the power conversion efficiency of 2.85%, where the power is collected by solar cells from the LSC edges.

Two different methods are considered to construct an LSC. One method is to embed luminescent particles directly into the waveguide, which is called a bulk LSC. The other method is to deposit a luminescent film on top of a transparent waveguide, where the film is much thinner than the waveguide. This device is called a thin-film luminescent solar concentrator. The thin-film LSC represents a convenient technology in the PV systems. The main reason for this method is to reduce cost and practicality. Thin-film LSCs are necessary because they enable to deposit into any

transparent waveguide, i.e., glass windows. In this situation, the thin doped layer is responsible for the absorption of sunlight. It is then emitted to the glass waveguide, where the majority of the light propagates within the glass waveguide resulting in lower re-absorption losses. The thin-film LSC structure containing luminescent material coated on a transparent plate was suggested to reduce re-absorption losses in the LSC. The thin-film reduces the re-absorption loss by confining the absorption and emission to the thin film, so the emitted light is primary trapped in the transparent waveguide.

de Boer *et al.* [53] found that Sm^{2+}-based phosphor has a relatively broad absorption spectrum, and a peak emission around 700 nm fulfills most of the luminescent material requirements. The problem with this inorganic phosphor is that it has a particle size in the micrometer range, which scatter the emitted light. A plate (100 mm x 100 mm x 2.5 mm) with a refractive index of 1.5 with negligible absorption is used as a light guide to perform a ray-tracing simulation. A luminophore coating is applied in the bottom of the light guide with a coating thickness of 100 µm (0.1 mm). The bottom surface of the coating is a perfect mirror. The top surface of the light guide is covered with a wave-length selective filter, which reflects emitted light but not incident light which the luminescent material will absorb. The author shows that this LSC setup can reduce the re-absorption and cone losses in the LSC.

Ying *et al.* [54] proposed inorganic phosphors for thin-film LSCs. The phosphor concentration and the suitable position of the thin phosphor layer in the LSC were investigated using different commercial phosphors. Several thin-film LSC with different inorganic phosphors material, phosphor concentrations, and the thin-film phosphor layer position in the LSC were investigated for the effective LSC. A glass plate (50 mm x 50 mm x 5 mm) is used as the light guide in the LSC. The phosphor layer thickness of 0.65 mm was used in the LSC device. Four phosphors, such as EG2762, NYAG4EL, R630, and R670, were used in the LSC with phosphor concentrations of 10%, 20%, 30%, 40%, and 50%. When the phosphor layer is placed on the top surface of the LSC, the optical efficiency decreases as the phosphor concentration increases from 10% to 50%. At higher concentrations in the phosphor layer, incident light is absorbed by more phosphors and reduces the optical efficiency. With the increase of phosphor concentration, the thin-film re-absorption increases, reducing the emitted light that travels to the PV cell. For all the phosphor

concentrations, the order of the highest optical efficiency for different phosphors was NYAG4EL > EG2762 > R630 > R670. The trend resembled the phosphors' QYs of EG2762, NYAG4EL, R630, and R670 were 0.93, 0.95, 0.84, and 0.80, respectively. When the phosphor layer is on the glass plate's top surface, incident light must first enter the phosphor layer, and more emitted light is directed to the PV cell on the glass edge. With high phosphor concentrations, re-absorption loss dominates in the phosphor layer, which reduces the emission light to the PV cell. The phosphor QY dominated the optical efficiency when the phosphor layer was on top of the glass surface. The author then investigated when the phosphor layer was on the bottom of the glass surface. In this setup, the optical efficiency increased when the phosphor concentration increased from 10% to 50%. The emitted light from the phosphor layer increased the light trapping with higher phosphor concentration. The high concentration in the phosphor layer scatters the incident light and emits the light to the glass plate. Thus, high concentration in the phosphor layer contributes to the optical efficiency when the film is on the bottom surface of the glass. For all the phosphor concentrations, the optical efficiency for different phosphors was R670 > R630 > EG2762 > NYAG4EL in the following order. The R670 phosphor has a broader absorption spectrum that overlaps a larger solar spectrum and delivers high optical efficiency. As seen above, the order of the phosphor layers is different when film placement is changed from the top to the bottom surface of the LSC. Therefore, the types of phosphors, phosphor concentration, and the thin phosphor layer position affect the LSC.

Zhang *et al.* [55] investigate the performance in a large-area LSC with two different waveguide materials. A LSCs (20 cm x 20 cm x 0.1 cm) with glass-based and PMMA-based with a G factor of 50 is used as the light guides in this LSC performance analysis. A uniform fluorophore layer thickness of ~3 µm was deposited on both glass and PMMA-based light guides. In this literature, the optical flux gain, which refers to the density of the incident and output photons of the LSC, has a higher optical flux gain in the PMMA-based LSC compared to glass-based LSC for all increased G values. When the G value was increased from 37.5 to 50, the optical flux gain from the glass-based LSC did not change. This indicates that more emitted light never reached the waveguide edges at higher G. However, the optical flux gain increased three times higher in the PMMA-based device than in glass-based LSC at G = 50. The ray simulation indicated that the absorbance of the waveguide significantly impacted the performance of large-area LSCs. The

optical flux gain from glass-based LSC stopped increasing when G is larger than 50, which shows similar results compared to experimental data. In a PMMA-based waveguide, the increase in optical flux gain above G = 50 is greater than in the glass-based waveguide. This demonstrates that for large-area LSC sizes, the main loss is due to the absorbance of the waveguide. This highlights the importance of the waveguide material used in the large area LSC.

Chávez [28] proposed two thulium models in her thesis report. The 1st model contains thulium particles (Tm^{2+}) doped in a glass. The 2nd model has two layers: glass and a thin film coating with Tm^{2+} particles on one side of the glass surface. The materials were assumed to have no impurities or absorption characteristics in the waveguide. Different LSC parameters are studied in the simulation tests. Mean Free Path (MFP) length, quantum yield, glass thickness, and LSC size have been studied to find optimum efficiency (MFP is discussed in section 3.2.1). In these tests, a light beam of 550 nm hits the center of the plate. One LSC edge was used to obtain the optical efficiency in the ray simulation software. The front and back surfaces were Fresnel type, and the other three edges were mirrors. The 1st model, which has a uniform concentration of thulium particles, is doped in a glass waveguide (50 mm x 50 mm x 5 mm). When the MFP length is increased, the optical efficiency increases until the MFP length is 5 mm. The thermalization losses decreased, and transmission losses increased at longer MFP. This is because larger MFP means lower phosphor concentration, where light can easily pass through the model. The next simulation was done with different quantum yield values of 1.0, 0.9, 0.8, and 0.6. As expected, the unity quantum yield, where one photon emitted per photon absorbed, receives the highest optical efficiency. The optical efficiency of 13% is obtained at an MFP length of 5 mm. In lower quantum yield with the same MFP length, the optical efficiency was lower as there were less photons emitted per photons absorbed. With a QY of 0.9 the maximum optical efficiency is about 12%, with a QY of 0.8 the maximum optical efficiency is 10.5%, and finally for the lower QY of 0.6 the maximum optical efficiency of 8% is obtained. The glass thicknesses 3, 4, 5, and 6 mm were tested in the first LSC model to see the optical efficiency change from thinner to the thicker waveguide, where the standard model thickness is 5 mm. The optical efficiency of thinner glass thickness (3 and 4 mm) is lower than the standard thickness of 5 mm in the same thulium concentration. With a glass thickness of 6 mm, the optical efficiency increased by ~1% from the standard glass thickness. In the next simulation, the surface area of model 1 was changed by 4 cm^2, 25 cm^2, 100 cm^2, and 400

cm^2, and the light beam was hitting the center of the glass. As expected, the highest optical efficiency was received in a smaller area (4 cm^2) LSC, and the lowest optical efficiency was received in a larger area (400 cm^2) LSC. In the same thulium particle concentration, photons travel a shorter distance in the smaller area LSC, while in larger area LSCs, photons have to travel longer distances which will likely be scattered outside of the plate and lost, which reduces the optical efficiency. In a 100 cm^2 size area LSC, the maximum optical efficiency was ~9% and in a 400 cm^2 size area LSC, the maximum optical efficiency was 5.6%. The 2nd model has a layer of pure silicon glass with a thickness of 5 mm and a Tm^{2+} doped coating film with a fixed thickness of 5 µm at the bottom of the glass. A light beam hits the front glass surface where the thulium coating is on the bottom surface. The simulation results are tested with different parameter results of MFP length, phosphor quantum yield, glass thickness, and LSC area. The MFP range tested is from 0.1 µm to 100 µm. In this simulation test, the thermalization losses due to down-conversion decreases with longer MFP (low concentration). However, the transmission losses increase as thulium film has a lower concentration. The optical efficiency is lower in MFP length below 1.5 µm. Then the optical efficiency increases up to 11%, and it keeps above 10% till 7 µm of MFP. The next simulations were tested by changing the quantum yield values of 1.0, 0.9, 0.8, and 0.6. The same trend of optical efficiency was obtained as in model 1. The maximum optical efficiency in the unity quantum yield was close to 11% in 4 and 5 µm of MFP length. In other quantum yields, the maximum optical efficiency was in this MFP length. With a QY of 0.9 the maximum efficiency was ~9.8%, QY of 0.8 the maximum efficiency was 8.7%, and finally with a lower QY of 0.6 the maximum optical efficiency was 6.5%. In the next simulation test, the film thickness was fixed and only the glass thickness was changed and simulated. The glass thicknesses of 4, 5, and 6 mm were modeled to obtain optical efficiency results with different glass widths while changing the concentration from 0.1 to 100 µm. In smaller MFP lengths, the optical efficiency is higher in the thicker glass. When the MFP length was 100 µm, the optical efficiency was similar in all glass thicknesses. Therefore, the glass thickness does not affect the optical efficiency at lower concentrations. In the final simulations, the LSC areas of 4, 25, 100, and 400 cm^2 were used to analyze the optical efficiency. In a small area (4 cm^2) LSC, the maximum optical efficiency was ~16%, the standard size (25 cm^2) LSC was ~11%, 100 cm^2 size LSC was 6.4%, and finally the

largest area (400 cm^2) LSC obtained a maximum efficiency of 3.6%. As expected, this shows that maximum optical efficiency decreases with large-area LSCs.

Griffini *et.al* [56] have examined the impact on the thin-film LSC, where the luminescent dye concentration and luminescent film thickness were varied. The concentration of the luminescent particles (Lumogen F Red 305) was varied in the thin-film LSC from 0.01% w/w to 10 % w/w. The power conversion efficiency obtained was 4.8% in a 5% w/w concentration. By increasing the dye concentration, the efficiency was reduced obtaining 4% in a 10% w/w dye concentration. In addition to varying the dye concentration, the effect of film thickness was investigated. By increasing the thickness of the LSC film in the range of 2 µm to 13 µm, the power conversion efficiency increased to 5.2% for a thickness of 8 µm and then it remained unchanged. This thesis is mainly focused on the thin-film LSC, where silicon quantum dots are used as luminescent particles.

Film-based LSCs have been reported in previous literatures, where different luminescent particles have been used in the luminescent film. Meinardi *et al.* [26] first time have used indirect bandgap QDs and is considered as a luminescent material choice for the LSC application. Indirect band gap Si-QDs have a low overlap between absorption and emission spectra, which results in low re-absorption losses in large-area LSCs. The author has doped Si-QDs in a PMMA to analyze optical efficiency in the bulk LSC and proven that indirect bandgap Si-QDs are useful for LSCs. Furthermore, thin films on glass reduce the effective path length through the polymer, suppressing the waveguide's absorption for optimizing Si-QD LSCs. In this thesis, we have used indirect band gap Si-QDs in a thin copolymer film and a low-iron glass where low absorption takes place in the waveguide. This LSC configuration was used in ray-tracing software to find the optical efficiency with different LSC parameter.

2.4. Operating principle of LSCs

The standard design of a conventional LSC allows the sunlight to enter through the top surface of a transparent material doped with luminescent material. The material should have a higher index of refraction as the photons will be reflected internally in the waveguide. The main component of the LSC is the doped luminescent particles, which absorb most of the incident light and re-emit it with a longer wavelength. The longer wavelength photons will travel to the edge of the waveguide, where a PV cell will collect the light and convert it to electrical energy (see Figure 2.7).

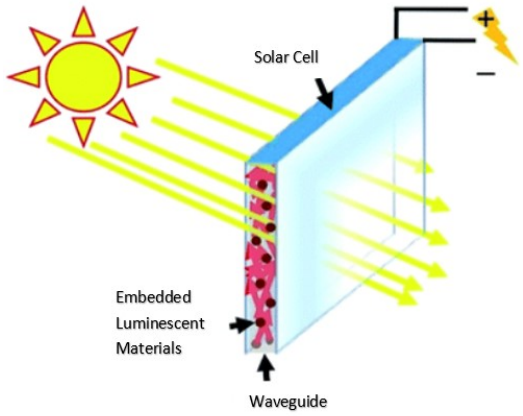

Figure 2.7: Schematic representation of fluorescence material based LSC. (Reprinted with permission from RSC Advances [22].)

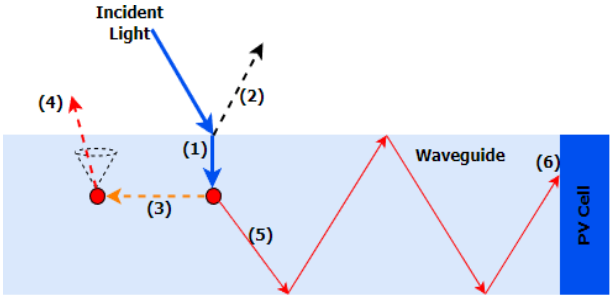

Figure 2.8: Schematic representation of light transport inside an LSC. (Figure adapted from Assadi *et al.* [57].)

Figure 2.8 shows the light propagation process through an LSC in 6 stages: (1) Incident light enters from the top surface and is transmitted to the waveguide; (2) Part of the light reflects, and the luminescent particle absorbs another part; (3) Luminescent particles re-emit the light, whereas another luminescent particle absorbs it; (4) Re-emitted light inside the escape cone is lost to the outside of the waveguide; (5) Re-emitted light by the luminescent particle can be trapped in the waveguide; (6) Trapped light will be absorbed by the photovoltaic cell, which is attached to the LSC [28].

Using inexpensive materials, e.g., glass or plastic, the cost of solar energy can be lowered via LSCs. A large concentrator factor can be obtained by placing a small area of PV cells on the edge of the waveguide. Concentration ratio (CR) is the ratio between the energy per unit area of incident light

to energy per unit area of concentrated light. When CR increases, the generated electricity price reduces since the concentrated light provides more power per unit area. Geometric gain (G) is a key factor related to the CR. Geometric gain is the incident light area (A_{top}) to the total area of the edges (A_{edge}) of the concentrator:

$$\mathrm{G} = \frac{A_{top}}{A_{edge}} \tag{2.10}$$

With larger values of geometric gain, LSCs can generate larger CRs.

2.4.1. Mean Free Path

The characteristics of the luminescent particles and their concentration in the waveguide determine the light interaction with a medium. The interaction between photon and luminophore is related to the number of particles and the mean free path. Mean Free Path (MFP) is the average distance a photon can travel without being absorbed or scattered by another luminophore particle [28]. This photon-luminophore interaction is translated into equation (2.11), where the MFP is inversely proportional to the multiplication of particle concentration and its optical cross-section [58].

$$MFP = \frac{1}{N \cdot \sigma} \tag{2.11}$$

Here, N is the density of particle in the waveguide, and σ is the optical cross-section of the particle. Light is easily absorbed by the luminescent particle for larger cross-sections, whereas photons are not absorbed in smaller cross-sections.

2.4.2. LSC performance

The overall efficiency of an LSC device is set by the light reaching the photovoltaic cell located at the edges of the waveguide. This efficiency is called optical efficiency (n_{opt}).

$$n_{LSC} = n_{opt} * n_{PV} \tag{2.12}$$

Here, n_{PV} is the light conversion efficiency. This efficiency is dependent on the material technology used in the PV cells. Optical efficiency (n_{opt}) is the ratio of output power (P_{out}) from the edges of the LSCs and input power (P_{in}) entering the top surface of the LSC:

$$n_{opt} = \frac{P_{out}}{P_{in}} \tag{2.13}$$

Incident light inside an LSC has various possible loss factors. Figure 2.9 shows a detailed schematic representation of losses in a waveguide. These losses include no photon absorption, no emission, self-absorption, scattering, escape cone losses, and surface impurity losses [59].

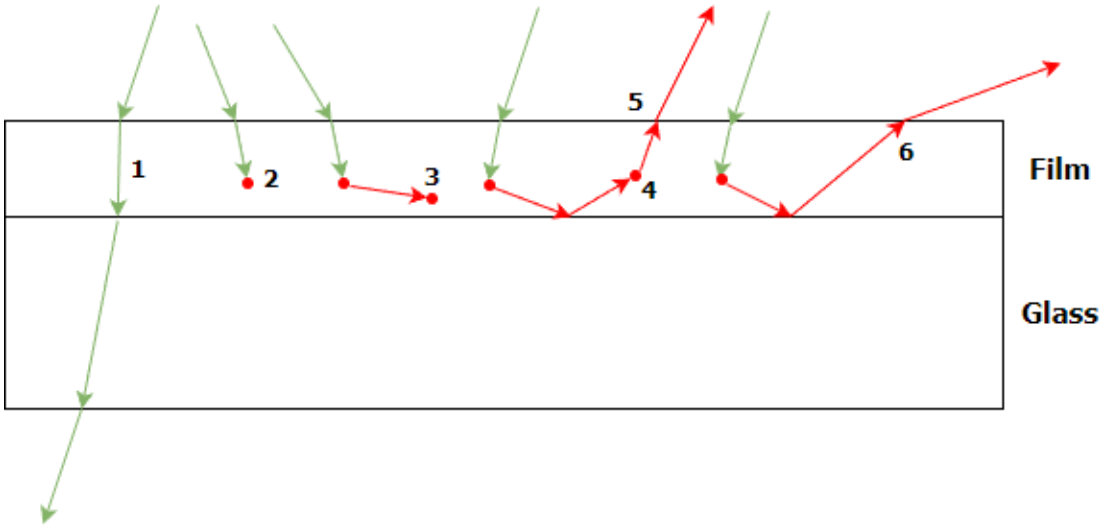

Figure 2.9: Incident light losses in a waveguide. (Figure adapted from Wiegman [59].)

Reisfeld *et al.* [60] presented equation (2.14) to describe the overall efficiency with different loss mechanisms.

$$n_{opt} = (1 - R) * n_{LHE} * n_{QY} * n_{self} * n_{St} * n_{trap} * n_{WG} \tag{2.14}$$

Here, $(1 - R)$ is the light portion transmitted into the LSC, where R is the Fresnel reflection coefficient of the LSC surface. Value of R for standard glass is around 4% [60].

Light harvesting efficiency (n_{LHE}) is the efficiency of absorption of incoming photons. For example in Figure 2.9, ray 1 is not absorbed. Light harvesting efficiency depends on the source emission

spectrum (S_{SO}) and the absorption spectrum of the LSC. Equation (2.15) describes n_{LHE} as the ratio of absorbed photons to the available photon flux [61]:

$$n_{LHE} = \frac{\int_0^\infty S_{SO}(\lambda)[1 - 10^{-A(\lambda)}]d\lambda}{\int_0^\infty S_{SO}(\lambda)d\lambda} \tag{2.15}$$

The term $[1 - 10^{-A(\lambda)}]$ describes the absorbed photons by the luminescent particle, where A is the absorbance as a function of wavelength (λ).

Photoluminescence quantum yield (n_{QY}) is the ratio between the number of photons emitted to the number of photons absorbed (In Figure 2.9, ray 2 is absorbed and not re-emitted.). The self-absorption efficiency (n_{self}) is the overlap between absorption and emission spectrum (Ray 3 in Figure 2.9.).

Stokes efficiency (n_{St}) is the ratio between the average energy of the emitted photons (v_{em}) to the average energy of the absorbed photons (v_{abs}), which is equivalent to:

$$n_{St} = \frac{v_{em}}{v_{abs}} \tag{2.16}$$

Trapping efficiency (n_{trap}) indicates the photons not lost by the emitted photons inside the escape cone (Ray 5 in Figure 2.9). Therefore, it is calculated from the refractive index (n) of the waveguide by using the following equation [60]:

$$n_{trap} = \sqrt{1 - \frac{1}{n^2}} \tag{2.17}$$

The waveguide efficiency (n_{WG}), also known as transport efficiency, accounts for the photon transport losses due to waveguide imperfections, e.g., absorption and scattering in the waveguide [28] [59] [60]. (See rays 4 and 6 in Figure 2.9)

Different losses in an LSC can be broken down into properties of the waveguide and luminescent materials, as mentioned in Table 2.2. A related property of the waveguide to reduce the LSC losses

is to increase the refractive index of the waveguide while maintaining transparency. Increasing the refractive index of the waveguide will also slightly increase Fresnel reflection losses [35].

Table 2.2: LSC losses as properties of the waveguide and luminescence material.

Property of Waveguide	**Property of Luminescent Material**
A good quality waveguide, i.e., a waveguide with no air bubbles and impurities, can be chosen to reduce the losses by absorption and scattering.	Increasing the absorbed spectrum of the luminescent material to absorb a broader range of the solar spectrum.
A higher refractive index of the waveguide can be used to trap the light by TIR inside the waveguide.	Using a high photoluminescent quantum yield luminescent material. PLQY≈ 100%
Minimize surface roughness to reduce loss of TIR photons.	Increase the Stokes shift to reduce the re-absorption losses by the luminescent materials.
Host material should also be inexpensive, lightweight, and non-toxic.	Photostable for multiple years is necessary to have a long lifetime of the LSC.

2.4.3. Intensity profile

The angle of light changes when traveling through the waveguide. This results in the change of path length and interactions at interfaces. When light interacts with the LSC, part of the light is reflected, absorbed, emitted, and guided in the LSC. An expression can be derived for the intensity profile in the LSC edge by using ray optics discussed previously. Ray optics is applied to the LSC's thin film and glass waveguide.

The relevant angles are represented in Figure 2.10 for the directional intensity profile calculations. The objective is to derive an expression for the intensity radiating from the LSC's PV surface (interface 1). This function is derived from the viewing angles θ and ϕ from the PV surface. The angles' capital characters are inside the waveguide, and the lower characters demonstrate incident

emitting and observation angles. For example in interface 2, angles α and A are related to Snell's law (equation (2.6)), and angles θ and Θ are at interface 1 [59].

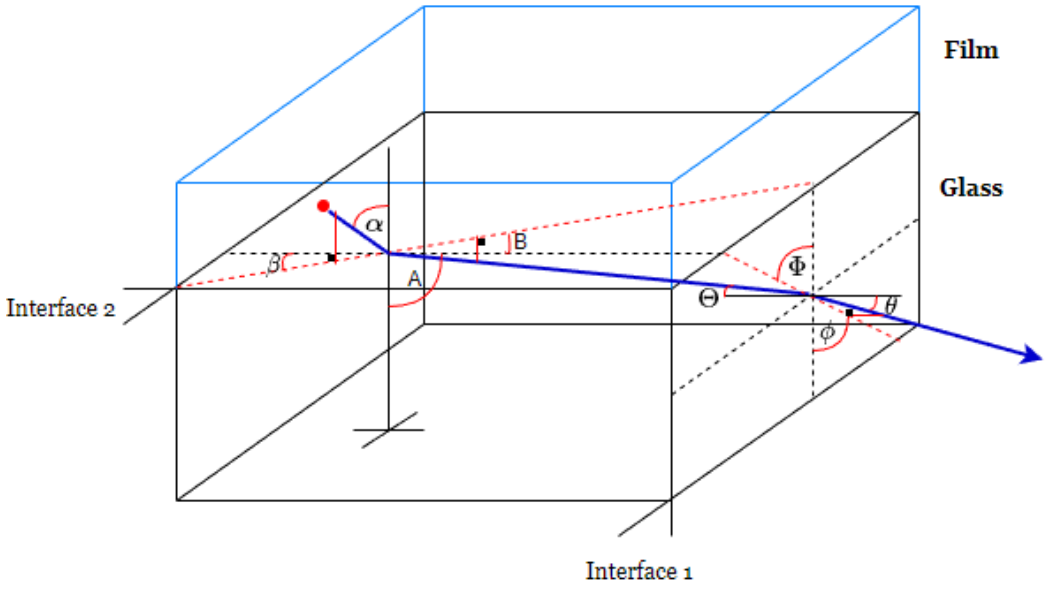

Figure 2.10: Schematic representation of the directional intensity profile calculations of a thin film LSC. (Figure adapted from Wiegman [59].)

Wiegman [59] describes that the power radiated from the luminescent particle is defined by the following expression with small angles $d\alpha$ and $d\beta$:

$$dP = \frac{P_0}{4\pi} \sin\alpha \, d\alpha \, d\beta \tag{2.18}$$

Here, P_0 is the total power radiated from the luminescent particle and angles α and β are shown in Figure 2.10. Then, angles α and β are rewritten in terms of the observation angles θ and ϕ:

$$dP = \frac{P_0}{4\pi} \sin[\alpha(\phi,\theta)] \left[\frac{\partial\alpha}{\partial\phi}d\phi + \frac{\partial\alpha}{\partial\theta}d\theta\right]\left[\frac{\partial\beta}{\partial\phi}d\phi + \frac{\partial\beta}{\partial\theta}d\theta\right] \tag{2.19}$$

This equation is further rewritten into equation (2.20) by disregarding quadratic terms in $d\alpha$ and $d\beta$:

$$dP = \frac{P_0}{4\pi}\sin[\alpha(\phi,\theta)]\left\{\left|\frac{\partial\alpha}{\partial\phi}\frac{\partial\beta}{\partial\theta}\right| + \left|\frac{\partial\alpha}{\partial\theta}\frac{\partial\beta}{\partial\phi}\right|\right\} d\phi\, d\theta \tag{2.20}$$

From equation (2.20), the intensity can be shown as a function of θ and ϕ after dividing by the infinitesimal area $\sin(\theta)\, d\phi\, d\theta$:

$$I(\phi,\theta) = \frac{P_0}{4\pi}\frac{\sin\alpha(\phi,\theta)}{\sin\theta}\left\{\left|\frac{\partial\alpha}{\partial\phi}\frac{\partial\beta}{\partial\theta}\right| + \left|\frac{\partial\alpha}{\partial\theta}\frac{\partial\beta}{\partial\phi}\right|\right\} \tag{2.21}$$

Chapter 3

Methodology

This chapter outlines the methodology in this thesis. ANSYS SPEOS was used to test the luminescent solar concentrator model and how accurate the software can estimate the optical efficiency and losses. First, a red-dye LSC was modeled based on a commercial sample. Ray-tracing simulation results will be compared to the optical efficiency and losses of experimentally measured results of a red-dye LSC sample. Second, a two-layer LSC with silicon quantum dots embedded in a thin copolymer film will be modeled on top of a glass waveguide. Finally, the simulation results of the optical efficiency and losses in the QD LSC model are obtained.

In section 3.1, a brief introduction to ANSYS SPEOS is presented. Then, descriptions of a red-dye LSC model and a quantum dot LSC model are discussed in sections 3.2 and 3.3, respectively. Finally, section 3.4 discusses the simulation procedure to obtain optical efficiency and losses in the red-dye and quantum dot models.

3.1. ANSYS SPEOS Simulations

The main purpose of this project is to characterize the performance of a thin-film luminescent solar concentrator-based model. Different models are implemented in the ray-tracing software. ANSYS SPEOS is a physics-based light modeler. This Multiphysics platform uses Monte-Carlo (MC) ray tracing method to perform interactive ray-tracing in three-dimension. The model simulates light from source to sensor, predicts hot spots, and validate the system performance.

The assumptions in the simulation of LSC model in ANSYS SPEOS include:

- A light is assumed to have a normal incidence angle relative to the front surface of the LSC, even though AM 1.5 G solar spectrum includes both direct and diffuse light.
- Sunlight is unpolarized.
- The refractive index of the red-dye waveguide and copolymer film in the QD LSC waveguide is constant and independent of the photon wavelength.
- The luminescent particles are uniformly distributed throughout the LSC volume.
- For the red-dye model, 10% visible light absorption is in the PMMA waveguide.
- The photoluminescent quantum yield of the luminescent material is constant.
- Reflection at the edges of the waveguide is ignored. The PV edges have 100% absorption where all the rays reaching this area are absorbed.
- Isotropic scattering emission is in the luminescent particles.
- No impurities are in the waveguide.

3.1.1. Monte Carlo ray-tracing algorithm

A Monte Carlo simulation for photon transportation, also known as ray-tracing, is a common technique in LSC research, where the numerical analysis is based on random number generation [62]. A single photon path is computed using the set of initial conditions, including the light source spectrum ($S(\lambda)$), size and the reflective index of the LSC, and the properties of luminescent particles: Absorption spectrum ($A(\lambda)$), emission spectrum ($E(\lambda)$), and quantum yield [63]. The ray will be followed until it leaves the system, or is absorbed by the system and not emitted again.

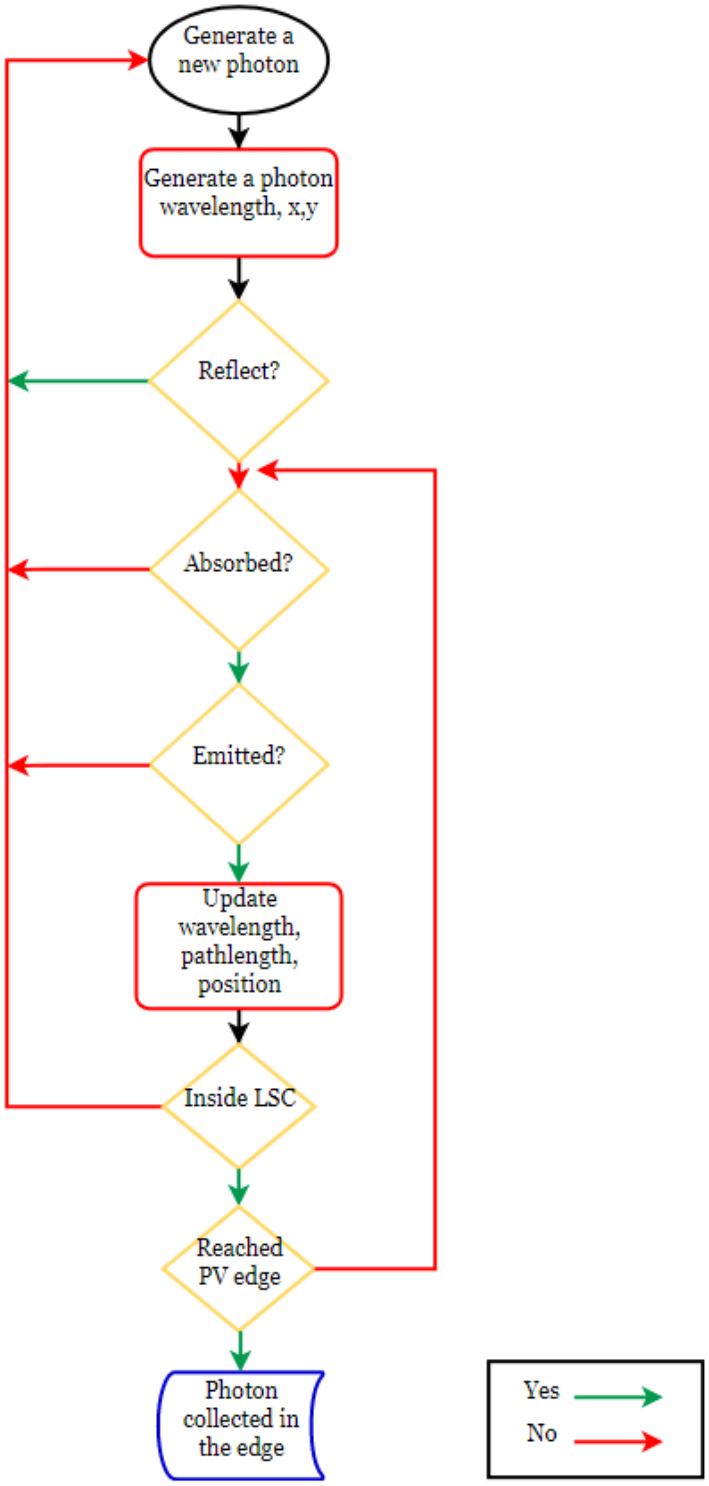

Figure 3.1: Flowchart of a schematic representation of the Monte Carlo ray-tracing algorithm.

Simulation input parameters include:

- Number of incident photons (1,000,000).
- Position and direction of incident light (AM1.5 spectrum).
- The size of the LSC.
- Refractive index and absorption coefficients of waveguide material.
- PLQY.
- Absorption and emission spectra of the luminescent particle.

In ray-tracing random numbers are used to determine the progress of the ray propagation [64]. Situations where the ray is determined by random numbers are:

- Reflection and transmission at interfaces.
- Absorption in the waveguide.
- Absorption by the luminescent particle.
- Emission by luminescent particle. In the emission process, PLQY is considered.
- Wavelength of emission.
- Direction of emission.

The software generates a photon from the light source with wavelength calculated from the probability density equation for a random number generated $\xi \in [0,1]$.

$$\frac{1}{K}\int_0^{\lambda_{em}} S(\lambda)\, d\lambda = \xi, \tag{3.1}$$

where K is a normalization constant,

$$K = \int_0^{\infty} S(\lambda)\, d\lambda. \tag{3.2}$$

Once the wavelength is assigned to the photon, it will emit from the source [63]. Once the photon interacts with the material, the boundary of the LSC is used to determine the direction of the photon propagation where the probability for reflection and transmission will depend on the Fresnel equation (equation 2.5). The inside boundaries are constrained by Snell's Law (equation

2.6) to determine if rays are escaped or TIR. When the photon is an absorbing region, the probability of a photon being absorbed can be described by the Beer-Lambert law,

$$p(L,\lambda) = 1 - 10^{-\varepsilon(\lambda)CL}, \tag{3.3}$$

where C is the concentration of the absorbing material, $\varepsilon(\lambda)$ is the extinction coefficient of the absorbing material, and L is the path length where the point that the photon will be absorbed [65]. The path length is calculated by replacing the absorption probability with a random number generated from a uniform distribution within [0,1].

$$L = \frac{1}{\varepsilon(\lambda)C} log_{10}\big(1 - p(L,\lambda)\big) \tag{3.4}$$

This equation describes the propagation of photons inside the LSC, where the path will determine the photon absorption point. If this path is longer than the dimensions of the LSC, then the ray will go through Fresnel equation again to determine the next photon propagation. When a photon is absorbed by a luminescent particle, the quantum yield determines if the photon will be re-emitted or lost. A photon is re-emitted only if,

$$p(L,\lambda) < QY, \tag{3.5}$$

where QY is the ratio between absorbed and emitted photons [62]. If a photon is re-emitted, then the direction and the wavelength of the new photon is determined. By generating a random vector on a unit sphere, the direction of the re-emitted photon can be obtained. The unit sphere is based on the isotropic emission and the center is the point of absorption. The new wavelength is calculated by a similar method as in equation 3.1, using the emission spectrum (E(λ)) from the luminescent particle. The new wavelength is longer after re-emission, as the re-emitted photon energy is lower than the absorbed photon energy [63].

$$\frac{1}{K}\int_{\lambda_{abs}}^{\lambda_{em}} \mathrm{E}(\lambda)\, d\lambda = \ \xi, \tag{3.6}$$

where K is a normalization constant,

$$K = \int_{\lambda_{abs}}^{\infty} \mathrm{S}(\lambda)\, d\lambda. \tag{3.7}$$

Depending on the random path, a photon can be trapped by internal reflection from all faces of the LSC. If the photon is re-emitted, its wavelength, position, and direction are updated. Then the photon will propagate to the next interaction and the process repeats.

Two different LSC models are created and configured for the simulations in ANSYS SPEOS. This is illustrated in Table 3.1. Model 1 (red-dye model) will be used to implement an experimental sample. Model 2 (quantum dot model) is used to find the optimum parameters of LSC with silicon quantum dot particles.

Table 3.1: Outline of LSC configurations between red-dye and QD LSC model.

	Model 1: Red-dye LSC	**Model 2: Quantum dot LSC**
Objective	ANSYS SPEOS will be used to model a red-dye LSC device and test how accurate this ray-tracing model is compared to experimental results.	The optimum parameters of a Si-QD ray-tracing model will be analyzed.
LSC Model	PMMA thickness of 3.2 mm is doped with Lumogen F Red305 dyes.	Two-layer LSC with silicon quantum dots embedded in a thin copolymer film will be modeled on top of a glass waveguide.
Light source Setup	A laser beam wavelength of 425 nm, hitting the red-dye model from a 20 mm distance from the PV edge.	AM1.5 solar light interacts perpendicularly with the LSC model's top surface of the copolymer film.

3.2. Red-dye model

The main purpose of the red-dye LSC model is to compare simulation results with experimental results of a commercialized dye sample. In addition, the ray-tracing software is used to validate the optical efficiency and losses of the proposed LSC model.

The waveguide is doped with red-dye luminescent particles, which are distributed homogeneously. This polymer has a 1.5 refractive index and an absorption coefficient of 0.033 mm^{-1}, which is obtained by the Lambert-Beer law equation (equation 2.8). The PMMA thickness is x = 3.2 mm, and light transmittance is $I/I_0 = 0.9$ when the waveguide absorbs 10% of the visible light. The polymer waveguide is modeled with no impurities, and it is surrounded by air ($n_0 = 1.0$). Using ray-tracing software, a luminescent particle Lumogen Red F305 is modeled in a PMMA waveguide.

For the red-dye model, a constant absorption coefficient of 0.033 mm^{-1} in the visible range up to 600 nm, then ten times lower absorption coefficient in the emission range up to 800 nm, and finally no absorption in the NIR spectrum ($\lambda \geq 900$ nm) are assumed [28] [66].

3.2.1. Mean Free Path

Equation (2.11) shows that MFP is inversely proportional to luminescent particle concentration. In luminescent particles, blue photons have smaller MFP as they are likely to be absorbed. While red photon emits with longer wavelength and have longer MFP as there is no absorption by luminescent particles. To this end, MFP ratio ($\mathcal{R}$) is defined as the coefficient between MFP after and before emission [28].

$$\mathcal{R} = \frac{Red\ MFP}{Blue\ MFP} \tag{3.8}$$

'Blue MFP' is referred to as the MFP in the wavelength range $\lambda \leq 601\,nm$ and, 'Red MFP' is the MFP in the wavelength range $\lambda \geq 601\,nm$. (See Figure 3.2)

3.2.2. Absorption and emission spectra

Luminescent particles are modeled using Lumogen Red F305 characteristics by BASF [67]. The absorption and emission spectra of the red-dye particles (see Figure 3.2) are used in the LSC model. In this spectrum, the absorption peaks are 442 nm and 553 nm, and the maximum point is 575 nm. The emission peak is 610 nm, and the Lumogen Red 305 presents a maximum quantum yield of 93% in the whole absorption range.

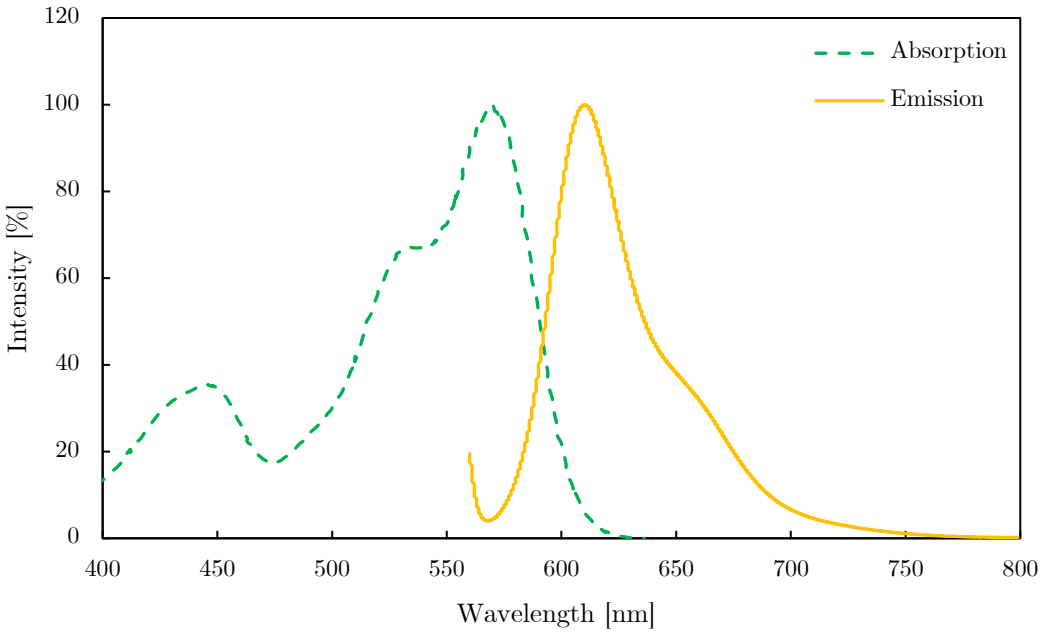

Figure 3.2: Absorption (green dashed lines) and emission (orange solid lines) spectra of Lumogen F Red 305 red-dye particles (Figure adopted from BASF [67]).

3.2.3. Photon-phosphor interaction

Interactions of a photon with a luminescent particle can either lead to its absorption or scatter by the luminophore. If an absorption occurs, photons will be converted to heat or into lower energy photons, and excess energy will be thermalized. In ANSYS, the scattering property for the red-dye model is 'isotropic', meaning that light scatters equally in all directions. Even though scattering by red-dyes molecules might not have an isotropic angular distribution, an isotropic scattering in red-dye based models is assumed for the scope of the thesis [28] [68].

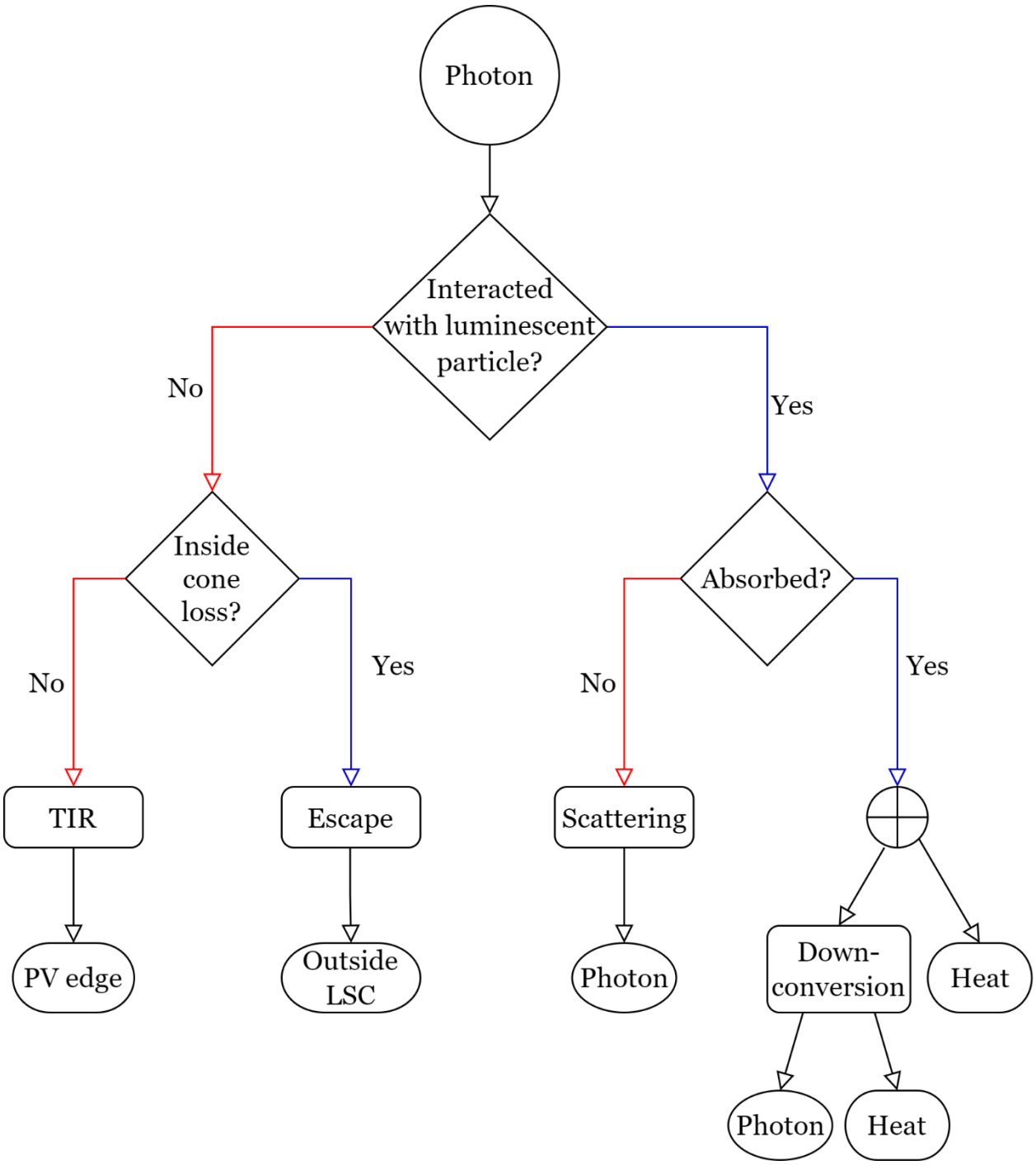

Figure 3.3: Flowchart of photon interaction with a luminescent particle.

3.2.4. Model geometry and optical characteristics

Figure 3.4 is a schematic representation of a red-dye model, which has the dimensions of a real sample: L = 100 mm, H = 24.5 mm, and W = 3.2 mm (thickness). The LSC size is A= 24.5 cm^2 and the PV edge area is 0.784 cm^2.

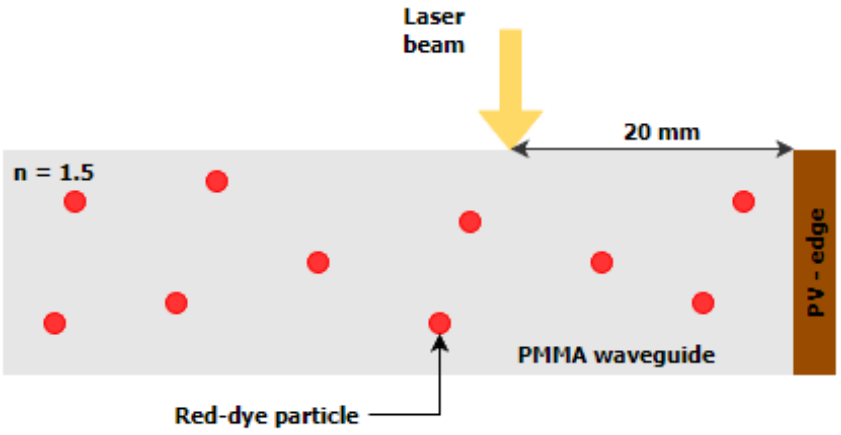

Figure 3.4: Schematic drawing of a red-dye model infused in a PMMA waveguide. A light beam hits the LSC surface at 20 mm from the PV edge.

Front and back surfaces are specified as Fresnel type. The PV edge serves as a perfect absorber since all the light reaches this area. The other three edges are also defined as 100% absorption (these edges are painted black in the real sample) [28].

3.3. Quantum dot model

A quantum dot LSC model is proposed for ray-tracing simulation. The QD LSC is construct by embedding QDs on a copolymer film and placed on top of a transparent waveguide. The QD model is proposed to obtain optical efficiency using different quantum dot sizes and LSC geometry. There are three main parameters to discuss; (1) Waveguide of glass layer; (2) Waveguide of copolymer layer; (3) Silicon quantum dot luminescent particles.

3.3.1. Waveguide: Low-Iron and regular glass layer

A low-iron glass waveguide with dimensions of L = 150 mm, H = 150 mm, and d = 6 mm with a refraction index variation shown in Figure 3.5 is modeled with an absorption variation of glass material in Figure 3.6. The model is surrounded by air, and it is assumed that there are no impurities in the solid.

AQM has provided the extinction coefficient data for the low-iron and regular glass in different wavelengths. Since ANSYS software package uses the absorption coefficient when creating the material, the extinction coefficient data is used to obtain the absorption coefficient using equation (2.4). In Figures 3.5 and 3.6, a comparison between a low-iron and a regular glass of refractive index and absorption coefficient is shown, respectively.

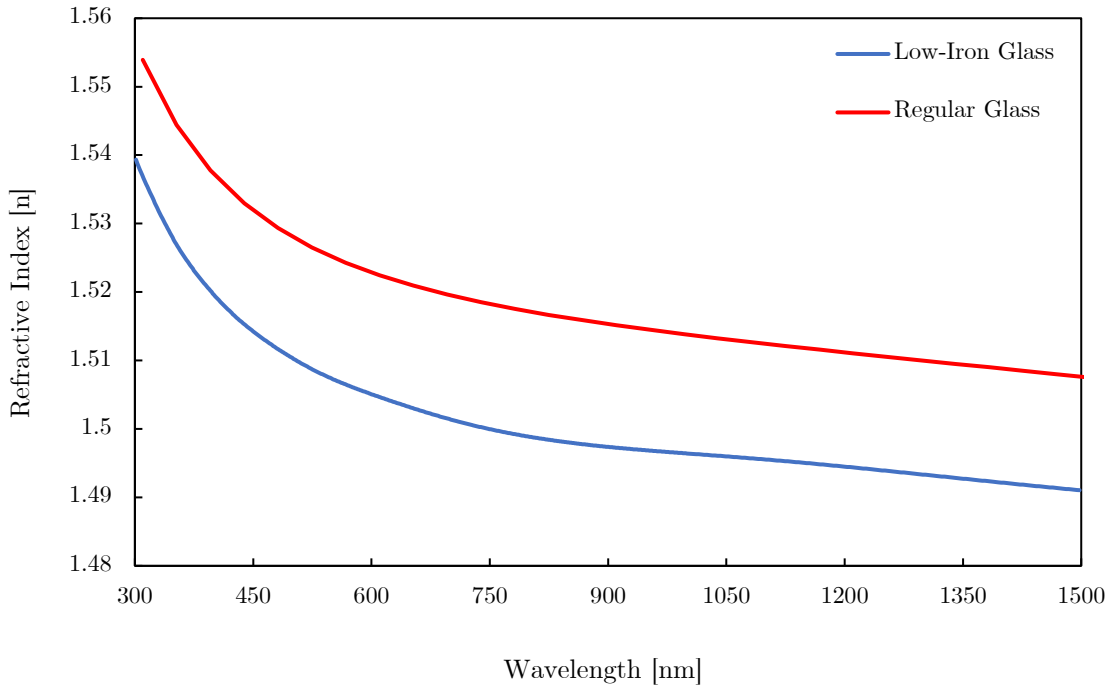

Figure 3.5: Refractive index variation of glass. (Data obtained from AQM [69])

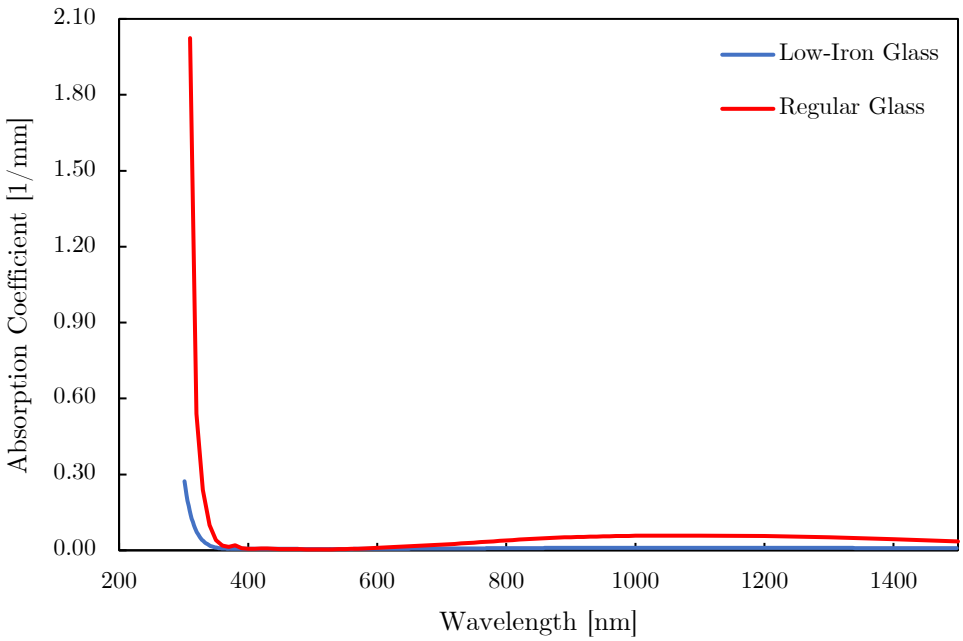

Figure 3.6: Absorption variation of glass. (Data obtained from AQM [69])

Regular glass has a higher absorption in the wavelength range of 600-1500 nm compared to low-iron glass (see Figure 3.6). For the Si-QD LSC model, low-iron glass is used as the waveguide to guide the light to edges of the glass. This is because low-iron glass has lower absorption than regular glass, resulting in higher transmittance (see Figure 3.7).

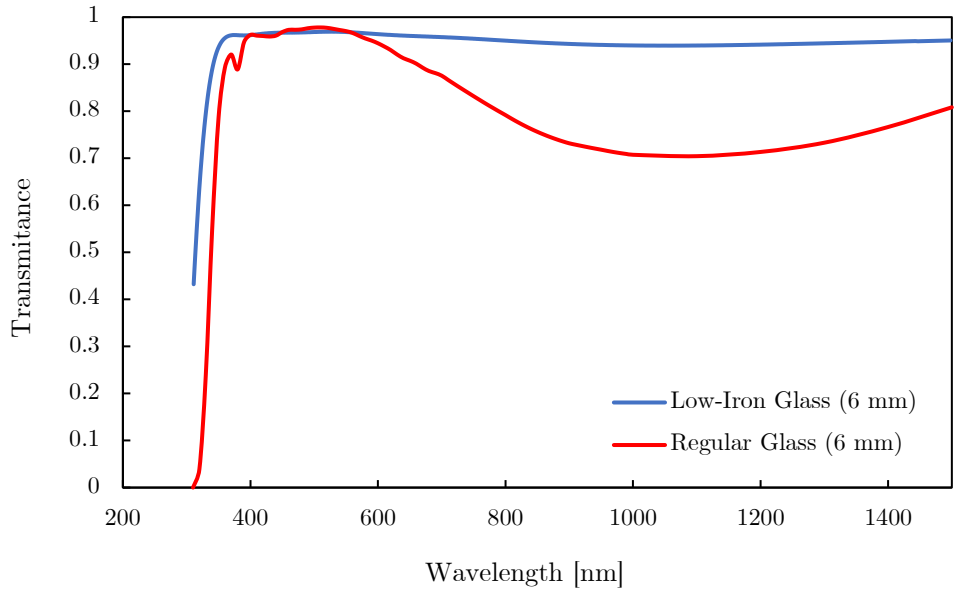

Figure 3.7: Transmittance of Low-Iron vs Regular glass. (Data obtained from AQM [69])

3.3.2. Waveguide: Copolymer layer

The copolymer film, known as Poly (butyl methacrylate-co-methyl methacrylate), is modeled above the glass component with dimensions of L = 150 mm, H = 150 mm, and W = 0.1 mm with a refractive index of 1.486. The transmittance data obtained from AQM is used to calculate the absorption coefficient using equation (2.8). Figure 3.8 shows the absorption variation throughout the whole wavelength, which is used to create the copolymer film in the ray-tracing software.

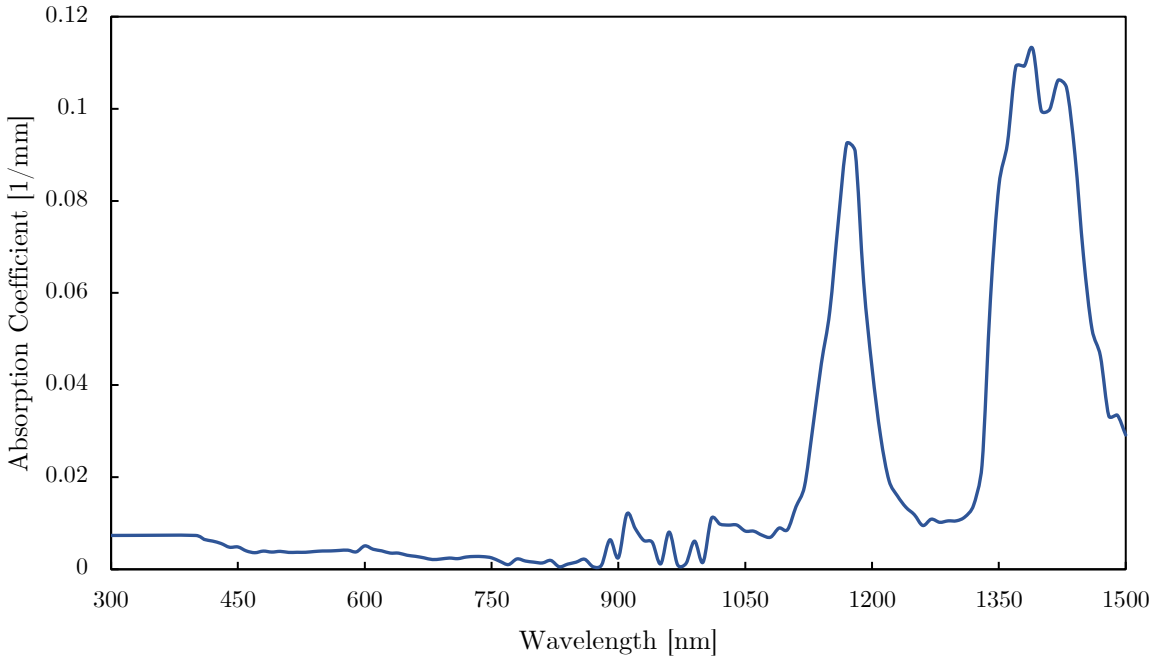

Figure 3.8: Absorption variation of the copolymer film. (Data obtained from AQM [69])

3.3.3. Luminophore: Silicon quantum dots

Figures 3.9, 3.10, and 3.11 correspondingly represent 3 nm, 4 nm, and 7.5 nm quantum dot size photoluminescence (PL) spectra that is obtained from AQM. The absorption spectrum (green dashed line) shows the change in absorption of a sample, as a function of the wavelength of incident light. The emission spectrum (orange solid line) shows the change in fluorescence intensity as a function of the wavelength of the emission light, which is measured using a spectrofluorometer.

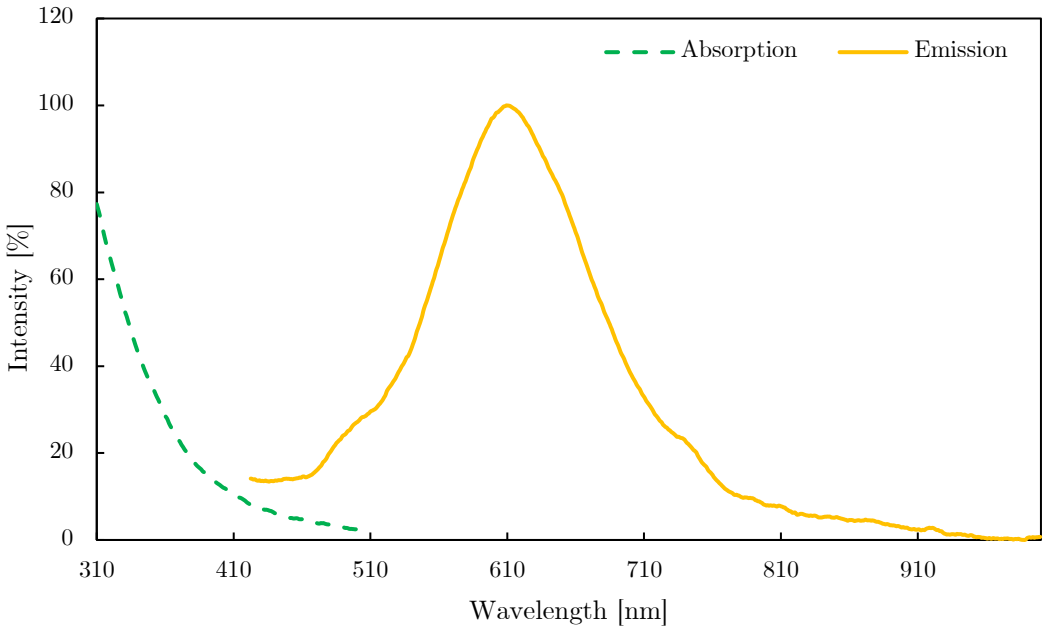

Figure 3.9: Absorption and Emission Spectrum of a 3 nm size QD. (Data obtained from AQM [69])

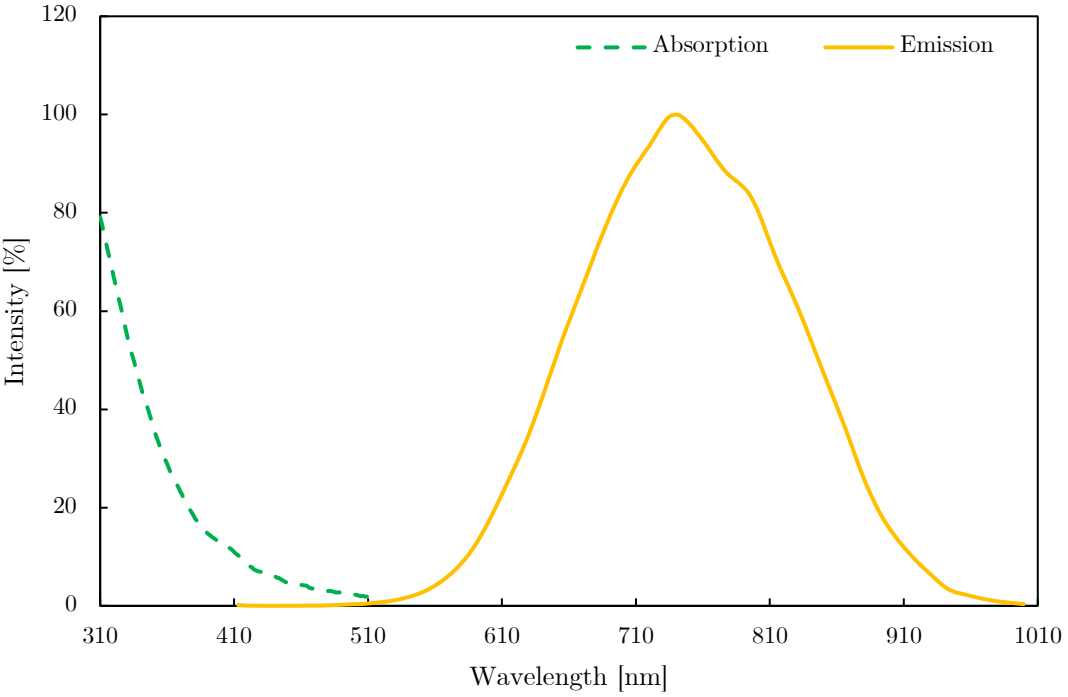

Figure 3.10: Absorption and Emission Spectrum of a 4 nm size QD. (Data obtained from AQM [69])

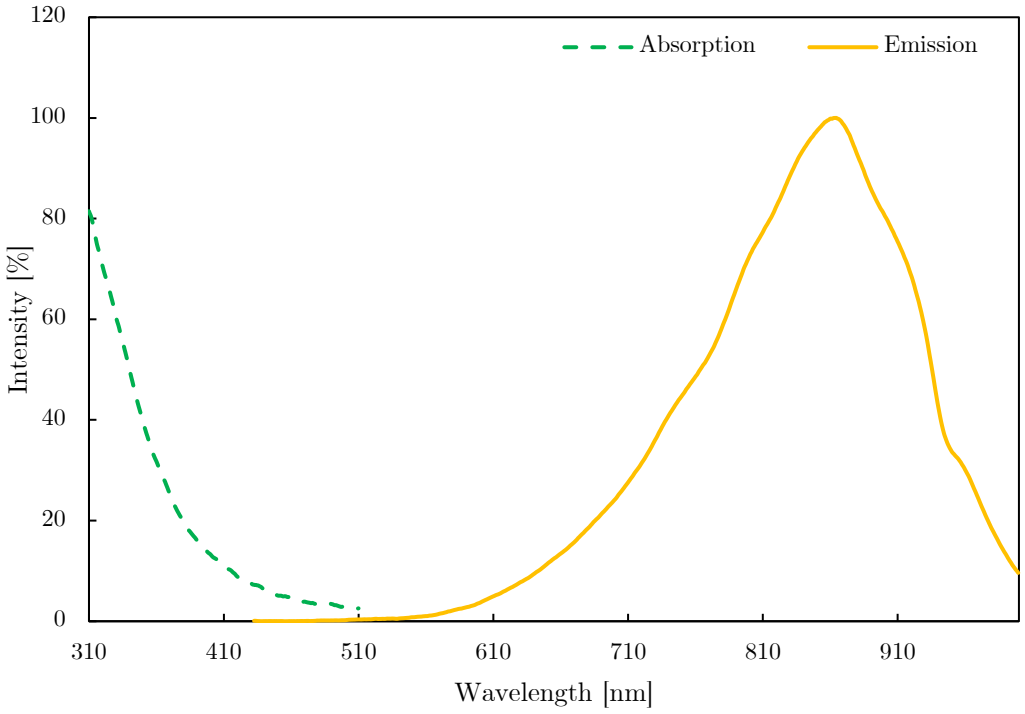

Figure 3.11: Absorption and Emission Spectrum of a 7.5 nm size QD. (Data obtained from AQM [69])

The concentration of Si-QD in the LSC model is given by w/w %, where the concentration of Si-QD in the copolymer to be simulated is 0.5% (w/w) as informed by AQM. Equation (3.9) is used to calculate the number of Si particles per unit volume [70]. Polymer film and silicon density were assumed to be 1.1 g/cm^3 and 2.33e-21 g/cm^3, respectively, as informed by AQM.

$$Concentration\ \%\ (w/w)\ =\ \frac{Mass\ of\ solute}{Mass\ of\ solution} \times\ 100\% \tag{3.9}$$

3.3.4. Model geometry and optical characteristics

Figure 3.12 is a schematic representation of QD-based model, which has the dimensions L = 150 mm, H = 150 mm, and W = 6 mm. This model includes a uniform coating film of 0.1 mm thickness on the glass waveguide. All four PV edges are considered perfect absorber, which receives all the light. Front and back surfaces are defined as Fresnel type in the QD model.

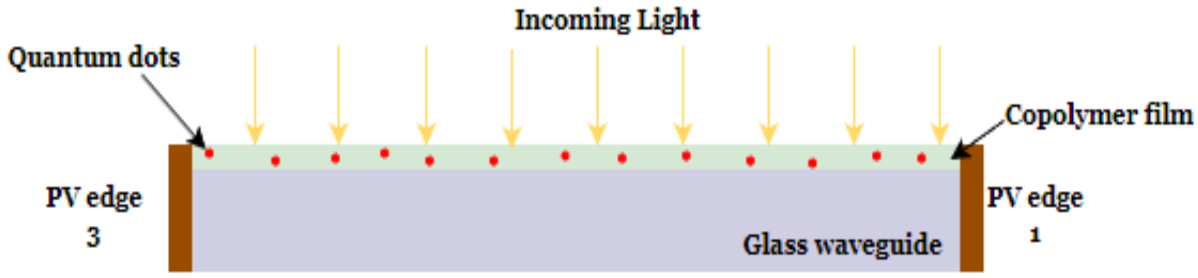

Figure 3.12: Schematic representation of a QD-based LSC model.

3.4. Simulation procedure

ANSYS SPEOS simulation procedure has two parts: First is the ray-tracing of a red-dye LSC model, and second is the ray-tracing of a quantum dot model. The red-dye LSC model utilizes ANSYS SPEOS to validate with a commercial sample. The optical efficiency and losses from the simulation results will be compared to the laboratory measurements by Lisset Manzano Chávez [28]. Once ANSYS results is proven accurately, this procedure can be extended to the quantum dot model.

In the red-dye simulation model, MFP length and ratio parameters are changed as they are unknown parameters of the sample. To estimate the LSC optical efficiency and power losses, a 'loss detector model' that was described in section 3.4.1 is used for the simulation. A light beam source of an emitting power of 100 W at a wavelength of 425 nm is used to hit the red-dye model 20 mm away from the PV edge, shown in Figure 3.4.

In the quantum dot simulation model, some parameters are kept constant and others are used as variables for testing purposes. For example, the absorption and emission spectrum of the QD and absorption coefficient of copolymer and glass are kept the same when other LSC parameters are tested. Variable parameters tested in the quantum dot LSC are QD concentration, quantum yield, glass thickness, copolymer thickness, and LSC size. To estimate the QD LSC model optical efficiency and power losses, a 'loss detector model' proposed in section 3.4.2 is used for the simulation. For the QD model, sunlight is used as the light source of the total front area of the LSC device. The solar light incident is perpendicular on the front surface of the LSC model. Figure

3.13 is a plot of AM1.5 Global solar spectrum obtained from the national renewable energy laboratory (NREL), which is used for flat plate modules and has an integrated power density of 1000 W/m^2. [71]

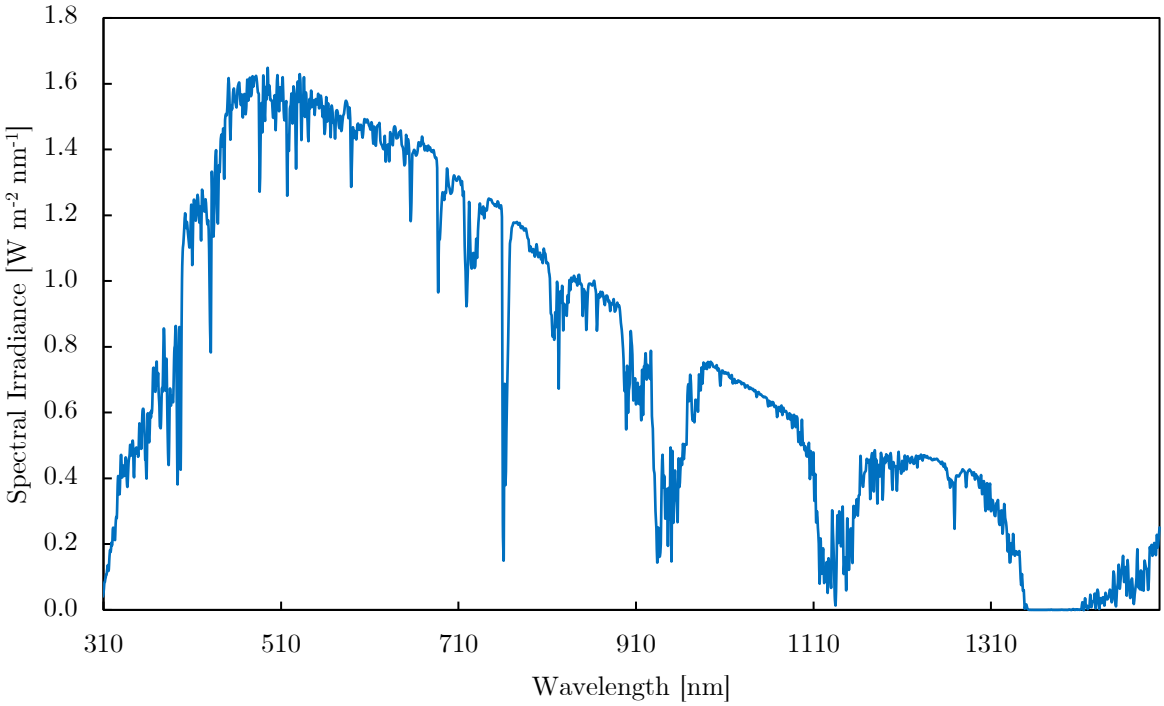

Figure 3.13: AM 1.5 Solar Spectrum from 310 nm to 1500 nm. (Data obtain from NREL [71].)

3.4.1. Estimations for the red-dye model

The main objective of this thesis is to estimate the LSC optical efficiency to optimize the power output produced by a PV cell attached to the waveguide. The optical efficiency is obtained by equation (2.13) in Chapter 2. The PV edge is defined as a perfect absorber to receive all the light by the sensor. In simulations, light input is 100 W, and output of the PV edge is measured in watts. From this, the optical efficiency can be obtained by:

$$\eta_{opt} = \frac{Output\ power\ in\ PV\ edge\ [W]}{100\ W} \tag{3.10}$$

Different sensors are placed around the model to identify the losses from the LSC. Figure 3.14 shows a schematic representation of an ANSYS model, which places sensors to measure the optical efficiency and losses. One sensor is placed on top of the model to detect the reflected light (green sensor), and another is placed on the bottom to see transmitted light (blue sensor). The reflection (R) and transmission (T) sensors are larger than the LSC surface, detecting all the light coming from the top and bottom of the LSC. The waveguide or luminescent particles absorb light, which is not reflected or transmitted. Some of this absorbed light reaches the PV edge, and the remaining will be lost due to thermalization and absorption by the other three edges of the waveguide. The final sensor is placed on the PV edge to collect light and estimate LSC efficiency.

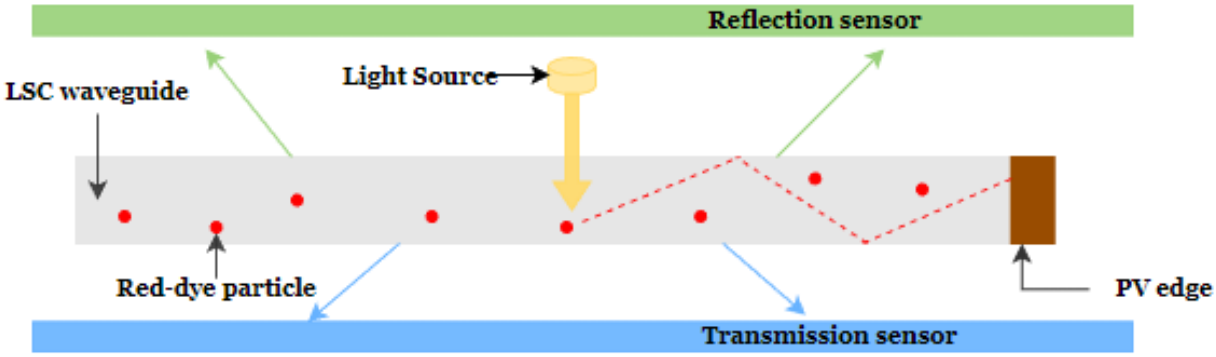

Figure 3.14: Schematic diagram of the ANSYS model to detect different losses in the red-dye LSC.

In this validation model, the optical efficiency is obtained only from one PV edge to match the experimental red-dye setup. The total light outcome in the red-dye LSC model can be shown as equation (3.11);

$$Total\ light\ outcome = n_{opt} + R + T + Other = 100\% \tag{3.11}$$

Here, the 'other' corresponds to the remaining light to complete a 100% total light outcome. In this validation model, the simulation results obtained from the red-dye model should have similar results to the laboratory measurements of optical efficiency and losses with a low error.

3.4.2. Estimations for the quantum dot model

In the QD LSC model, the optical efficiency is obtained by equation (3.12), where the output power is measured in watts from all four PV edges in the LSC device. The PV edges are defined as perfect absorber to receive all the light by the sensors. The solar light radiant power is 22.5 W for the LSC size of 15 cm. The optical efficiency can be obtained by:

$$\eta_{opt} = \frac{Collected\ power\ in\ all\ four\ PV\ edges\ [W]}{Incident\ power\ [W]} \tag{3.12}$$

Various sensors are placed around to collect light from the LSC, such that we can identify different losses in a QD LSC model. Figure 3.15 shows a schematic representation of where the sensors are placed in the LSC model. Four sensors are placed on all four PV edges (brown sensors), one sensor is placed on top of the model to detect the reflected light (green sensor), and another sensor is placed on the bottom of the model to see transmitted light (blue sensor). In this QD LSC model, the optical efficiency is obtained by including the power output of all four PV edges.

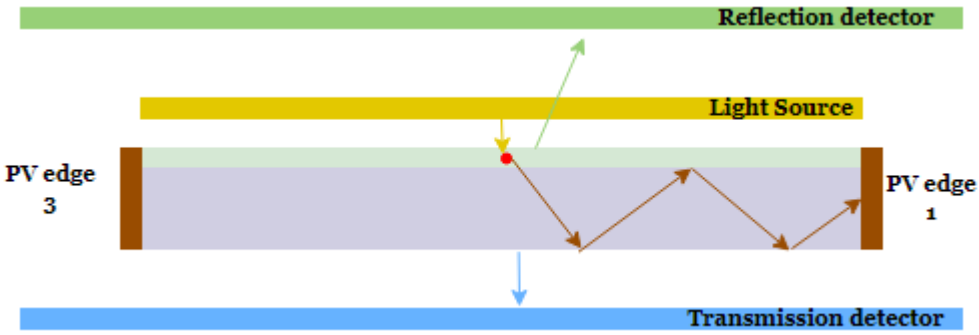

Figure 3.15: Schematic diagram of the ANSYS model to detect different losses in the QD LSC.

Chapter 4

Validation of red-dye LSC model

This chapter evaluates the ANSYS accuracy of in simulating an LSC device to using the ray-tracing model is accurate. The loss detector model proposed in Chapter 3 (section 3.4.1) is modeled in ANSYS and the optical efficiency and losses are compared to an actual LSC sample (PMMA doped with Lumogen F Red-305).

Section 4.1 discusses additional parameters regarding red-dye and simulation results of a red-dye LSC model. Then, section 4.2 presents the main experimental results of optical efficiency and losses. Finally, section 4.3 discusses the findings and conclusions of the validation model of the red-dye LSC.

4.1. Simulations of a Red-dye model

As discussed in Chapter 3, the red-dye model is based on an LSC sample, where the parameters of the optical and geometry of the model are fixed in ANSYS. Red-dye concentration in the PMMA waveguide is unknown. Therefore, the MFP is unknown.

The main standard LSC parameters for the red-dye model is shown in Table 4.1. The absorption and emission spectra are shown in Figure 3.2, and the refractive index of 1.5 is set as the additional data for the red-dye model simulation. Red-dye concentration is tested by changing MFP length and MFP ratio (equation (3.8)), which both are related to red-dye concentration.

Table 4.1: Standard LSC parameters for red-dye model [28].

Parameters	**Standard parameters for Red-dye Model**
MFP ratio ($\mathcal{R}$)	$\mathcal{R} = 10$
MFP Length	Blue ($\lambda \leq 600$ nm) MFP: 0.1 mm
	Red ($\lambda \geq 601$ nm) MFP: 1.0 mm
Quantum Yield	$\eta_{QY} = 0.93$

For this simulation, the light source is a monochromatic source at 425 nm, inputting to the model at 20 mm away from the PV edge as a 100 W incident power. Figure 4.1 shows the ray-tracing simulation of the red-dye model. Figure 4.1(a) shows a red-dye LSC ray-tracing simulation and Figure 4.1(b) is the side view of the LSC where rays are waveguided to the PV edge. The intensity map is shown in Figure 4.1(c), where more rays are shown in the center of the PV edge.

First, as the base case of the red-dye model, the MFP ratio is set as 10. This shows that blue photons will have an MFP length of 0.1 mm, and red photons will have an MFP length of 1.0 mm (see Table 4.1). The smaller MFP ratios will result in lower optical efficiency, and larger MFP ratios will have higher optical efficiency as red photons will have larger MFP lengths respect to blue photons. Therefore, photons will travel longer paths to reach the PV edge with less photon absorption with increased of MFP length.

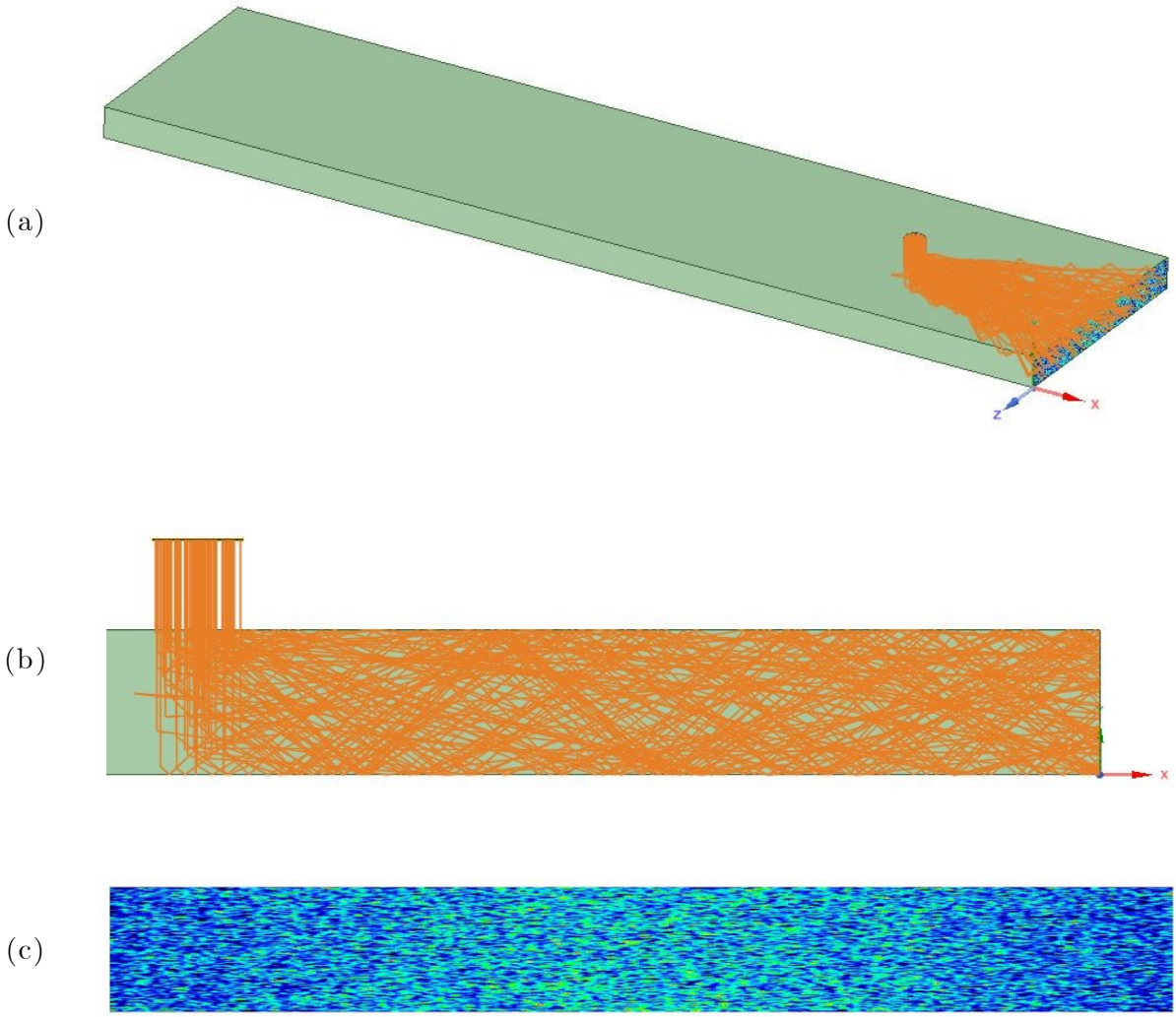

Figure 4.1: Red-dye LSC simulation: (a) 3D view of a ray-tracing in a red-dye LSC model. (b) Side view of the LSC model showing ray-tracing. (c) Intensity map of the LSC PV edge.

The first step involves testing the change in the MFP ratio and how it affects the optical efficiency and losses. In this test, the MFP ratio is increases from 1 to 400, and the blue MFP length is fixed at 2.5 mm. Therefore, red MFP length varies with larger MFP ratios. Figure 4.2 represents the power losses and optical efficiency when increasing the value of MFP ratio ($\mathcal{R}$).

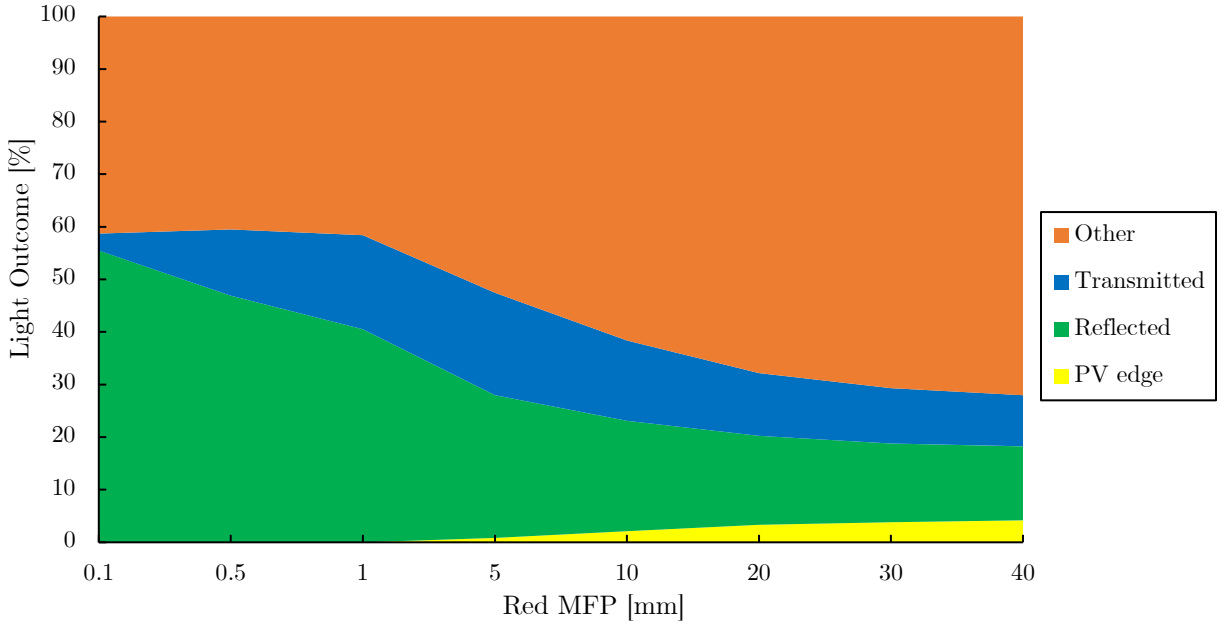

Figure 4.2: Ray-tracing simulation results of a red-dye model by increasing MFP ratio and fixing blue MFP length at 2.5 mm.

Figure 4.2 presents the simulation results for the red-dye model when the MFP ratio is increased from $\mathcal{R} = 1$ (Red MFP length = 0.1 mm) to $\mathcal{R} = 400$ (Red MFP length = 40 mm). Here, the orange area represents the thermalization losses and absorbed light by the other LSC edges, except for the PV edge. The blue area represents transmitted light by the LSC, the green area represents the reflected light from the LSC, and the yellow area shows the optical efficiency of the PV edge. The graph shows that the optical efficiency increases from the red MFP length of 5 mm. At an MFP length of 10 mm, the optical efficiency is 2.10%, and the maximum efficiency is 4.16% at 40 mm of red MFP length ($\mathcal{R} = 400$).

The major optical losses are thermalization and absorption by the other edges of the LSC. Transmitted light (blue) slightly increases initially and becomes constant at longer red MFP length. Reflected light (green) decreases initially and becomes constant with longer MFP length. The longer MFP ensures that the red photon reaches the PV edge, which results in higher optical efficiency. According to these results, reflected and transmitted light efficiency does not change significantly but effectively increases the optical efficiency with long red MFP length.

In the next simulation of the red-dye model, MFP ratio is fixed at 100, while changing the MFP lengths. Figure 4.3 presents the light outcome of changing the blue MFP length from 0.1 mm up to 4 mm. In this figure, transmitted light has a larger variation when the blue MFP length increases, while reflected light slightly decreases with a larger MFP length. Other losses, which include thermalization and absorption by other edges, decrease significantly with larger blue MFP length.

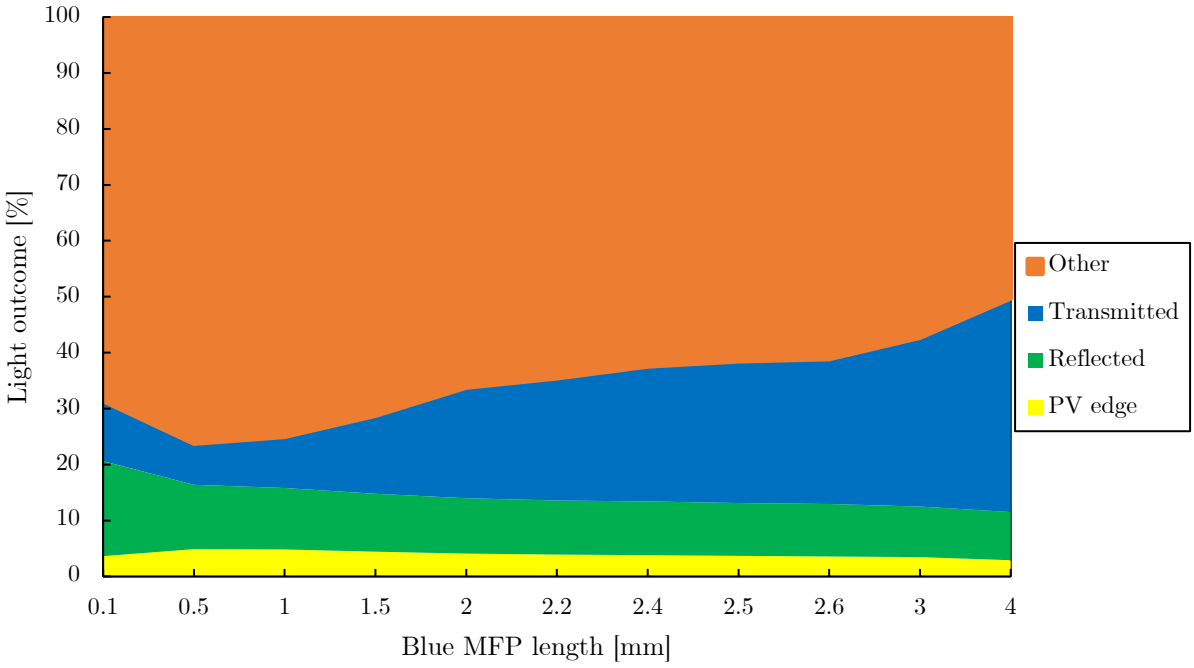

Figure 4.3: Ray-tracing simulation of a red-dye model by fixing MFP ratio and increasing both before and after emission MFP length.

Transmitted light changed drastically when the blue and red MFP lengths were changed, while keeping the MFP ratio constant. As shown in the above graph, the blue MFP length from 1 to 3 mm slightly affects the optical efficiency. The optical efficiency increases when the blue MFP length is lower than 1 mm, and the optical efficiency decreases when the MFP length is longer than 3 mm. The maximum optical efficiency is 4.90% at 0.5 mm of blue MFP length and around 4% from 1.5 mm to 2.5 mm in the blue MFP range. This MFP range will be compared with the optical efficiency of the experimentally measured LSC sample.

4.2. Experimental optical efficiency and losses

Lisset Manzano Chávez [28] presents the experimental optical efficiency of a red-dye sample, which was measured by Overbeek [72] using a 425 nm laser beam which is hitting from a 20 mm distance from the PV edge. Figure 4.4 shows a summary of experimental results of the red-dye sample's total reflection, total transmission, and optical efficiency (output from PV edge).

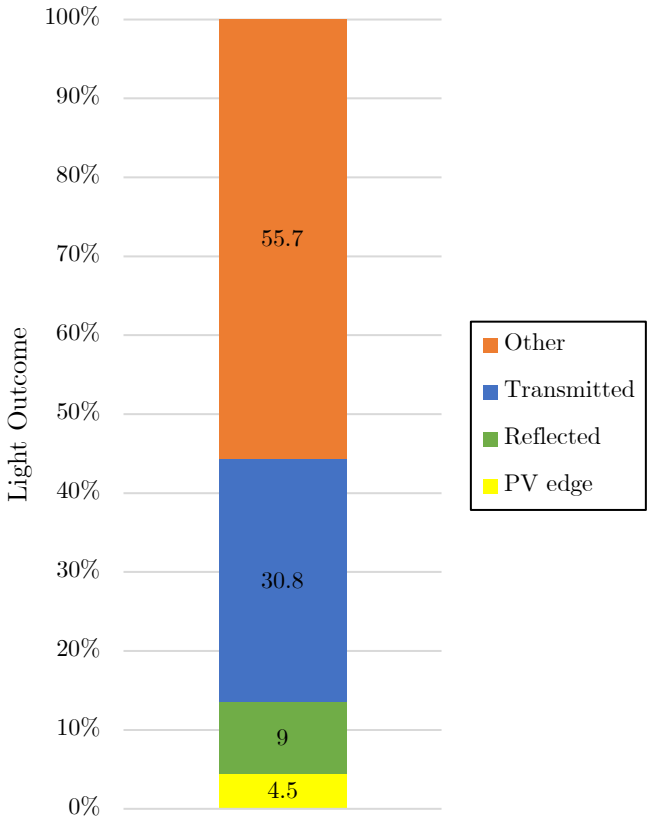

Figure 4.4: Optical efficiency and losses of a red-dye sample. (Figure adopted from Lisset [28])

Figure 4.4 shows that around 4.5% optical efficiency is measured in the red-dye sample. Losses of the LSC are recorded as: Total reflected light with around 9%, total transmitted light that is around 30.8%, and other losses at around 55.7%. Other losses are due to thermalization and absorption by other edges of the LSC, except for the PV edge.

4.3. Discussion of results

One of the objectives in this work was to validate if ANSYS can provide a good tool to obtain accurate simulation results. A LSC composed with PMMA doped with red-dye particles was used to measure the optical efficiency and optical losses (transmission and reflection) for an LSC device. Two parameters are tested during the red-dye simulations: MFP ratio and MFP length (change in red and blue MFP length).

The MFP ratio is initially evaluated by changing the red MFP length. The larger red MFP length increases the optical efficiency, whereas the transmitted light reduces when increasing the red MFP length. In this case, a larger red MFP length means longer paths for the red photons, which increases ray tracing to the PV edge, increasing the optical efficiency. No loss changes occur when the red MFP length is above 20 mm.

The second examination focuses on changing the MFP length, which will be both red and blue MFP lengths. In this simulation, changing the MFP length results in a significant change in the loss outcome. With increasing MFP length, the transmitted light is increased as light can pass through the waveguide easily, while the red-dye concentration is lower. However, the optical efficiency is higher as light is absorbed by the luminescent particles and re-emitted to the PV edge with a lower MFP length.

The second set of simulations (see Figure 4.3) shows similar results to the measured red-dye sample. To compare the simulations with the experimental measured red-dye sample, results with similar optical efficiency and losses from Figure 4.4 is used. Figure 4.5 presents optical efficiency and losses in an LSC sample and simulation results of a red-dye model (three simulation results from Figure 4.3). The blue MFP of 1.5, 2.0, and 2.5 mm were the closest of the simulations results to the experimental measurement shown in Figure 4.3.

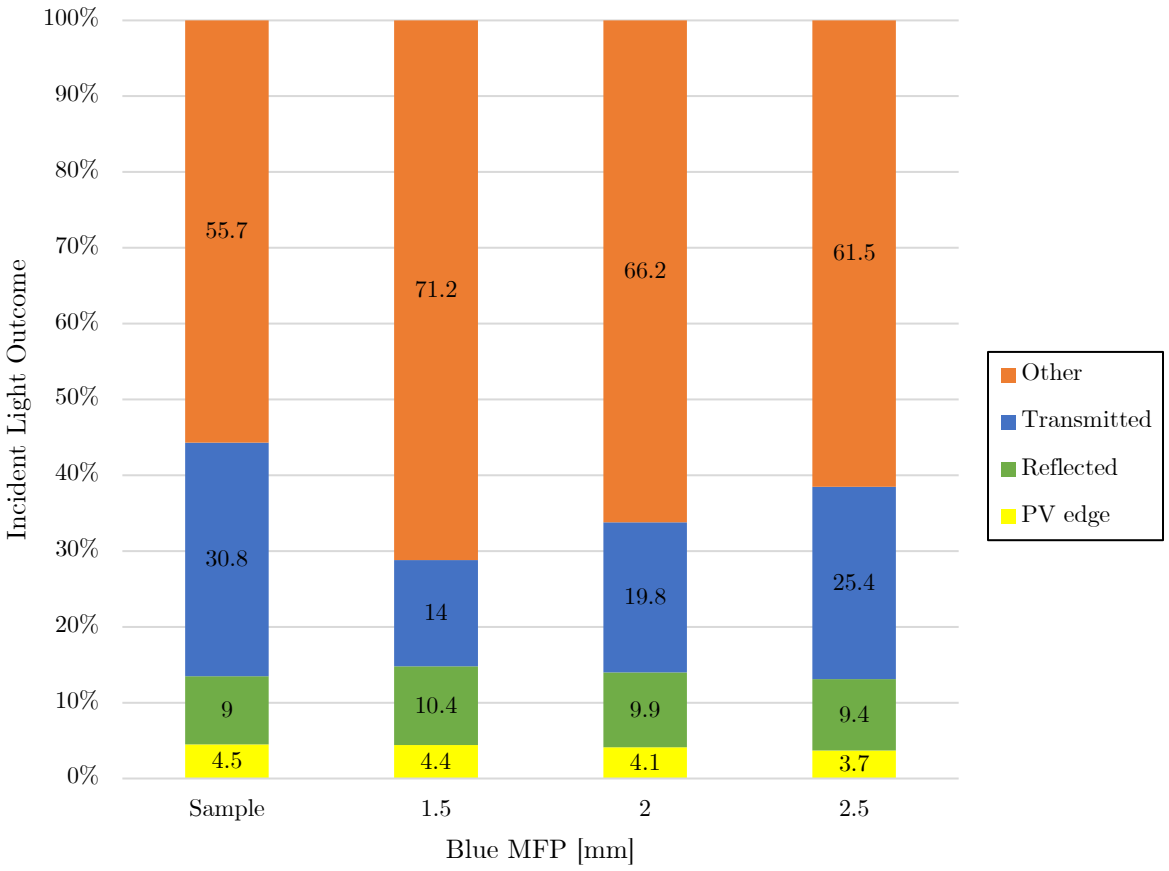

Figure 4.5: Optical efficiency and losses of an experimental red-dye sample and simulations with different blue MFP lengths of 1.5, 2.0, and 2.5 mm.

In blue MFP length of 1.5 mm, the optical efficiency is closer to the experimental sample. However, the transmitted light is too low compared to the experimental sample. The transmitted light increases with increasing MFP, closer to the measured results. Among all the simulation results from Figure 4.5, the best simulation was chosen at 2.5 mm of blue MFP. In this simulation, the optical efficiency and loss mechanisms had similar results closer to the experimental results compared to other simulations. Table 4.2 shows the best simulation results and error respect to the experimental measurements. By comparing the best model simulation with experimental results, the red-dye model was validated with a smaller error. According to Table 4.2, the highest error is shown in other losses, and afterwards in transmitted light. Optical efficiency has an error of 0.8%, and transmitted light with an error of 5.4%.

Table 4.2: Optical efficiency and losses of red-dye sample comparing experimental estimation with the best simulation results (Blue MFP = 2.5 mm), and error of simulations.

Light Outcome	**Experimental Results**	**Best Simulation**	**Error**
Optical Efficiency	4.5%	3.7%	-0.8%
Reflected	9.0%	9.4%	+0.4%
Transmitted	30.8%	25.4%	-5.4%
Other Losses	55.7%	61.5%	+5.8%

The scattering direction of the red-dye molecule depends on the alignment of molecules in the LSC [73] [68]. The isotropic scattering property is a reasonable assumption when simulating the red-dye LSC model as results obtained with a lower error. Chapter 4 concludes that ANSYS SPEOS is a useful ray-tracing tool with great accuracy when modeling the LSC to obtain optical efficiency and losses.

Chapter 5

Quantum dot based LSC model

It was validated in Chapter 4 that ANSYS SPEOS can accurately simulate an LSC model for estimating optical efficiency. This chapter discusses a new luminescent particle known as a silicon quantum dot for the ray-tracing model. This model aims to find the optimal parameters of Si-QD-based LSCs. Simulation of QD LSC models is used to adjust the parameters for the maximum output at the edges of LSCs.

In section 5.1, the outline of the simulation tests is discussed. This section will analyze specific parameters affecting the LSC: QD size, QD concentration, PLQY, glass thickness, copolymer thickness, and LSC area. The obtained information will help select the optimal parameters for increasing the optical efficiency of LSCs. Then in section 5.2, the results of the simulation models are discussed.

5.1. Simulation of the LSC model

Different LSC parameters will be considered during these simulations: Different QD concentrations, QD sizes, PLQY, glass thickness, polymer thickness, LSC area, and when a reflective surface is added on the bottom of the glass. Table 5.1 presents LSC parameters that are used during the simulations. In each simulation test shown in Table 5.1, one parameter is changed, and the rest of the parameters are set to the standard values. In most simulation tests, the ideal condition of 100% PLQY is simultaneously simulated to compare with other results. Each test is simulated by illuminating the LSC with sunlight AM1.5, in the range of 310-1500 nm, hitting the top of the copolymer film. Chapter 3 (section 3.4.2) discussed the loss detection model that is used to obtain optical efficiencies and other LSC losses.

Table 5.1: Summary of LSC parameters which will be simulated in the QD LSC model.

Parameter	**Standard Values**	**Simulation Tests**
QD size	4 nm	3 nm, 4 nm, 7.5 nm
QD concentration	0.5% w/w	0.01; 5% w/w
PLQY	45%	45%, 60%, 100%
Glass thickness	6 mm	1; 10 mm
Copolymer thickness	0.1 mm	0.1; 1 mm
LSC area	225 cm^2	144 cm^2, 225 cm^2, 400 cm^2, 900 cm^2, 3600 cm^2, & 1 m^2

The Si-QD LSC is modeled with two layers where the first layer is embedded with Si QDs, which is doped in the copolymer film, and the second layer is a glass waveguide. This model is simulated in ANSYS, and the ray-tracing is shown in Figure 5.1. This figure shows the ray tracing on one side of the PV edge and demonstrates the intensity map of that PV edge.

(a)

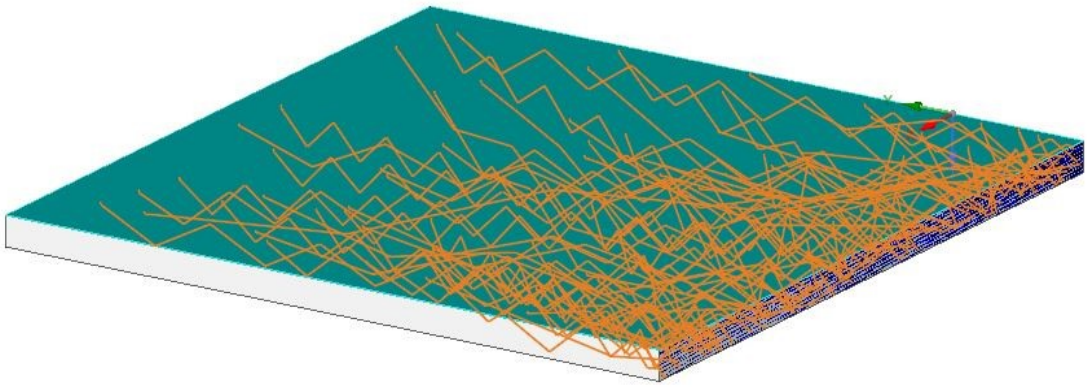

(a)

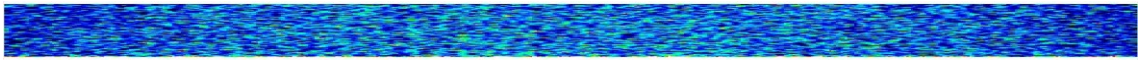

Figure 5.1: Si-QD LSC simulation. (a) Ray-tracing in a Si-QD LSC model. (b) Intensity map of an LSC PV edge.

In Figure 5.2, the optical efficiency and losses are plotted by increasing the concentration of Si-QD in the copolymer film where the standard parameters are used. The yellow area represents the optical efficiency of the LSC device. It is shown that the optical efficiency significantly increases up to 3.49% in a 0.4% w/w QD concentration. Then a maximum optical efficiency of 4.06% is obtained at a 2% w/w QD concentration. Then the optical efficiency slightly decreases. This decrease in optical efficiency is slightly small as the size of the QD particles has smaller cross-section, which results in the scattering effects to become smaller.

In Figure 5.2, 'Other' indicates the absorption and thermalization losses of the LSC. The blue area represents transmitted light from the LSC device. In lower concentrations, transmitted light has a higher loss percentage. The light easily passes through the copolymer and glass as it is not absorbed due to lower QD concentration. On the other hand, there is a constant contribution of reflection losses (green area).

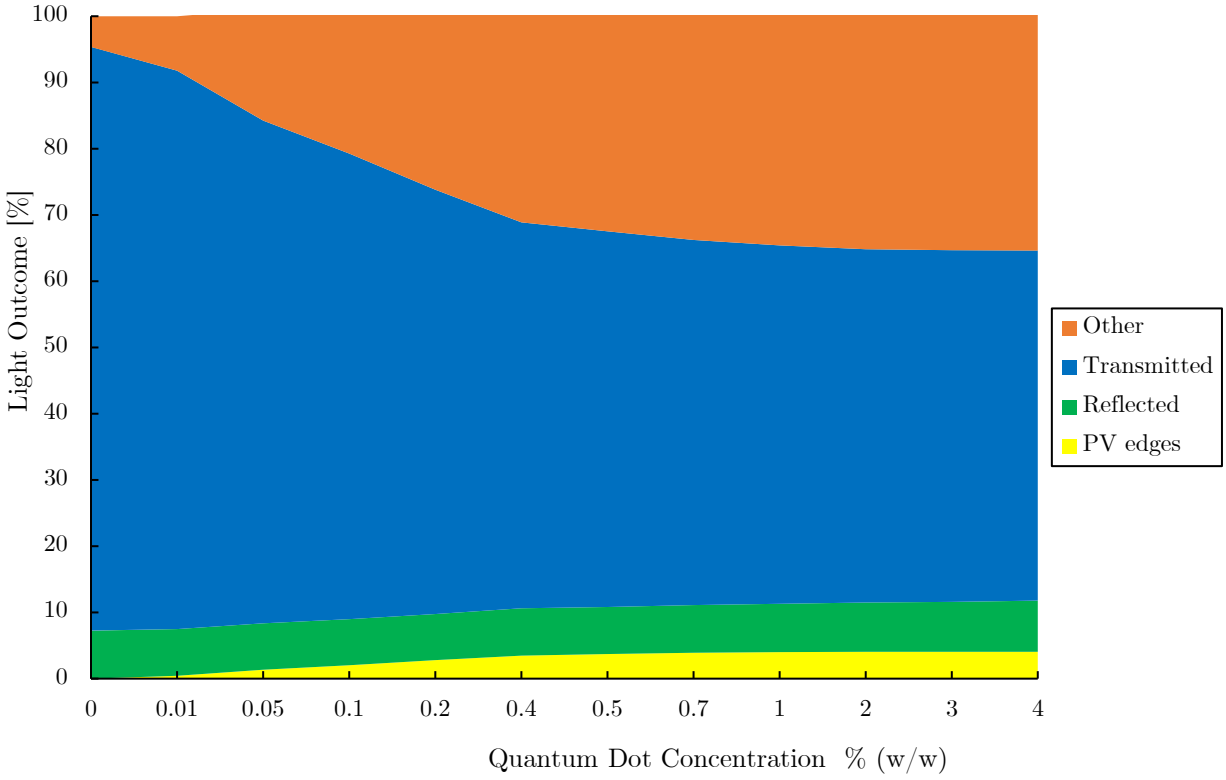

Figure 5.2: Optical efficiency and losses using 4 nm QDs and 45% quantum yield.

The results presented in the following sections will mainly use the standard Si-QD LSC model, a LSC (L = 15 cm, H = 15 cm) with a 6 mm low-iron glass and 0.1 mm copolymer thickness. The copolymer is embedded with 4 nm size quantum dots and 0.5% w/w quantum dot concentration with a 45% PLQY. The optical efficiency from this model is received as 3.70%, 7.10% reflected, and 56.7% transmitted light. The QD characteristics are changed, and the optical efficiency is recorded in the following sections.

5.1.1. Quantum dot sizes

In Figure 5.3, the optical efficiency variation is reached when there are different quantum dot concentrations and sizes. Here, the 'blue solid line' corresponds to a 7.5 nm quantum dot, the 'solid green line' corresponds to a 4 nm quantum dot, and the 'red solid line' corresponds to a 3 nm

quantum dot. The QD concentration inside the LSC is varied from 0.01 to 5% w/w in a 45% quantum yield. In Figure 5.2, the yellow area of optical efficiency corresponds to the green curve in Figure 5.3.

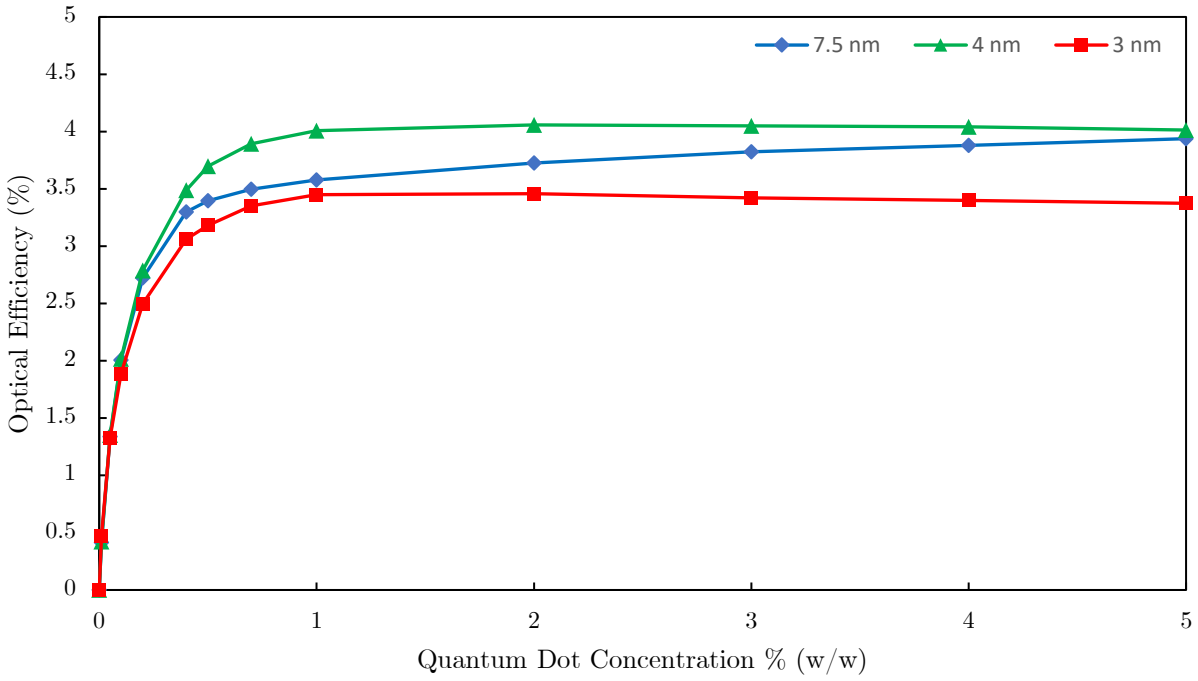

Figure 5.3: Optical efficiency with the variation of QD concentration and QD sizes.

Figure 5.3 shows that the optical efficiency initially increases when the number of QD increases in the LSC. Then the optical efficiency slightly decreases after a certain QD concentration. The absorption of photons increases initially with the QD concentration in the LSC. The highest optical efficiency is obtained when the incident photons equal the number of QDS in the LSC. Then reabsorption and scattering effects of the QDs become dominant when the QD concentration increases in the LSC. With this, the optical efficiency decreases. In all sizes of QDs, the maximum optical efficiency is found to be in the concentration range between 0.4 to 5% w/w.

The maximum optical efficiency of 3.46% is obtained at the edges of the LSC in a 3 nm QD size of a 2% w/w QD concentration. 3 nm size QDs have a lower optical efficiency than other QDs due to smaller Stokes' shift in the absorption and emission spectra (see Figure 3.9), which results in a

self-absorption loss. The maximum optical efficiency of 4.06% in 2% w/w QD concentration and 3.94% in 5% w/w QD concentration is obtained for 4 nm and 7.5 nm size QDs, respectively.

5.1.2. Quantum Yield

In this simulation test, the optical efficiency is recorded for three different quantum yield values of 45%, 60%, and 100%. These are tested on the standard values of LSC parameters. The simulation results of optical efficiency are recorded in Figure 5.4. As expected, the maximum optical efficiency is achieved when the QDs have the highest PLQY of 100%. The 100% quantum yield, also describes as unity, represents an ideal case where in most cases, it is far from reality for luminescent particles to achieve a higher quantum yield. For the 100% quantum yield case, the maximum optical efficiency of 8.91% is obtained at 2% w/w QD concentration. With lower quantum yield at the same concentration, the emitted photons per photons absorbed from QDs are less, which results in lower optical efficiency. With a PLQY of 60%, the maximum optical efficiency is about 5.39%, and for the lowest PLQY of 45%, the maximum optical efficiency is 4.06%.

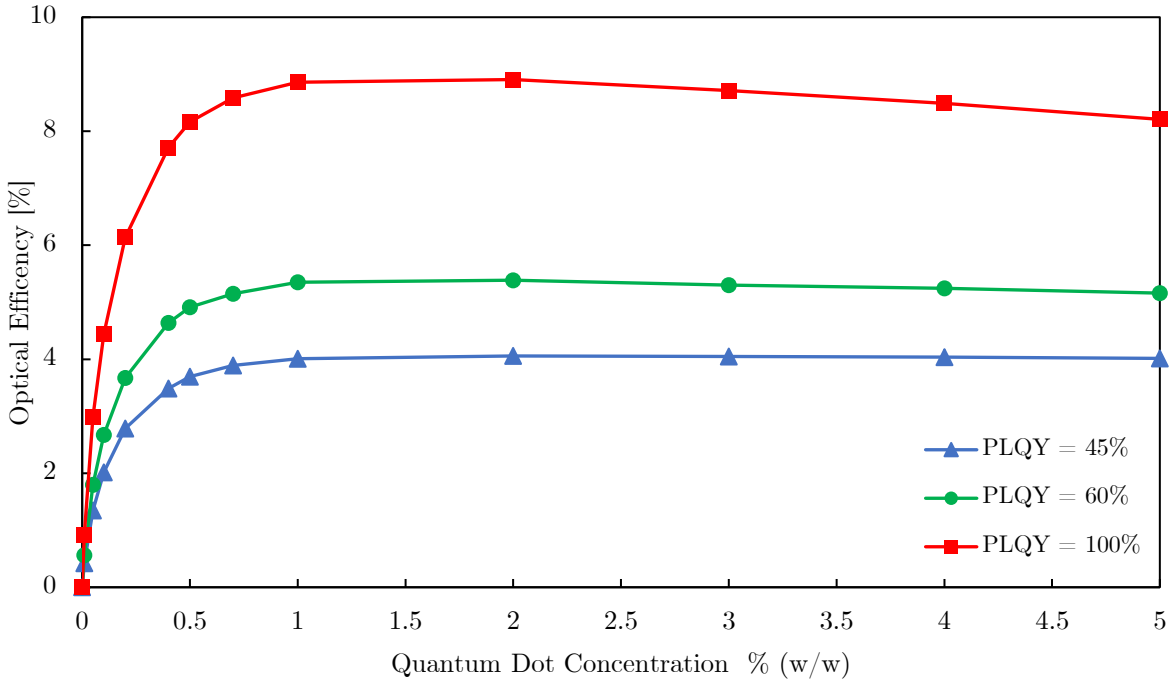

Figure 5.4: Optical efficiency with the variation of QD concentration

For the standard quantum dot concentration of 0.5% w/w, it is observed that around 3.70% optical efficiency in the PV edges is achieved when the quantum yield is 45%. A 4.92% optical efficiency is achieved when the quantum yield is 60%. Finally, 8.16% optical efficiency is achieved when the quantum yield is 100%. In Figure 5.5, optical efficiency and losses are plotted using a quantum yield of 100% in an LSC model with standard parameters. The yellow area of the optical efficiency corresponds to the red curve in Figure 5.4. In the figure, it is possible to see the change of losses at a high quantum efficiency of Si-QD particles. Optical efficiency, reflection (green area), and transmission (blue area) losses are higher in the 100% quantum yield. However, thermalization losses (orange area) show a lower loss compared to QDs, with an PLQY of 45%.

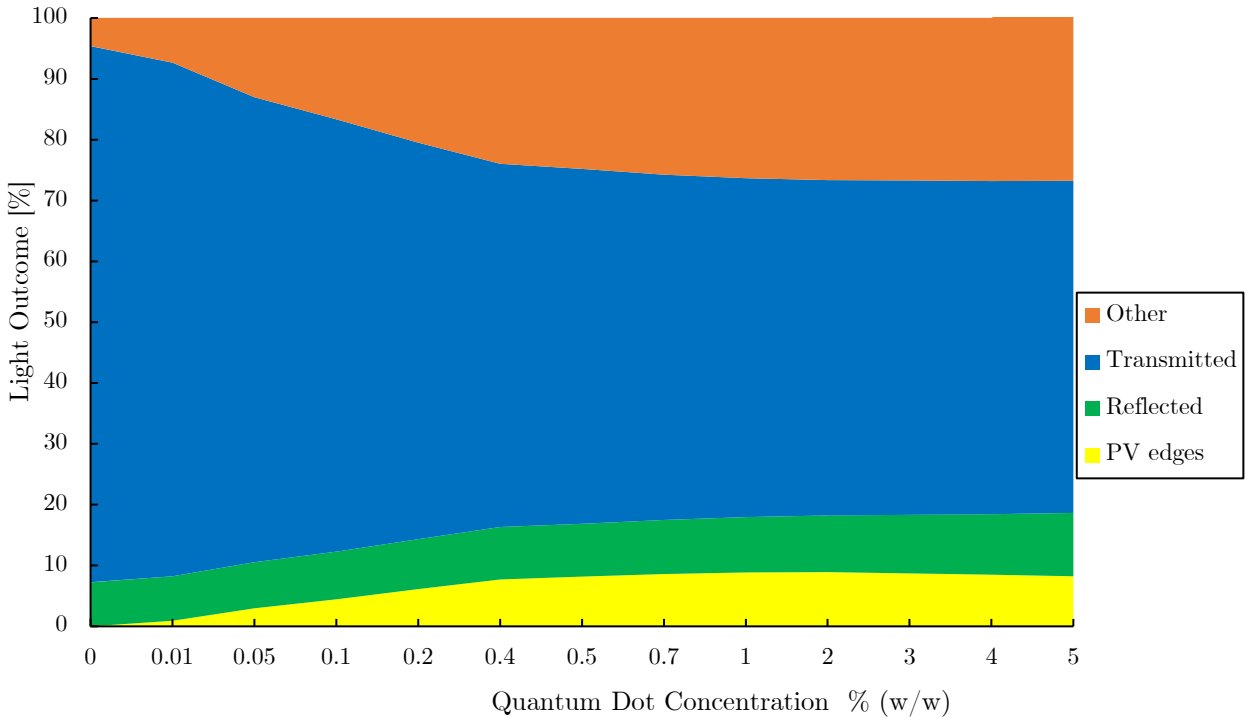

Figure 5.5: Optical efficiency and losses with a QD quantum yield of 100%

Performance of the Si-QD LSC design is obtained by varying glass thickness (1 – 10 mm), copolymer thickness (0.1 – 1 mm), and LSC sizes (12 - 100 cm). In these cases, the Si-QD quantum yield is modeled as 45% efficiency.

5.1.3. Glass thickness

In the following simulation results, the copolymer film thickness of 0.1 mm is kept constant, and the glass thickness is changed from 1 mm to 10 mm. The main objective of these simulations is to see the optical efficiency change from a thinner to a thicker waveguide in the LSC model. The optical efficiency due to this change is plotted and shown in Figure 5.6.

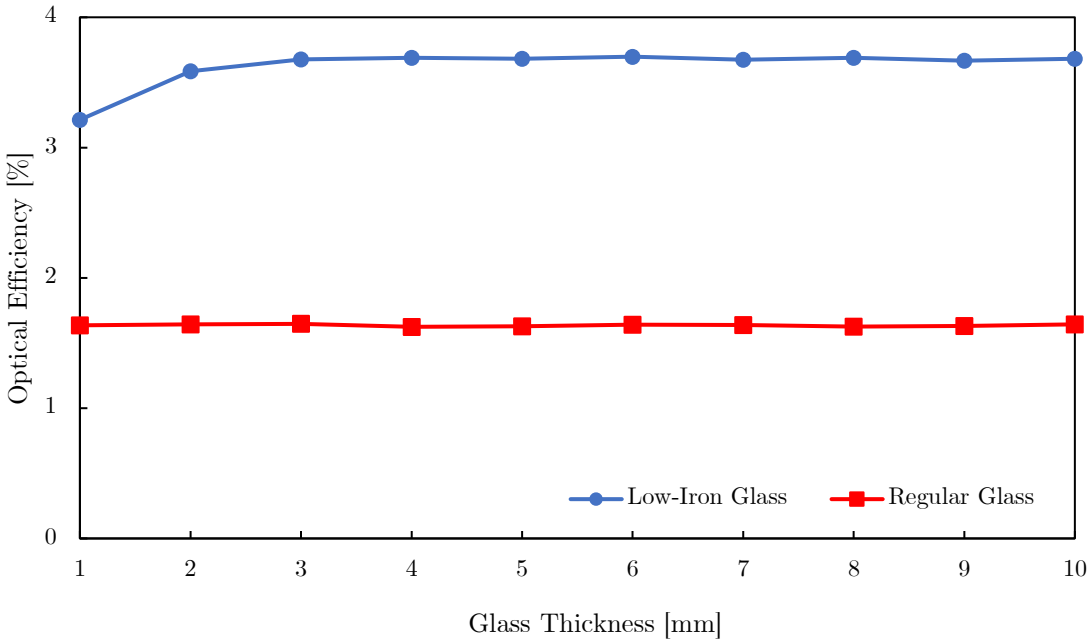

Figure 5.6: Optical efficiency change with different glass thickness.

According to the simulation results, the optical efficiency from the edges in the LSC slightly increased when the glass thickness increased. This increment is shown in Figure 5.6 for both low-iron and regular glass waveguides.

Regular glass receives a lower optical efficiency than low-iron glass, as regular glass has higher absorption than low-iron glass (see Figure 3.6). A constant optical efficiency of 1.64% is obtained throughout the regular glass thickness. For low-iron glass, the optical efficiency initially increases from 3.21% to 3.68% and is constant throughout the remaining thickness in the LSC simulations.

5.1.4. Copolymer thickness

In this simulation test, the model is changed by increasing the thickness of the copolymer film to obtain optical efficiency. First, the glass thickness of 6 mm is kept constant, and the copolymer film thickness is changed from 0.1 mm to 1 mm. The optical efficiency from the edges is shown in Figure 5.7.

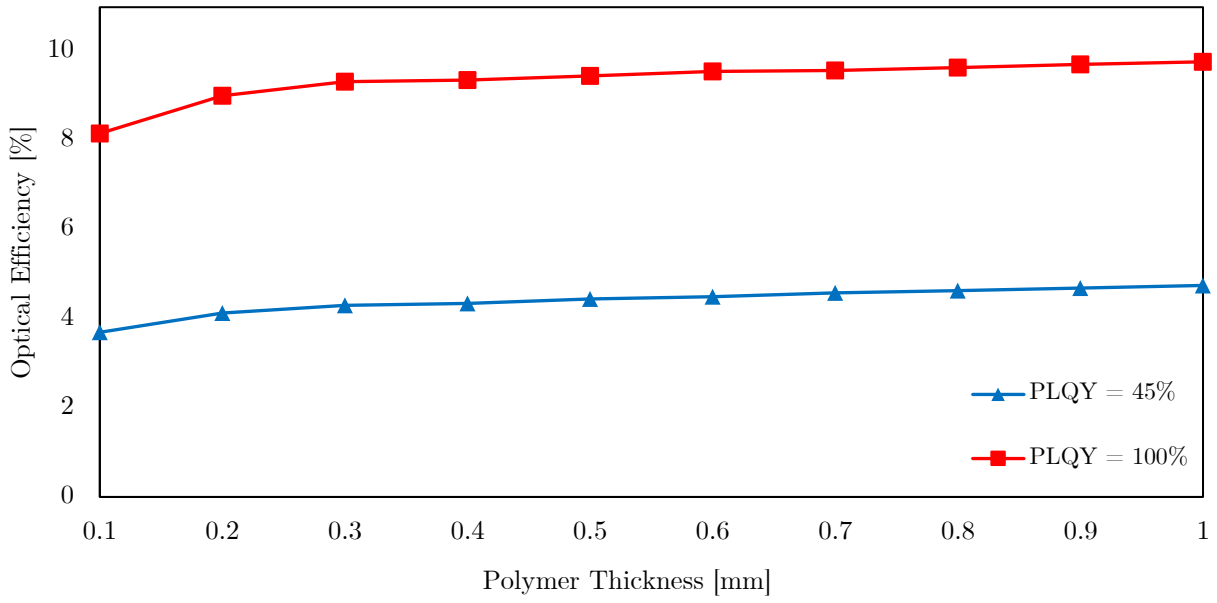

Figure 5.7: Optical efficiency change with different copolymer thickness.

The results show that the total number of quantum dots in the copolymer film increases when copolymer thickness is increased. More incident photons are absorbed by the QD, which increases optical efficiency. This figure presents the ideal case where Si-QD PLQY equals 100%.

These models show that optical efficiency slightly increases with the thickness of the copolymer film. The estimated trends with the 6 mm glass thickness of 15 x 15 cm^2 area model receive an optical efficiency variation from 3.70% to 4.75% of the copolymer thickness from 0.1 mm to 1 mm. The optical efficiency varies from 8.16% to 9.77% when the PLQY equals 100%.

5.1.5. LSC area

This analysis continues with changing the surface area while keeping the same standard parameters of the LSC model. The surface areas are changed by: 144 cm^2 (L = 12 cm, H = 12 cm), 225 cm^2 (L = 15 cm, H = 15 cm), 400 cm^2 (L = 20 cm, H = 20 cm), 900 cm^2 (L = 30 cm, H = 30 cm), 3600 cm^2 (L = 60 cm, H = 60 cm), and 1 m^2 (L = 100 cm, H = 100 cm). AM1.5 global solar spectrum, with an integrated power density of 1000 W/m^2, is used to illuminate the front surface of these LSC devices. A power of 14.4 W, 22.5 W, 40 W, 90 W, 360 W, and 1000 W are used, respectively, as the input power of the solar light for the different size LSC devices. These are simulated using the 4 nm QD properties, such as absorption and emission spectra, with a 45% quantum yield. Figure 5.8 demonstrates the simulation results of the optical efficiency with different LSC sizes.

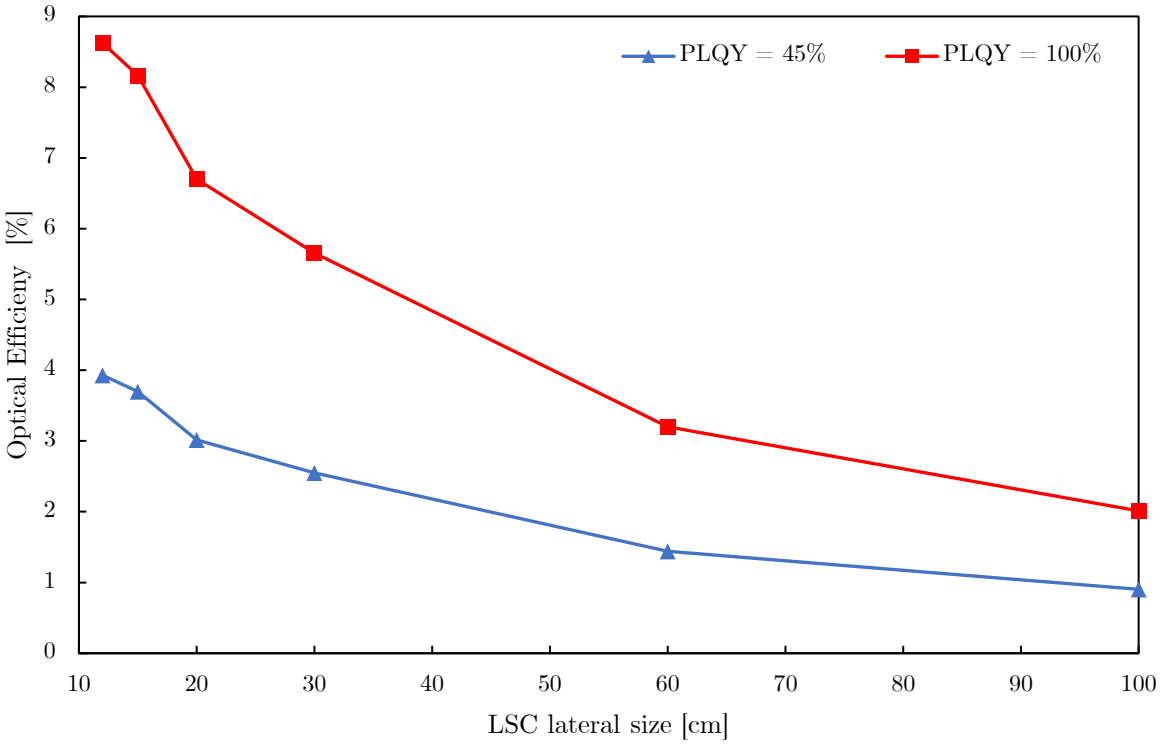

Figure 5.8: Variation of optical efficiency with different length of LSCs.

It is observed that the optical efficiency decreases with increasing LSC lengths. This is expected as re-absorption and scattering losses occur when re-emitted photons propagate throughout the

edges of the waveguide in the LSC. Thus, selecting an optimal LSC length for the LSC is essential. As shown in Figure 5.8, the optical efficiency of 3.93% is obtained by a smaller LSC area (144 cm^2), and the optical efficiency of 0.90% is obtained at a larger LSC area (1 m^2). With a PLQY of 100%, the optical efficiency of 8.63% is obtained by a 144 cm^2 LSC area, and the optical efficiency of 2.01% is obtained when the LSC area is increased to 1 m^2.

Once the LSC size is increased, the optical efficiency decreases accordingly. In smaller LSC areas, photons travel shorter distances resulting in a higher probability that light will reach the edges of the LSC. In larger areas, photons travel longer distances that are likely to be reabsorbed and scattered before reaching the edges of the LSC, resulting in lower optical efficiency.

5.1.6. Reflective surface

The least expensive and simplest method to improve optical efficiency is through using reflective surface at the back of the LSC. The existing Si-QD LSC model is modified by adding a reflective surface to the bottom of the LSC model, as shown in Figure 5.9, to acquire optical efficiency. This reflective surface was changed starting from 0% to 100% reflectiveness at increments of 10%.

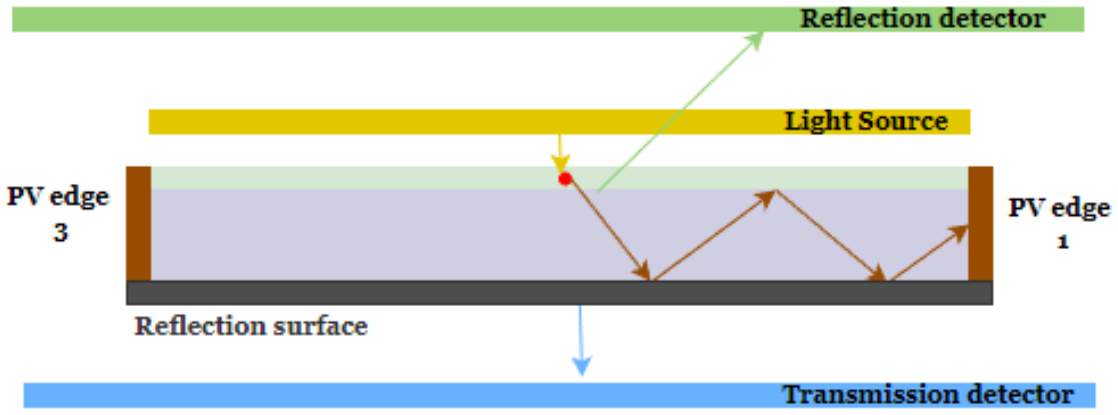

Figure 5.9: Schematic diagram of an LSC model when a reflective surface is attached in the bottom.

According to Figure 5.10, the optical efficiency slightly increased when the reflective surface in the model increased. Due to the reflective surface, the LSC model's light trapping has increased, resulting in a higher optical efficiency when the reflective surface is 100%. In a PLQY of 45%, the

optical efficiency of 3.67% is obtained with no reflectivity. With a reflectivity of 100%, the optical efficiency increased to 4.05%. In an ideal case of PLQY of 100%, the optical efficiency is increased from 8.09% to 8.98%.

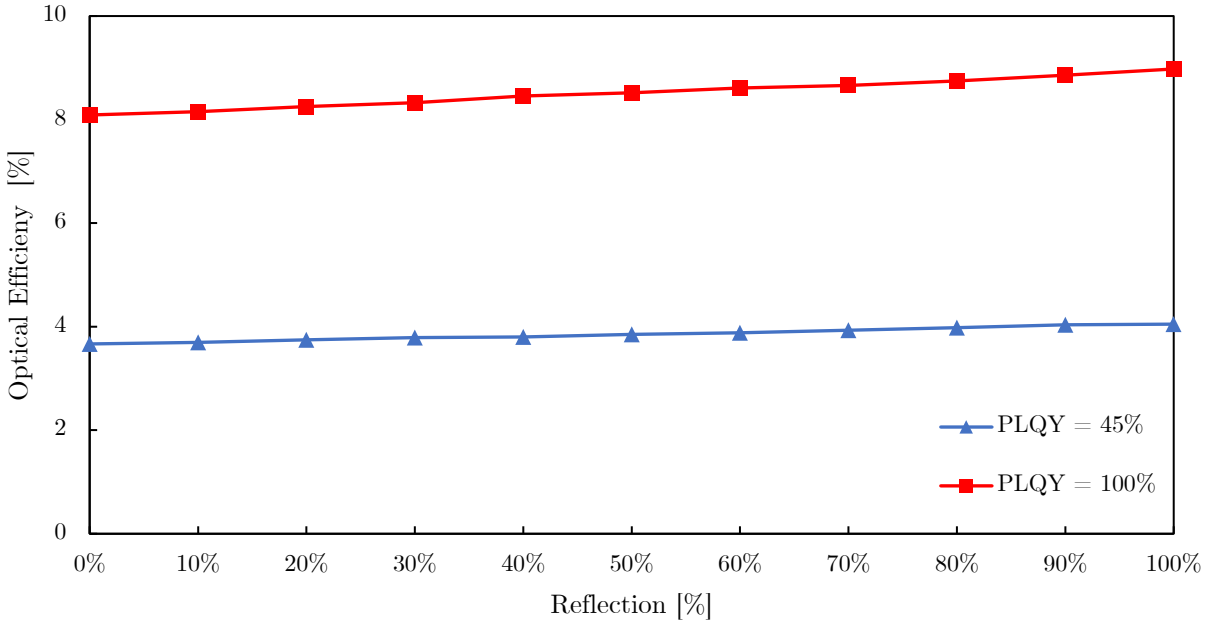

Figure 5.10: Optical efficiency change with different reflective surfaces.

5.1.7. Testing different light source

A final simulation test is conducted on the initial Si-QD LSC setup with standard LSC parameters. Two different light sources are tested for the last simulations. First, a monochromatic light source is illuminated in the front area of the LSC (copolymer film) to record the optical efficiency and losses. Then, sunlight (AM1.5) in the range of 310-1500 nm is used as the main light source to illuminate the front LSC surface area. Table 5.2 shows the simulation results of the two different light sources completely illuminated to the LSC surface area.

Table 5.2: Simulation results of a Si-QD LSC model when illuminated by two different light sources.

	Monochromatic light at 365 nm	**Solar Spectrum AM1.5**
Optical Efficiency	7.65%	3.70%
Reflected	6.58%	7.11%
Transmitted	2.48%	56.7%
Other Losses	83.3%	35.4%

The above table shows that when using monochromatic light at 365 nm, optical efficiency is around 7.67% and 2.48% of transmitted light, where 83.3% of heat and thermalization loss occurs. The solar light AM1.5 results in a lower optical efficiency compared to the monochromatic light. This optical efficiency is around 3.70% and has a higher transmitted light of 56.7% compared to the previous light source.

Si-QDs can absorb only up to 510 nm of the solar spectrum, where all the spectrum is not utilized, and every spectrum wavelength does not have the same irradiance intensity (see Figure 3.13). Due to this, the solar spectrum light source gives lower optical efficiency compared to the monochromatic light source.

5.2. Discussion of results

LSCs with Si-QD particles embedded in a copolymer film and a glass waveguide are simulated using standard parameters in Table 5.1. From the simulation of the Si-QD LSC model, it is observed a higher optical efficiency is achievable with ideal characteristics, such as 100% quantum yield, larger QD concentration, and small LSC size. To measure the optical efficiency, ideal optical properties are considered: 100% absorption in the PV edges and no impurities in the glass and PMMA. In a realistic model, the PV edge will not absorb all the light since PV cells have reflective losses. Impurity effects cause absorption and scattering losses where the effects are not studied in these models.

Results of QD concentration and QD sizes: Optical efficiency initially increases when the QD concentration increases. The highest optical efficiency is obtained when the incident photons equal the QD concentration. Then the re-absorption and scattering effects become dominant, and the optical efficiency decreases. Light can easily transmit through the LSC at lower QD concentrations without interacting with Si-QD particles. A large QD concentration in 4nm QDs is expected as there is no re-absorption by QD particles. Si-QD spectra have no overlap between absorption and emission, which will result in no self-absorption losses. So, emitted photons propagate longer distances. However, photons can be scattered by other non-absorbed QD particles when they encounter them. 3 nm QDs have a lower optical efficiency than other QDs (4 nm and 7.5 nm), as there is an overlap in the absorption and emission spectra (see Figure 3.9), resulting in re-absorption losses.

Results of Quantum yield: For higher quantum efficiency QDs, a higher optical efficiency was possible for the LSC performance. For a QY of 60%, the optical efficiency increased by 1% compared to the standard parameter LSC model. In an ideal case, where QY is 100%, the optical efficiency increased by 4% compared to 45% efficiency QDs in the standard LSC model.

Results of glass and copolymer thickness: When the glass thickness is increased in the LSC model, a slight increase in the start and then a constant optical efficiency is achieved. When the copolymer thickness is increased from 0.1 mm to 1 mm, the optical efficiency increases by 0.4% when PLQY is 45%. When the PLQY is 100%, the optical efficiency increases by 1%.

Results of LSC size: The model predicts optical efficiency reduction when the LSC area increases to 1 m^2. This is expected as the re-absorption and scattering loss mechanism increases, and the average path length to the edge of the LSC also increases. In a QD concentration of 0.5% w/w, the smaller LSC model of 144 cm^2 achieves an optical efficiency of 3.93%. A larger area (1 m^2) of the same characteristics in the LSC model provides an optical efficiency of 0.90%, where light must travel a longer distance to the PV edges, which leads to re-absorption and scattering losses.

Results of reflective surface: Light is carried mainly by total internal reflection in the glass waveguide. A reflective surface is used under the glass waveguide to increase the optical efficiency.

A slight increase in optical efficiency is achieved when a higher reflectivity surface is attached to the bottom of the LSC surface.

Chapter 6

Conclusion and Future work

The main aim of the thesis work is to investigate a luminescent solar concentrator and how the parameters of an LSC affect its performance. In this project, two different luminescent particles, red-dye and silicon quantum dot-based LSC, were studied using ANSYS SPEOS. The first LSC model is a PMMA doped with red-dye particles. The second LSC model has two layers: The top layer is a thin copolymer known as Poly (butyl methacrylate-co-methyl methacrylate) where silicon quantum dots are embedded in the film and the second layer of the LSC is a glass where the light is waveguided to the edges.

The simulation results show that ANSYS SPEOS is a useful tool for ray-tracing an LSC-based model. The simulation results of a red dye-based LSC have similar efficiency results from experimental measurements conducted by a previous thesis work [28]. The red-dye particles in the LSC are characterized by their absorption, emission spectra, and quantum yield. Ray-tracing was used to evaluate the optical efficiency and losses. The simulation results showed similar results to the experimental measurements. The optical efficiency of the model is 3.7%, and that of the

experimental measurement was 4.5%, which has a 0.8% error. Losses in the model showed similar results. The total transmitted light of the model was 25.4%, and the experimental transmitted measurement was 30.8%. With this red-dye validation model, it was extended to the silicon quantum dot-based LSC model.

The optical efficiency is recorded from the simulation results in the silicon quantum dot LSC model. The LSC model with a glass thickness of 6 mm and copolymer thickness of 0.1 mm is simulated, and an optical efficiency of 3.70% was received at a QY of 45%. LSC parameters of quantum dot concentration, quantum yield, glass thickness, and copolymer film thickness were changed, and the optical efficiency was recorded in different cases. Increasing QD concentration does not increase the optical efficiency indefinitely, but it plateaus at the maximum optical efficiency (See Figure 5.4). In a PLQY of 45% and 60%, the graph plateaus at 4.06% and 5.39%, respectively. When the glass thickness was increased, the optical efficiency was constant in the low-iron and regular glass with an optical efficiency of 3.70% and 1.64%, respectively. The model was then changed by adding a reflective surface to the bottom of the LSC. When a 100% reflective surface was added to the bottom surface, the optical efficiency increased to 4.05%. Finally, a larger LSC size (1 m^2) was determined to have a lower optical efficiency of 0.90%, while a smaller LSC size (144 cm^2) led to a higher optical efficiency of 3.93% in a PLQY of 45%.

The discussed results and conclusion can answer the main questions proposed in this thesis. The main parameters that affect the LSC performance are determined. Thus, it was determined how it can be optimized. One of the main parameters affecting optical efficiency and transmission losses is the QD concentration. With higher concentration, more light can be converted by QDs, but high concentration also means that other QDs can scatter emitted photons. With lower concentrations, light can reach the PV edges easily, but light can also easily transmit through the waveguide without being absorbed by luminescent particles. Another main parameter is the quantum yield. A higher quantum yield will result in a lower thermalization loss and higher optical efficiency.

In LSC window application, not only the optical efficiency, but the transparency of the glass window is important. Small-size LSCs present a higher optical efficiency, but large-size LSCs present lower optical efficiency. In higher LSC model, light propagation is difficult as the path

length is increased to reach the PV edge in the LSC. The device presents poor results in performance. The optical efficiency was under 1% for the large-scale LSC model. For the optimum performance of a thin-film LSC window application, a higher photoluminescence quantum yield is recommended, where more emitted photons can propagate in the waveguide.

6.1. Future Developments

Currently, the company working on the silicon quantum dots has provided the required measured characteristics, which are used in the simulation. AQM has provided additional silicon quantum dot measured characteristics, such as absorption and emission spectra, quantum yield, reflective index, and absorption variation of glass and copolymer. To improve the silicon quantum dot-based model, one of the main recommendations is to make a small-size silicon quantum dot LSC model to obtain experimental data by comparing them with the ray-tracing model. As discussed in Chapter 4, a red-dye-based LSC model is simulated in the ray-tracing software. The results were compared to the real sample to understand the optical efficiency and losses better. The same procedure can be used for the silicon quantum dot LSC model to obtain a better understanding of the device.

Reference

[1] G. B. Smith, Green nanotechnology: Solutions for Sustainability and Energy in the Built Environment, CRC Press, 2010.

[2] G. Kocher-Oberlehner, M. Bardosova, M. Pemble and B. S. Richards, "Planar photonic solar concentrators for building-integrated photovoltaics," *Solar Energy Materials and Solar Cells,* vol. 104, pp. 53-57, 2012.

[3] J. W. E. Wiegman and E. van der Kolk, "Building integrated thin film luminescent solar concentrators: Detailed efficiency characterization and light transport modelling," *Solar Energy Materials and Solar Cells,* vol. 103, pp. 41-47, 2012.

[4] R. Reisfeld, D. Shamrakov and C. Jorgensen, "Photostable solar concentrators based on fluorescent glass films," *Solar Energy Materials and Solar Cells,* vol. 33, no. 4, pp. 417-427, 1994.

[5] S. M. El-Bashir, F. M. Barakat and M. S. AlSalhi, "Metal-enhanced fluorescence of mixed coumarin dyes by silver and gold nanoparticles: Towards plasmonic thin-film luminescent solar concentrator," *Journal of Luminescence,* vol. 143, pp. 43-49, 2013.

[6] J. Chow, R. J. Kopp and P. Portney, "Energy Resources and Global Development," *Science,* vol. 302, no. 5650, pp. 1528-1531, 2003.

[7] National Resources Canada, "Energy Fact Book 2021-2022," National Energy Board.

[8] Energy Information Administration, "International Energy Outlook 2019," 2019.

[9] Cambridge University Press, Global Energy Assessment: Toward a Sustainable Future, ISBN: 9780511793677, 2012.

[10] "U.S Energy Information Administration," 2019. [Online]. Available: https://www.eia.gov/todayinenergy/detail.php?id=41493#.

[11] C. Wadia, A. P. Alivisatos and D. M. Kammen, "Materials Availability Expands the Opportunity for Large-Scale Photovoltaics Deployment," *Environmental Science & Technology,* vol. 43, no. 6, pp. 2072-2077, 2009.

[12] "Lazard's Levelized Cost of Energy Analysis," Lazard, 2020.

[13] "April 25, 1954: Bell Labs Demonstrates the First Practical Silicon Solar Cell," APS News, 04 2009. [Online]. Available: https://www.aps.org/publications/apsnews/200904/physicshistory.cfm#:~:text=In%201883%2C%20American%20inventor%20Charles,and%20thus%20not%20very%20practical.. [Accessed 26 06 2022].

[14] International Energy Agency, "Snapshot of Global PV Markets," 2022. [Online]. Available: https://iea-pvps.org/snapshot-reports/snapshot-2022/.

[15] R. F. Service, "Skyscrapers could soon generate their own power, thanks to see-through solar cells," Science, 28 06 2018. [Online]. Available: https://www.science.org/content/article/skyscrapers-could-soon-generate-their-own-power-thanks-see-through-solar-cells. [Accessed 26 06 2022].

[16] F. Meinardi, F. Bruni and S. Brovelli, "Luminescent solar concentrators for building-integrated photovoltaics," *Nature Reviews Materials,* 2017.

[17] "Edmond Becquerel," Physics Today, 24 03 2016. [Online]. Available: https://physicstoday.scitation.org/do/10.1063/pt.5.031182/full/. [Accessed 26 06 2022].

[18] K. Kumar, "A History of the Solar Cell, in Patents," 27 04 2020.

[19] Smithsonian Magazine, "A Brief History of Solar Panels," [Online]. Available: https://www.smithsonianmag.com/sponsored/brief-history-solar-panels-180972006/.

[20] V. Siva Reddya, S. C. Kaushik, K. R. Ranjan and S. K. Tyagi, "State-of-the-art of solar thermal power plants-A review," *Renewable and Sustainable Energy Reviews,* vol. 27, pp. 258-273, 2013.

[21] A. Goetzberger and W. Greubel , "Solar Energy Conversion with Fluorescent Collectors," *Applied Physics,* vol. 14, pp. 123-139, 1977.

[22] F. I. Chowdhury, C. Dick, L. Meng, S. M. Mahpeykar, B. Ahvazib and X. Wang, "Cellulose nanocrystals as host matrix and waveguide materials for recyclable luminescent solar concentrators," *RSC Advances,* no. 51, 2017.

[23] Jun Zhang, Mengjiao Wang, Yi Zhang, Hao He, Wei Xie, Mengmeng Yang , Jianjun Ding, Jun Bao, Song Sun, Chen Gao, "Optimization of large-size glass laminated luminescent solar concentrators," *Solar Energy,* 2015.

[24] P. P. C. Verbunt and M. G. Debije, "Progress in Luminescent Solar Concentrator Research: Solar Energy for the Built Environment," *World Renewable Energy Congress,* pp. 2751-2759, 2011.

[25] Y. K. Gun'ko and F. Purcell-Milton, "Quantum dots for Luminescent Solar Concentrators," *Journal of Material Chemistry,* no. 33, 2012.

[26] F. Meinardi, S. Ehrenberg, L. Dhamo, F. Carulli, M. Mauri, F. Bruni, R. Simonutti, U. Kortshagen and S. Brovelli, "Highly efficient luminescent solar concentrators based on earth-Abundant indirect-bandgap silicon quantum dots," *Nature Photonics,* vol. 11, no. 3, pp. 177-185, 2017.

[27] O'Farrell, N., Houlton, A. & Horrocks, B. R., "Silicon nanoparticles: applications in cell biology and medicine," *Int. J. Nanomedicine,* vol. 1, p. 451–472, 2006.

[28] L. M. Chávez, "Optimization of a Luminescent Solar Concentrator: Simulation and application in PowerWindow design," TU Delft Applied Sciences, 2017.

[29] J. R. Meyer-Arendt, Introduction to Classical and Modern Optics, 4th edition, Prentice Hall, 1995.

[30] PVEducation, "Absorption Coefficient," [Online]. Available: https://www.pveducation.org/pvcdrom/pn-junctions/absorption-coefficient.

[31] Edinburgh Instruments, "Fluorescence, Phosphorescence, Photoluminescence Differences," [Online]. Available: https://www.edinst.com/blog/photoluminescence-differences/.

[32] Bio-Rad, "Fluorescence," 2017. [Online]. Available: https://www.bio-rad-antibodies.com/flow-cytometry-fluorescence.html.

[33] Thermo Fisher Scientific, "Fluorescence Fundamentals," [Online]. Available: https://www.thermofisher.com/ca/en/home/references/molecular-probes-the-handbook/introduction-to-fluorescence-techniques.html.

[34] Edinburgh Instruments, "What is Quantum Yield," [Online]. Available: https://www.edinst.com/blog/what-is-quantum-yield/. [Accessed 18 8 2022].

[35] M. Gajic, "Non-imaging technologies for designing a hybrid photovoltaic and solar thermal collector," RMIT university, 2017.

[36] Y. Zhou, H. Zhao, D. Ma and F. Rosei, "Harnessing the properties of colloidal quantum dots in luminescent solar concentrators," *Chemical Society Reviews,* no. 15, 2018.

[37] W. E. Benjamin, D. R. Veit, M. J. Perkins, E. Bain, K. Scharnhorst, S. McDowall, D. L. Patrick and J. D. Gilbertson, "Sterically Engineered Perylene Dyes for High Efficiency Oriented Fluorophore Luminescent Solar Concentrators," *Chemistry of materials,* vol. 26, pp. 1291-1293, 2014.

[38] J. S. Batchelder, A. H. Zewail and T. Cole, "Luminescent solar concentrators. 2: Experimental and theoretical analysis of their possible efficiencies," *Applied Optics,* vol. 20, no. 21, pp. 3733-3754, 1981.

[39] T. Daniel, C. Bauer, I. Dolamic and D. Brühwiler, "Spectral-based analysis of thin film luminescent solar concentrators," *Solar Energy,* vol. 84, no. 8, pp. 1366-1369, 2010.

[40] H. Liang, Z. Zheng, Z. Li, J. Xu, B. Chen, H. Zhao, Q. Zhang and H. Ming, "Fabrication and amplification of Rhodamine B-doped step-index polymer optical fiber," *Journal of Applied Polymer Science,* vol. 93, no. 2, pp. 681-685, 2004.

[41] F. Meinardi, A. Colombo, K. A. Velizhanin, R. Simonutti, M. Lorenzon, L. Beverina, R. Viswanatha, V. I. Klimov and S. Brovelli, "Large-area luminescent solar concentrators based on 'Stokes-shift-engineered' nanocrystals in a mass-polymerized PMMA matrix," *Nature Photonics,* vol. 8, pp. 392-399, 2014.

[42] Y. F. Zhou, D. Benetti, Z. Y. Fan, H. G. Zhao, D. L. Ma, A. O. Govorov, A. Vomiero and F. Rosei, "Near Infrared, Highly Efficient Luminescent Solar Concentrators," *Advanced Energy Materials,* vol. 6, no. 11, 2016.

[43] W. G. J. H. M. V. Sark, K. W. J. Barnham, L. H. Slooff, A. J. Chatten, A. B¨uchtemann, A. Meyer, S. J. Mccormack, R. Koole, D. J. Farrell, R. Bose, E. E. Bende, A. R. Burgers, T. Budel, J. Quilitz, M. Kennedy, T. Meyer, C. D. M. Doneg´a, A. Meijerink and D. Vanmaekelbergh, "Luminescent Solar Concentrators – A review of recent results," *Optic Express,* vol. 16, no. 26, pp. 21773-21792, 2008.

[44] S. Kanchi and D. Sharma, Nanomaterials in Diagnostic Tools and Devices, ISBN: 9780128179246, 2020.

[45] U. Resch-Genger, M. Grabolle, S. Cavaliere-Jaricot, R. Nitschke and T. Nann, "Quantum dots versus organic dyes as fluorescent labels," *Nature Methods,* vol. 5, no. 9, pp. 763-776, 2008.

[46] O. I. Micic, C. J. Curtis, K. M. Jones, J. R. Sprague and A. J. Nozik, "Synthesis and Characterization of InP Quantum Dots.," *The Journal of Physical Chemistry,* vol. 98, no. 19, pp. 4966-4969, 1994.

[47] A. G. Cullis, L. T. Canham and P. D. J. Calcott, "The structural and luminescence properties of porous silicon," *Journal of Applied Physics,* vol. 82, no. 3, pp. 909-965, 1997.

[48] S. Ehrenberg, "Silicon quantum dot luminescent solar concentrators," 2019.

[49] D. Kovalev, H. Heckler, M. Ben-Chorin, G. Polisski, M. Schwartzkopff and F. Koch, "Breakdown of the k-Conservation Rule in Si Nanocrystals," *Physical Review Letters,* vol. 81, pp. 2803-2806, 1998.

[50] I. Coropceanu and M. G. Bawendu, "Core/Shell Quantum Dot Based Luminescent Solar Concentrators with Reduced Reabsorption and Enhanced Efficiency," *Nano Letters,* vol. 14, no. 7, pp. 4097-4101, 2014.

[51] F. Meinardi, H. McDaniel, C. Francesco, A. Colombo, K. A. Velizhanin, N. S. Makarov, R. Simonutti, V. I. Klimov and S. Brobelli, "Highly efficient large-area colourless luminescent solar concentrators using heavy-metal-free colloidal quantum dots," *Nature Nanotechnology,* vol. 10, pp. 878-885, 2015.

[52] Y. Zhou, D. Benetti, Z. Fan, H. Zhao, D. Ma, A. O. Govorov, A. Vomiero and F. Rosei, "Near Infrared, Highly Efficient Luminescent Solar Concentrator," *Advanced Energy Materials,* vol. 6, no. 11, 2016.

[53] D. K. G. de Boer, D. J. Broer, M. G. Debije, W. Keur, A. Meijerink, C. R. Ronda and P. P. C. Verbunt, "Progress in phosphors and filters for luminescent solar concentrators," *Optical Express,* vol. 20, no. S3, pp. A395-A405, 2012.

[54] S.-P. Ying, B.-M. Chen and W.-L. Tseng, "Thin-Film Luminescent Solar Concentrators Using Inorganic Phosphors," *IEEE Transactions on Electron Devices,* vol. 66, no. 5, pp. 2290-2294, 2019.

[55] B. Zhang, P. Zhao, L. Wilson, J. Subbiah, H. Yang, P. Mulvaney, D. J. Jones, K. P. Ghiggino and W. W. H. Wong, "High-Performance Large-Area Luminescence Solar

Concentrator Incorporating a Donor–Emitter Fluorophore System," *ACS Energy Letters,* vol. 4, no. 8, pp. 1839-1844, 2019.

[56] G. Griffini, M. Levi and S. Turri, "Thin-film luminescent solar concentrators: A device study towards rational design," *Renewable Energy,* vol. 78, pp. 288-294, 2015.

[57] M. K. Assadi, H. Hanaei, N. M. Mohamed, R. Saidur, S. Bakhoda, R. Bashiri and M. Moayedfar, "Enhancing the efficiency of luminescent solar concentrator (LSC)," *Applied Physics,* vol. 122, no. 821, 2016.

[58] K. Busch, C. M. Soukoulis, and E. N. Economou, "Transport and scattering mean free paths of classical waves," 1994.

[59] J. W. Wiegman, "Detailed efficiency characterisation of Lu2O3:Eu3+ thin film luminescent solar concentrators: an analytic and experimental light transport study.," 2012.

[60] R. Reisfeld, D. Shamrakov and C. Jorgensen, "Photostable solar concentrators based on fluorescent glass films," *Solar Energy Materials and Solar Cells,* vol. 33, no. 4, pp. 417-427, 1994.

[61] T. Dienel, C. Bauer, I. Dolamic and D. Bruhwiler, "Spectral-based analysis of thin film luminescent solar concentrators," *Solar Energy,* vol. 84, no. 4, pp. 1366-1369, 2010.

[62] D. Sahin, B. Ilan and D. F. Kelly, "Monte-Carlo simulations of light propagation in luminescent solar concentrators based on semiconductor nanoparticles," *Journal of Applied Physics,* vol. 110, no. 3, 2011.

[63] P. Moraitis, G. van Leeuwen and W. van Sark, "Visual Appearance of Nanocrystal-Based Luminescent Solar Concentrators," *Materials,* vol. 12, no. 6, p. 885, 2019.

[64] A. R. Burgers, L. H. Slooff, R. Kinderman and J. A. M. Van Roosmalen, "Modelling of luminescent concentrators by ray-tracing," *Proceedings of the 20th European Photovoltaic Solar Energy Conference,* pp. 394-397, 2005.

[65] J. Shu, X. Zhang, P. Wang, R. Chen, H. Zhang, D. Li, P. Zhang and J. Xu, "Monte-Carlo simulations of optical efficiency in luminescent solar concentrators based on all-inorganic perovskite quantum dots," *Physica B: Condensed Matter,* vol. 548, pp. 53-57, 2018.

[66] W. A. Al-Taa'y, S. F. Oboudi, E. Yousif, M. A. Nabi, R. M. Yusop and D. Derawi, "Fabrication and Characterization of Nickel Chloride Doped PMMA Films," *Advanced in Material Science and Engineering,* 2015.

[67] Graz University of Technology, "Lumogen Red F300," 2017.

[68] B. C. Rowan, L. R. Wilson and B. S. Richards, "Advanced Material Concepts for Luminescent Solar Concentrators," *IEEE Journal of Selected Topics in Quantum Electronics,* vol. 14, no. 5, pp. 1312-1322, 2008.

[69] "Applied Quantum Materials Inc.," [Online]. Available: https://www.aqmaterials.com/.

[70] D. W. Ball and J. A. Key, Introductory Chemistry – 1st Canadian Edition, Victoria: BCcampus, 2014.

[71] "Reference Air Mass 1.5 Spectra," [Online]. Available: https://www.nrel.gov/grid/solar-resource/spectra-am1.5.html.

[72] S. V. Overbeek, "Optical Efficiency Measurements on Luminescent Solar Concentrators," Applied physics Bachelor Thesis, 2015.

[73] M. G. Debije, P. P. C. Verbunt, B. C. Rowan, B. S. Richards and T. L. Hoeks, "Measured surface loss from luminescent solar concentrator waveguides," *Applied Optics,* vol. 47, no. 36, pp. 6763-6768, 2008.

[74] "Solargis," [Online]. Available: https://solargis.com/maps-and-gis-data/download/canada. [Accessed 27 10 2022].

[75] "RefractiveIndex.INFO," [Online]. Available: https://refractiveindex.info/?shelf=main&book=Si&page=Aspnes. [Accessed 4 10 2022].

[76] Y. Yu, G. Fan, A. Fermi, R. Mazzaro, V. Morandi, P. Ceroni, D.-M. Smilgies and B. K. Korgel, "Size-Dependent Photoluminescence Efficiency of Silicon Nanocrystal Quantum Dots," *The Journal of Physical Chemistry,* vol. 121, no. 41, pp. 23240-23248, 2017.

Appendix

Appendix A: Additional data

A.1. Global horizontal irradiance in Canada

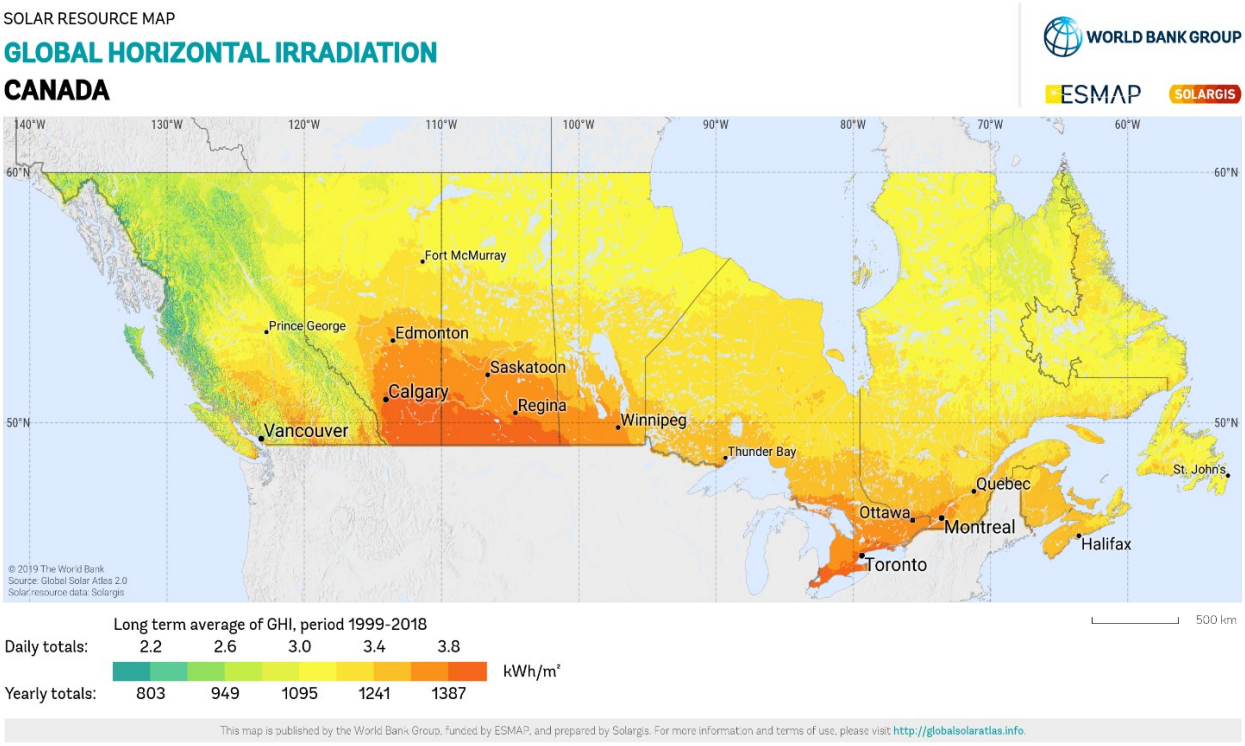

Figure A.1: Global horizontal irradiance in Canada. © 2020 The World Bank, Source: Global Solar Atlas 2.0, Solar resource data: Solargis [74].

A.2. Silicon reflective index

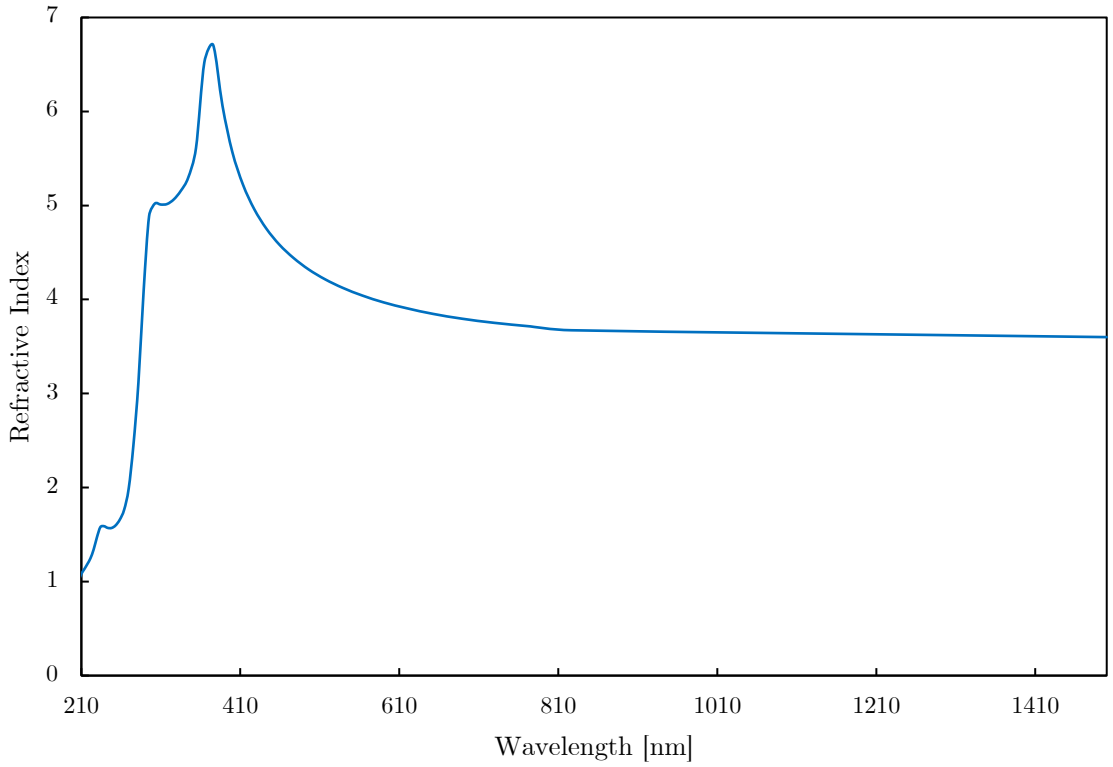

Figure A.2: Silicon refractive index variation. (Data obtained from RefractiveIndex.INFO [75])

Appendix B: Red-dye Additional Results

B.1. Red-dye LSC simulation results

(a)

(b)

(c)

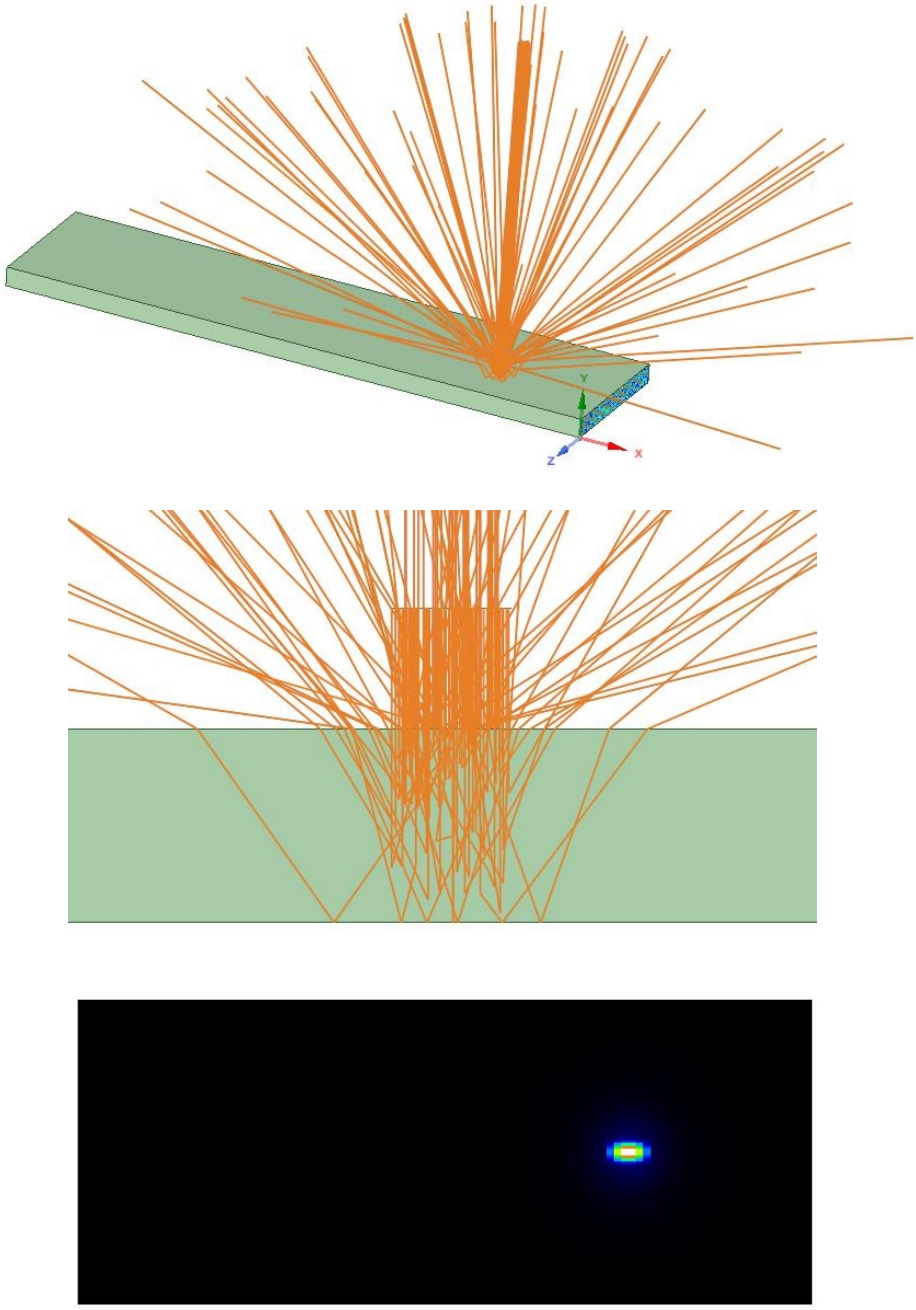

Figure A.3: Red-dye LSC simulation for reflection: (a) 3D view of reflected rays in a red-dye ray-tracing LSC model. (b) Side closeup view of the LSC model showing ray-tracing. (c) Intensity map of the reflected light.

(a)

(b)

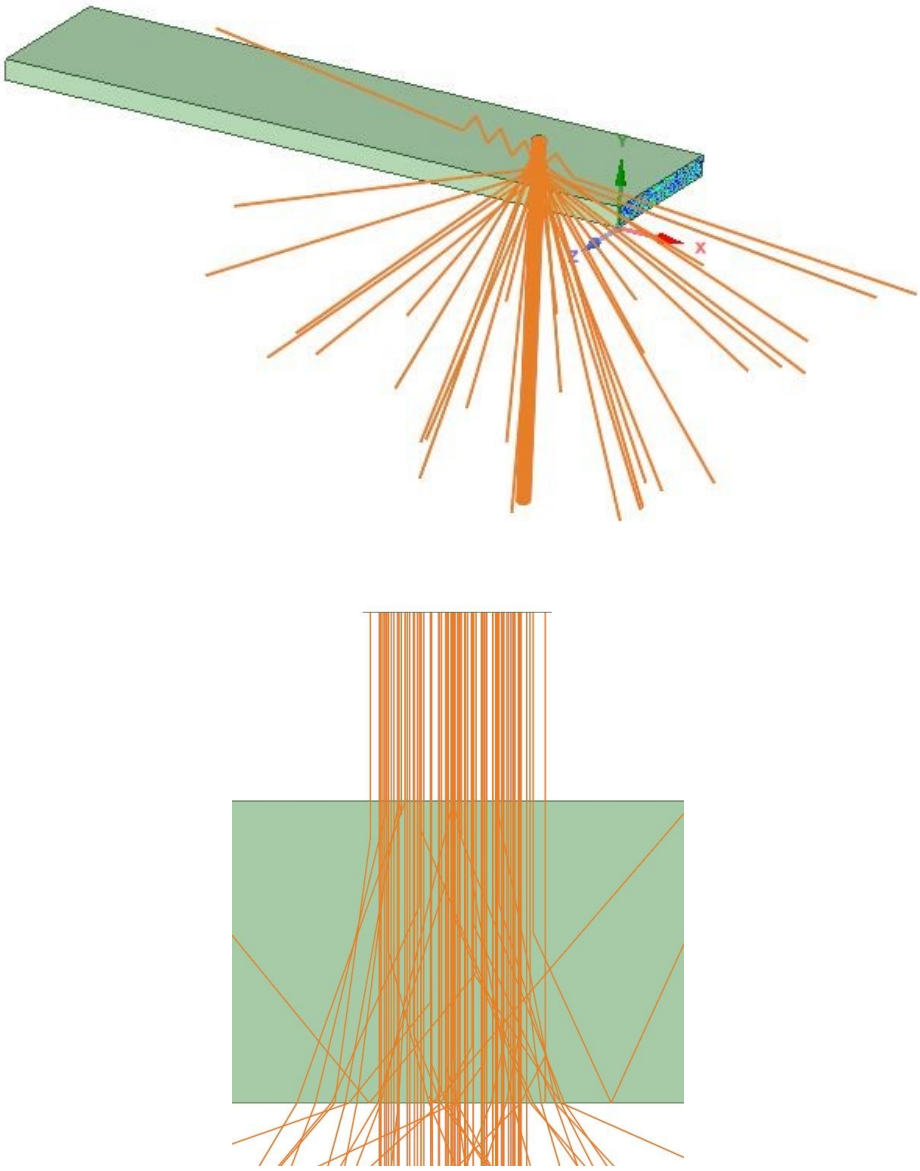

(c)

Figure A.4: Red-dye LSC simulation for transmission: (a) 3D view of transmitted rays in a red-dye ray-tracing LSC model. (b) Side closeup view of the LSC model showing ray-tracing. (c) Intensity map of the transmitted light.

B.2. Testing different light source in the red-dye model.

Two different light setups are used testing the red-dye LSC model using ANSYS. Light source (monochromatic) and sunlight (AM1.5) illuminate the LSC surface area in these two different simulations. Table B.1 shows the simulation results of the two different light sources completely illuminated to the LSC surface area.

Table B.1 shows that, the optical efficiency is around 2.56% and 25.1% of transmitted light, which will result in 63.0% of other losses by using monochromatic light at 425 nm. The solar source AM1.5 in the range of 310-1500 nm, has an optical efficiency of 1.86% and a higher transmitted light of 67.8% compared to the previous light source. The solar source received about half of the maximum optical efficiency compared to the monochromatic light. This is because red-dye particles can absorb up to 600 nm of the solar spectrum, and every wavelength does not have the same spectral intensity (see Figure 3.13).

Table B.1: Simulation results of an LSC model when illuminated by two different light sources.

Light Outcome	**Monochromatic light at 425 nm**	**Solar Spectrum AM 1.5**
Optical Efficiency	2.56%	1.86%
Reflected	9.30%	8.88%
Transmitted	25.1%	67.8%
Other Losses	63.0%	25.4%

Appendix C: QD Additional results

QDs are embedded directly into the waveguide (15 cm x 15 cm x 0.26 cm), which is called a bulk LSC. This LSC is simulated to measure the optical efficiency and losses. Figure A.5 shows a schematic representation of the bulk QD LSC model where the sensors are placed to measure the optical efficiency and losses. Figure A.7 and Figure A.8, represents the optical efficiency and losses in a PLQY of 45% and 100%, respectively. The optical efficiency of the yellow area in Figure A.7 corresponds to the blue curve in Figure A.6 and the yellow area in Figure A.8 corresponds to the red curve in Figure A.6. In a QD concentration of 0.1% w/w, the optical efficiency is 7.33% in a PLQY of 45% and an optical efficiency of 13.49% in PLQY of 100% is obtained. Figure A.9 shows the optical efficiency change when the thickness of the LSC is increased. In a QD concentration of 0.05% w/w, the optical efficiency increased from 6.81% to 9.53% when the LSC thickness increased from 0.26 cm to 2 cm.

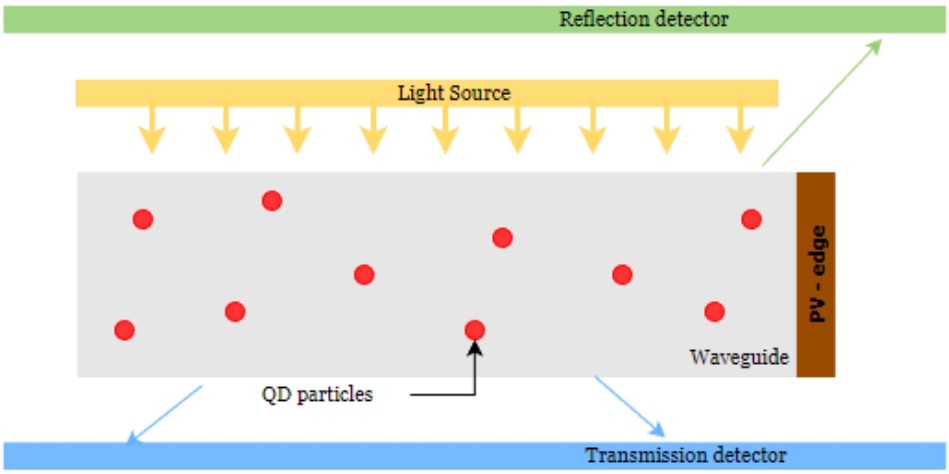

Figure A.5: Schematic diagram of a Bulk LSC model.

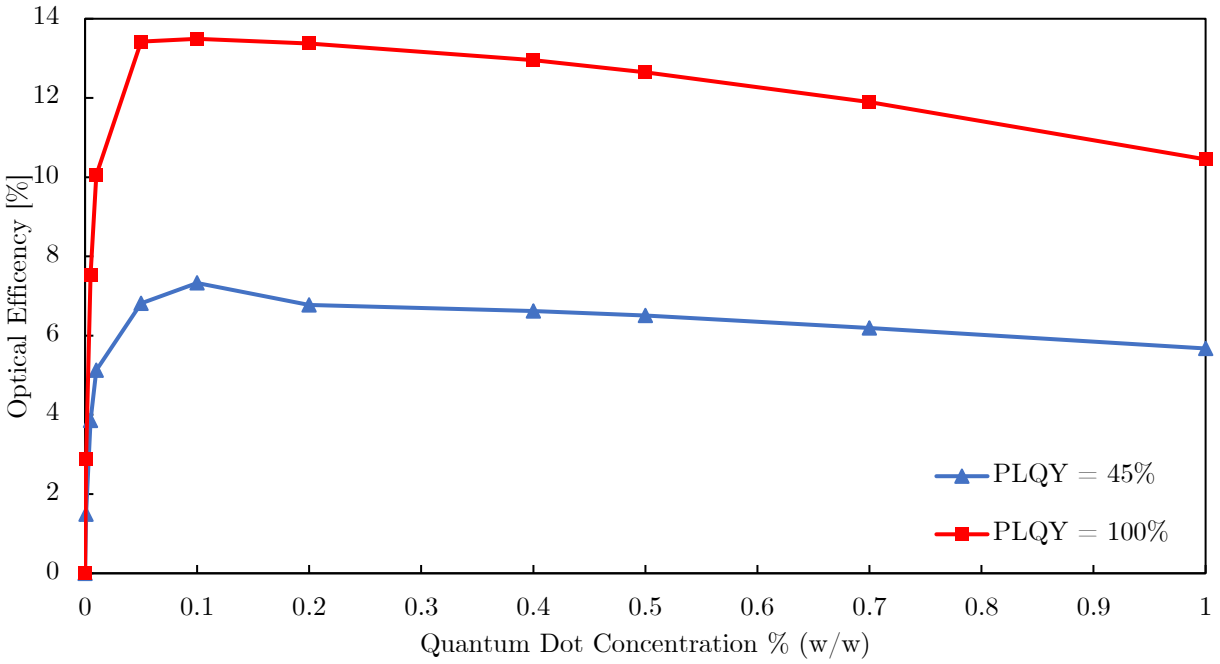

Figure A.6: Optical efficiency with the variation of QD concentration and quantum yield.

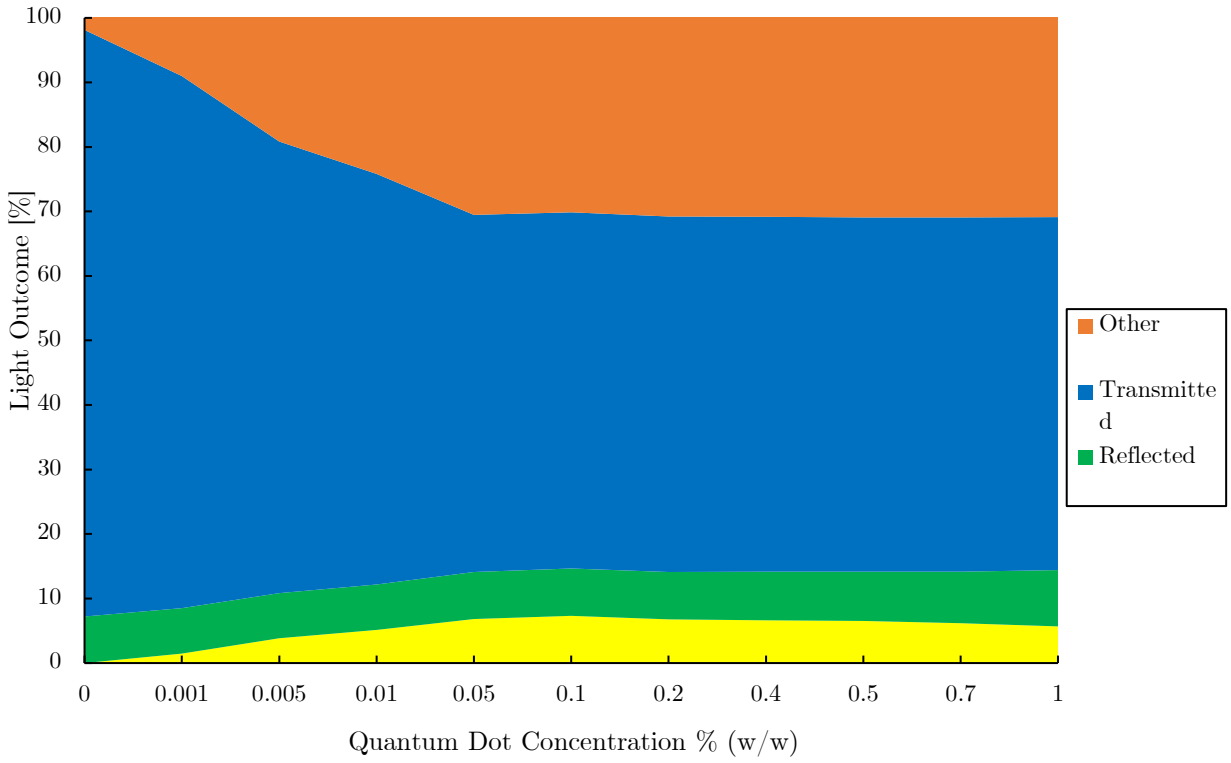

Figure A.7: Optical efficiency and losses with a QD quantum yield of 45%.

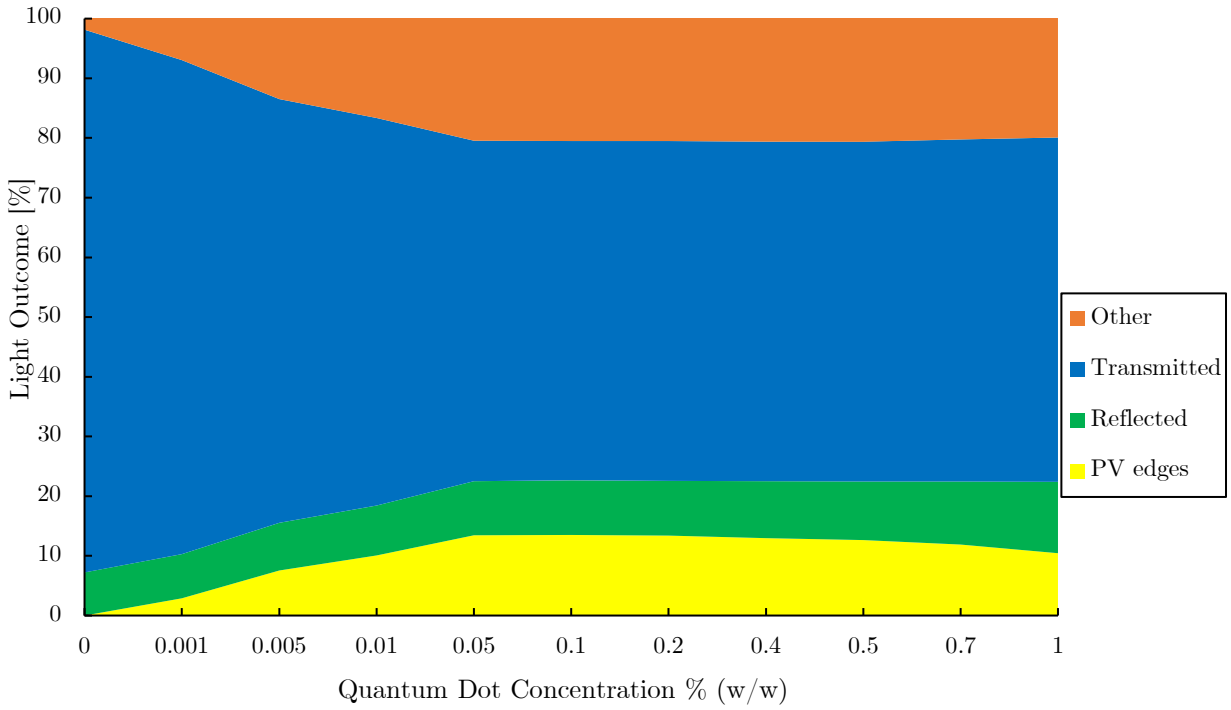

Figure A.8: Optical efficiency and losses with a QD quantum yield of 100%.

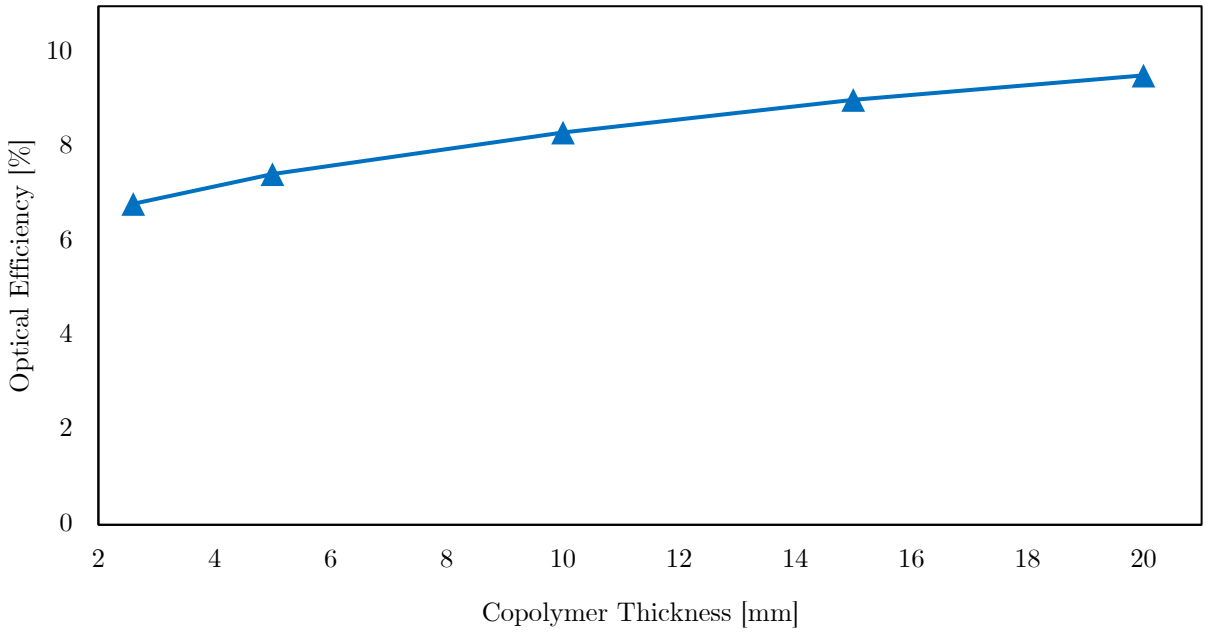

Figure A.9: Optical efficiency change with different copolymer thickness.